Cluster-Lensed Supernova Yields in the *Nancy Grace Roman Space Telescope*

Mateusz Bronikowski

University of Nova Gorica, Vipavska 13, SI-5000 Nova Gorica

Abstract

Strong gravitational lensing provides an excellent opportunity for observing lensed and magnified images of supernovae. In the past decade, several multiply-imaged supernovae were discovered, which showed their potential for probing cosmological parameters. We analysed a sample of 69 galaxy clusters in terms of their potential for multiply-imaged supernova detections by the upcoming *Nancy Grace Roman Space Telescope* High Latitude Time Domain Survey. We simulated magnified supernova lightcurves at a range of redshifts to obtain detection efficiency for the *Nancy Grace Roman Space Telescope*. We combine that with gravitational lensing models of galaxy clusters, and volumetric supernova rates, to obtain an estimate of expected number of supernovae in given clusters in the *Nancy Grace Roman Space Telescope* survey. We found multiple clusters for which several multiply-imaged supernovae can be expected if they fall within the High Latitude Time Domain Survey fields. We make recommendations on selecting those fields based on our results.

Keywords:
Gravitational lensing: strong; cosmology: observations, supernovae: general, galaxies: star formation; techniques: photometric; galaxies: clusters: general

1. Introduction

The idea to search for supernovae (SNe) in fields lensed by galaxy clusters is not new [see e.g. 1, 2, 3, 4]. The gravitational lensing effect, a phenomenon predicted by Einstein's theory of General Relativity, causes massive galaxy clusters to act as cosmic magnifying glasses, significantly amplifying the light from background sources, such as quasars, galaxies, distant supernovae occuring in those

Email address: mateusz.bronikowski@ung.si (Mateusz Bronikowski)

galaxies. It was proposed that observing a supernova with multiple images, and obtaining a light curve for each image, could be performed in order to obtain time delays between images, which in turn can be used to probe the Hubble parameter H_0 [5]. Robust measurements of the time delay can also be used to constrain the dark energy equation of state [e.g. 6, 7, 8, 9]. This method of probing cosmological parameters is called time-delay cosmography [e.g. 10]. Such measurements may prove invaluable in resolving the so-called Hubble tension, a $> 5\sigma$ disagreement between late-Universe measurements of H_0 from the SH0ES program [11] and H0LiCOW [12], and early-Universe measurements from the Planck satellite [13] and from the Dark Energy Survey constraints from galaxy clustering and weak gravitational lensing [14], which probe the early Universe's evolution.

Historically, strongly-lensed Active Galactic Nuclei (AGNs) have been used for time-delay cosmography, with the latest result from H0LiCOW by [12] combining six lensed quasars to obtain 2.4% precision, well in agreement with [11]. However, there are several advantages to using supernovae over quasars. SNe have predictable light curves, which vastly simplifies time-delay measurements compared to the stochastic nature of AGNs; SNe fade quickly, which allows for precise photometry to be obtained by performing background subtraction once the SN fades, and for predictive experiments on the timing and brightness of delayed trailing images, as SN host fluxes and AGN fluxes alike are typically highly blended [15]; time-delay measurements for SNe require much shorter campaigns; and the impact of microlensing is somewhat mitigated [16, 17], with less pronounced chromatic effects [18, 19], although microlensing can still be a significant source of uncertainty for systems with low time delays (on the order of 1 day or less), such as iPTF16geu [20] or SN Zwicky [21]. Those are time delays typical of galaxy-lensed supernovae, but significantly lower than those typical of galaxy cluster lenses.

Despite the strong scientific potential of such an observation, it was only 50 years after Refsdal's publication, in 2014, that the first multiply-imaged supernova, dubbed SN "Refsdal", was discovered [22], and used to provide a measurement of the Hubble parameter [e.g. 23, 24]; futhermore, so far, only a handful of other multiply-imaged supernovae have been discovered, e.g. SN Requiem [25], iPTF16geu [20], SN Zwicky [26] or the most recent SN H0pe [27].

Particularly valuable when lensed are supernovae of Type Ia (SNe Ia), those used as "standardizable" candles to measure cosmological parameters [e.g. 28, 29]. Their standardisable absolute magnitude, as well as a well-understood light curve evolution [e.g. 30, 31, 32], can provide constrains for lens modelling, and break degeneracies that occur due to the mass-sheet degeneracy [33, 34], if the mililensing and microlensing effects are not extremely strong.

The upcoming *Nancy Grace Roman Space Telescope* (*NGRST*), scheduled to launch in 2026, is going to be a powerful tool in the search for transient objects.

As one of the major goals of the mission is to make a state-of-the-art measurement of dark energy through Type Ia SN cosmology, the telescope is going to use its Wide Field Instrument with a field of view of 0.28 square degrees [35] to perform its High Latuitude Time Domain Survey (HLTDS). HLTDS will observe fields at a high galactic latitude to minimize galactic extinction. The fields will be observed for two years at a cadence of 5 days, in two regimes: Deep, with a filter set adapted for high redshift observations and long exposure times, and Wide, with a focus on lower redshift targets, lower exposure times, but with a higher area of the sky covered. The survey is expected to detect an unprecedented number of supernovae. Predictions have been made regarding the expected number of supernovae lensed by galaxies for many surveys [e.g. 36, 37, 38, 19, 39, 40], however, for cluster-scale lensed supernovae, the predictions were very few. So far, only seven clusters have been analysed for their strongly-lensed supernova prospects [41, 42, 43], of which only two analysed prospects for *NGRST*.

In this work, we aim to analyse the available sample of galaxy clusters as gravitational telescopes, and make predictions for cluster-lensed supernovae in HLTDS.

2. Data

In this work, models for galaxy clusters, for which gravitational lensing models have been developed, were taken from previous studies and are listed in Table 1. We selected models of 69 galaxy clusters – 70 models, because one cluster, RXS J060313.4+4212, is split into two parts – along with their redshifts and sources. We limited our sample to models which have available deflection, shear and convergence lensing maps. Our sample consists of the majority of galaxy clusters which have been modeled.

The clusters in our sample are mostly from the RELICS program [44, 56], CLASH [53], as well as [52]'s program to observe clusters with the MUSE instrument [57], as well as several models from [54] and [55].

[1]The cluster was studied and modeled by the RELICS program [44, 56], but no paper has been published on the cluster. Models available at `https://archive.stsci.edu/hlsp/relics`, date of access: 2023-08-02

[2]The clusters were also analysed by the team, but are not included in the paper. Data available here: `https://cral-perso.univ-lyon1.fr/labo/perso/johan.richard/MUSE_data_release/`, date of access: 2023-08-02

Table 1: Cluster models and their sources used in this work.

Cluster	z	Source & comments
A1758a	0.280	[1]
A1763	0.228	[1]
A2163	0.203	[44]
A2537	0.297	[44]
A2813	0.292	[1]
A3192	0.425	[1]
A697	0.282	[45]
ACT-CLJ0102-49151	0.870	[44]
AS295	0.300	[45]
CLJ0152.7-1357	0.833	[46]
MACS J0025.4-1222	0.586	[1]
MACS J0035.4-2015	0.352	[1]
MACS J0159.8-0849	0.405	[1]
MACS J0257.1-2325	0.505	[1]
MACS J0308.9+2645	0.356	[47]
MACS 0417.5-1154	0.443	[48]
MACS 0553.4-3342	0.430	[1]
MS1008.1-1224	0.306	[1]
PLCK G171.9-40.7	0.270	[47]
PLCK G209.79+10.23	0.677	[1]
PLCK G287.0+32.9	0.390	[49]
RXC J0018.5+1626	0.546	[1]
RXC J0032.1+1808	0.396	[50]
RXC J0142.9+4438	0.341	[44]
RXC J0232.2-4420	0.284	[1]
RXC J0600.1-2007	0.460	[1]
RXC J0911.1+1746	0.505	[1]
RXC J0949.8+1707	0.383	[1]
RXC J2211.7-0350	0.397	[44]
RXS J060313.4+4212_N	0.228	The two parts of the cluster
RXS J060313.4+4212_S	0.228	were modeled separately. [1]
SMACS J0723.3-7327	0.390	[1]
SPT-CLJ0615-5746	0.972	[51]
WHL J24.3324-8.477	0.566	[1]
A370	0.375	[52]
A2744	0.308	[52]
AS1063	0.348	[52]
BULLET	0.296	[52]
MACS0257	0.322	[52]
MACS0329	0.450	[52]
MACS0416	0.397	[52]
MACS0451	0.550	[52]
MACS0520	0.336	[52]
MACS0940	0.335	[52]
MACS1206	0.438	[52]
MACS2214	0.502	[52]
RXJ1347	0.451	[52] [2]
SMACS2031	0.331	[52] [2]
SMACS2131	0.442	[52] [2]
SMACS2332	0.3980	[52] [2]
A1423	0.213	[53]
A209	0.206	[53]
A2261	0.224	[53]
A383	0.187	[53]
A611	0.288	[53]
CLJ1226+3332	0.890	[53]
MACSJ0647+70	0.584	[53]
MACSJ0717+37	0.548	[53]
MACSJ0744+39	0.686	[53]
MACSJ1149+22	0.544	[53]
MACSJ1423+24	0.545	[53]
MACSJ1720+35	0.391	[53]
MACSJ2129-07	0.589	[53]
MS 2137.3-2353	0.313	[53]
RXJ2129+0005	0.234	[53]
MACSJ0429	0.399	[54]
MACSJ1115	0.352	[54]
MACSJ1311	0.494	[54]
MACSJ1931	0.352	[54]
A1489	0.350	[55]

3. Methodology

3.1. Supernova rates from SFRs

Since the progenitors of CC SNe are massive stars, it is safe to assume that their short lifespan is negligible compared to the timescales at which Star Formation Rates (SFRs) specific to a given galaxy change, and thus should trace the locally recent SFR. We follow previous high-z CC SN studies in assuming that progenitors of CC SNe are stars in the $8 - 50 M_\odot$ range, and use a [58] initial mass function (IMF, $\phi(z)$) to calculate the fraction of stars which form CC SN progenitors:

$$k_{\rm CC} = \frac{\int_{8M_\odot}^{50M_\odot} \phi(M) {\rm d}M}{\int_{0.1M_\odot}^{100M_\odot} \phi(M) {\rm d}M},$$

resulting in $k_{\rm CC} = 0.0060^{+0.0019}_{-0.0022} M_\odot^{-1}$. Thus, the CC SN rate in a given galaxy ("specific" to a galaxy) is:

$$R^{\rm s}_{\rm CC} = k_{\rm CC} \cdot {\rm SFR}.$$

We further divide CC SNe into seven subtypes following [59], who combined relative SN rates from [60] with Type IIL and Type IIP relative rates from [61]. Thus, for a CC SN subtype j, the galaxy-specific supernova rate is:

$$R^{\rm s}_j = k_{\rm CC} \cdot {\rm SFR} \cdot r_j,$$

where r_j is the relative rate of the subtype j of CC SNe, such that $\Sigma r_j = 1$. We assume that these relative rates are constant through cosmic history.

The relation between Type Ia SN rates and Star Formation History is more complex. The two main models of their progenitors necessitate the formation of at least one White Dwarf (WD), which is a slower process due to lower WD progenitor's masses. Further, after the formation of the WD, more time is required for the infall of matter onto it, either from a companion star, or during an inspiral period in a binary system. In order to calculate the galaxy-specific Type Ia SN rate $R^{\rm s}_{\rm Ia}$, we use the simple model from [62]. According to this model, $R^{\rm s}_{\rm Ia}$ consists of two components: a prompt element proportional to sSFR, and a time-extended element proportional to the total stellar mass formed within the galaxy:

$$R^{\rm s}_{\rm Ia} = A \cdot M_* + B \cdot {\rm SFR},$$

with A and B being the proportionality constants. We use updated values from [63]:

$$A = (4.66 \pm 0.56) \cdot 10^{-14}\ {\rm SNe\ yr^{-1}} M_\odot^{-1}, B = (4.88^{+0.54}_{-0.52})\ \cdot 10^{-4} \frac{\rm SNe\ yr^{-1}}{M_\odot {\rm yr}^{-1}}.$$

We acknowledge the so-called $A + B$ model's limitations, mentioned by [64] and [63]; however, we believe that it is sufficiently accurate to not be a major contributor to our work's uncertainties. Since there are virtually no discovered Type Ia supernovae beyond $z = 2$, extending any model beyond this redshift, even if it is physically motivated, is uncertain.

3.2. Survey control time

The expected number of SNe $\mathrm{d}N_j$ of a subtype j in a comoving volume element $\mathrm{d}V_c$ depends on the volumetric SN rate R_j^V and the survey control time, $T_j(z)$, which is the total time during which the survey is sensitive to detecting a supernova:

$$\mathrm{d}N_j(z) = T_j(z)\frac{R_j^V(z)}{1+z}\mathrm{d}V_c, \tag{1}$$

where the $(1 + z)$ factor corrects for cosmological time dilation, as $T_j(z)$ in this work is calculated in the observer frame, and SN rates $R_j^V(z)$, R_j^{s} are in the rest-frame. The comoving volume unit $\mathrm{d}V_c$ can be calculated as follows:

$$\mathrm{d}V_c = \frac{cd_L^2(z)}{H(z)(1+z)^2}\mathrm{d}\omega\mathrm{d}z,$$

where $\mathrm{d}\omega$ is the solid angle element for the survey, $\mathrm{d}z$ is the redshift element, and d_L is the cosmological luminosity distance for redshift z.

In this work, we are considering supernovae which are strongly lensed, and thus magnified by a factor of μ. This affects the survey control time by increasing the time during which a supernova is brighter than the survey detection threshold. Therefore, Equation 1 can be rewritten as:

$$\mathrm{d}N_j(z,\mu) = T_j(z,\mu)\frac{R_j^V}{1+z}\mathrm{d}V_c. \tag{2}$$

In order to obtain the survey control time, $T_j(z,\mu)$, we use the *Supernova Analysis Package* [*SNANA,* 65] to simulate supernovae of the following types: Ia, Ib, Ic, IIb, IIn, IIL, IIP, IIc-BL.

We simulated a total of 6.8 million supernovae, lensed by a factor of $\mu \in [1.166, 100]$, at redshifts in the range of $z \in [0.2, 6]$. We simulate a survey of 725 days of observations in accordance with the survey specifications proposed by [35], and simulate SNe, the peaks of which occur between 50 days before the first observation, to 15 days after the last observation of a given field. Thus, the total time in which SNe are simulated is $t_{\mathrm{sim}} = 790$ days.

It follows that the survey control time $T_j(z,\mu)$ is the product of t_{sim} and the probability $p_j(z,\mu)$ that a supernova of type j, at redshift z, magnified by a factor

of μ, will be detected, if it explodes at a time such that its peak falls in the simulated period:

$$T_j(z, \mu) = t_{\rm sim} p_j(z, \mu).$$

We interpret the fraction of SNe detected by our simulations to be a proxy for $p_j(z, \mu)$, and that each simulated SN is statistically independent from others for the purposes of uncertainty estimation. Our detection condition was that a given Supernova has two detections above Signal to Noise Ratio 5, in any filter, at at least two epochs. We repeated the simulation for both the Wide and the Deep survey tier, as per [35]. We only consider the photometric survey element and make no considerations for the planned *NGRST* spectroscopic survey part.

3.3. Volumetric supernova yield estimates

In order to obtain a volumetric estimate of SN yields, we assume volumetric CC SN rates of $R^V_{\rm CC}(z) = k^V_{\rm CC} h^2 \psi(z)$, where $k^V_{\rm CC} = 0.0091 \pm 0.0017$ from [66] is the fraction of stars that are CC SN progenitors, and $\psi(z)$ is the Cosmic Star Formation History (CSFH), using the updated values from [67], Table 2. We extend this model to $z = 6$. We note that the k_{CC} cited by [66] differs from the one computed from a [58] IMF, as it is a model fit. We assume that the relative fractions of CC SN subtypes are constant throughout cosmic history and use the rates cited by [59].

We use the simple volumetric Type Ia SN rate cited by [67], which follows a broken power-law: $R^V_{\rm Ia} = R_0(1+z)^A$, with $R_0 = 2.40 \pm 0.02 \times 10^{-5}$ yr^{-1} Mpc^{-3} h^3_{70} and $A = 1.55 \pm 0.02$ for $z <= 1$, and $A = -0.1 \pm 0.2$ for $z > 1$.

For every cluster in the sample, we computed the expected yield of detected SNe as a function of redshift $\mathrm{d}N_j/\mathrm{d}z$, by integrating $\mathrm{d}N_j(z, \mu)$ given in Equation 2 in the source plane at fixed redshifts, in bins of $\Delta z = 0.1$. We limited magnification to $\mu_{\rm max} = 100.$ to limit effects from finite-resolution cluster lensing models.

It is important to note that the *NGRST* survey's target observed fields have not yet been selected; only a handful of guidelines as to how the fields will be selected are presented by [35]. We therefore cannot conclusively tell whether a given cluster will be observed by *NGRST*, and can only provide predictions which assume a cluster will be observed.

4. Results

The number of expected supernovae of a given subtype, assuming the cluster is in a given survey field, is given in Table 2 for the Deep field, and in Table 3 for the Wide survey field. Figure 1 presents the 20 most promising clusters in either survey domain with respect to the number of expected multiply-imaged Type Ia supernova

Table 2: Expected number of multiply-imaged supernova images of a given subtype in *NGRST* High Latitude Time Domain Survey, if a given cluster is in the deep survey field.

Cluster	Type Ia	Type IIP	Type IIn	Type IIL	Type IIb	Type Ib	Type Ic	Type Ic-BL
MACSJ0717+37	13.50	15.57	1.68	2.74	2.94	3.22	2.32	0.34
MACS J0025.4-1222	8.54	9.33	1.08	1.74	1.80	2.01	1.47	0.21
RXC J2211.7-0350	7.84	9.50	1.02	1.66	1.82	1.98	1.42	0.20
RXC J0032.1+1808	6.95	8.88	0.90	1.49	1.69	1.81	1.29	0.19
MACS 0553.4-3342	6.53	7.77	0.83	1.36	1.47	1.60	1.15	0.17
PLCK G287.0+32.9	4.40	5.97	0.56	0.93	1.12	1.16	0.82	0.12
A3192	3.93	5.10	0.51	0.85	0.97	1.04	0.74	0.10
MACS 0417.5-1154	4.15	4.97	0.51	0.84	0.93	1.00	0.72	0.10
MACS J0308.9+2645	3.43	4.65	0.44	0.73	0.87	0.91	0.64	0.09
RXJ1347	3.74	4.45	0.46	0.76	0.83	0.90	0.65	0.09
PLCK G171.9-40.7	3.15	4.40	0.42	0.69	0.83	0.87	0.61	0.09
A370	3.21	4.30	0.42	0.69	0.81	0.85	0.60	0.08
A1489	3.24	4.24	0.42	0.69	0.79	0.84	0.60	0.08
AS1063	3.04	4.00	0.39	0.65	0.75	0.80	0.57	0.08
A2744	2.90	3.83	0.39	0.64	0.73	0.78	0.56	0.08
A1758a	2.85	3.79	0.38	0.62	0.72	0.76	0.54	0.08
MACS J0035.4-2015	2.87	3.70	0.38	0.63	0.71	0.76	0.54	0.08
MACS0329	2.67	3.24	0.33	0.55	0.61	0.65	0.47	0.06
MACS1206	2.43	3.11	0.30	0.51	0.58	0.62	0.44	0.06
SPT-CLJ0615-5746	3.21	3.03	0.33	0.54	0.54	0.60	0.43	0.06
MACSJ0647+70	2.64	2.84	0.30	0.49	0.52	0.56	0.40	0.06
MACS0520	2.00	2.71	0.26	0.43	0.51	0.54	0.38	0.05
RXC J0600.1-2007	2.15	2.78	0.26	0.43	0.51	0.53	0.37	0.05
PLCK G209.79+10.23	2.60	2.53	0.31	0.49	0.48	0.55	0.40	0.05
RXS J060313.4+4212 S	1.82	2.56	0.25	0.41	0.49	0.51	0.36	0.05
MACS J0257.1-2325	2.10	2.36	0.27	0.44	0.46	0.51	0.38	0.05
MACS J0159.8-0849	1.91	2.48	0.24	0.40	0.46	0.49	0.35	0.05
MACSJ1931	1.83	2.44	0.24	0.40	0.46	0.49	0.34	0.05
MS1008.1-1224	1.78	2.26	0.23	0.38	0.43	0.46	0.33	0.04
MACS0257	1.67	2.27	0.22	0.36	0.43	0.45	0.32	0.04
SMACS J0723.3-7327	1.93	2.11	0.24	0.39	0.40	0.45	0.33	0.04
A2261	1.56	2.14	0.21	0.34	0.40	0.43	0.30	0.04
WHL J24.3324-8.477	1.89	2.21	0.22	0.37	0.41	0.44	0.31	0.04
MACS0451	1.94	2.15	0.23	0.37	0.40	0.43	0.31	0.04
MACS0416	1.67	2.02	0.20	0.34	0.38	0.40	0.29	0.04
ACT-CLJ0102-49151	2.51	2.17	0.24	0.39	0.37	0.42	0.30	0.04
RXC J0018.5+1626	1.65	1.96	0.19	0.32	0.36	0.39	0.27	0.04
RXC J0949.8+1707	1.42	1.90	0.18	0.30	0.36	0.37	0.27	0.03
BULLET	1.45	1.93	0.18	0.30	0.36	0.38	0.26	0.03
A2537	1.30	1.85	0.17	0.28	0.34	0.35	0.25	0.03
RXC J0142.9+4438	1.30	1.78	0.16	0.27	0.33	0.34	0.24	0.03
MACSJ1149+22	1.62	1.80	0.17	0.29	0.32	0.34	0.24	0.03
RXC J0232.2-4420	1.13	1.63	0.15	0.25	0.30	0.31	0.22	0.03
A611	1.09	1.51	0.14	0.24	0.28	0.30	0.21	0.03
MACSJ2129-07	1.36	1.55	0.15	0.26	0.28	0.30	0.22	0.03
MACS2214	1.23	1.52	0.15	0.25	0.28	0.30	0.21	0.03
SMACS2332	1.21	1.49	0.15	0.25	0.28	0.30	0.21	0.03
A1423	0.99	1.43	0.13	0.22	0.27	0.28	0.20	0.02
SMACS2131	1.14	1.45	0.14	0.23	0.27	0.28	0.20	0.03
MACSJ1720+35	1.15	1.43	0.14	0.23	0.26	0.28	0.20	0.02
MACSJ0744+39	1.41	1.44	0.14	0.24	0.25	0.27	0.19	0.02
SMACS2031	1.09	1.38	0.13	0.22	0.25	0.27	0.19	0.02
RXS J060313.4+4212 N	0.90	1.26	0.12	0.20	0.24	0.25	0.17	0.02
MACSJ0429	0.96	1.22	0.12	0.20	0.23	0.24	0.17	0.02
MACSJ1311	0.96	1.20	0.12	0.20	0.22	0.24	0.17	0.02
AS295	0.84	1.12	0.10	0.17	0.21	0.21	0.15	0.02
A2813	0.72	1.07	0.09	0.16	0.20	0.20	0.14	0.02
MS 2137.3-2353	0.76	0.99	0.09	0.16	0.18	0.20	0.14	0.02
A1763	0.65	0.97	0.09	0.15	0.18	0.19	0.13	0.01
MACSJ1423+24	0.78	0.94	0.09	0.15	0.17	0.18	0.13	0.01
A383	0.58	0.86	0.08	0.13	0.16	0.17	0.12	0.01
MACS0940	0.58	0.75	0.07	0.13	0.14	0.15	0.11	0.01
A2163	0.49	0.70	0.06	0.11	0.13	0.13	0.09	0.01
RXJ2129+0005	0.41	0.59	0.05	0.09	0.11	0.11	0.08	0.01
A209	0.40	0.55	0.05	0.09	0.10	0.11	0.08	0.01
CLJ0152.7-1357	0.63	0.53	0.06	0.09	0.09	0.10	0.07	0.01
CLJ1226+3332	0.54	0.50	0.05	0.08	0.08	0.09	0.06	0.01
RXC J0911.1+1746	0.36	0.42	0.04	0.07	0.07	0.08	0.05	0.00
MACSJ1115	0.22	0.29	0.02	0.04	0.05	0.05	0.03	0.00
A697	0.11	0.15	0.01	0.02	0.02	0.02	0.02	0.00

Table 3: Expected number of multiply-imaged supernova images of a given subtype in the *NGRST* High Latitude Time Domain Survey, if a given cluster is in the wide survey field.

Cluster	Type Ia	Type IIP	Type IIn	Type IIL	Type IIb	Type Ib	Type Ic	Type Ic-BL
MACSJ0717+37	7.24	9.02	1.39	1.94	1.20	1.59	1.19	0.18
MACS J0025.4-1222	4.48	5.01	0.86	1.15	0.66	0.92	0.69	0.10
RXC J2211.7-0350	4.46	5.77	0.85	1.19	0.81	1.05	0.78	0.12
RXC J0032.1+1808	4.09	5.68	0.77	1.13	0.80	1.01	0.74	0.11
MACS 0553.4-3342	3.59	4.59	0.69	0.96	0.62	0.82	0.61	0.09
PLCK G287.0+32.9	2.66	4.27	0.50	0.77	0.63	0.72	0.53	0.08
A3192	2.37	3.35	0.44	0.65	0.48	0.60	0.44	0.06
MACS 0417.5-1154	2.26	3.07	0.43	0.62	0.42	0.53	0.39	0.06
MACS J0308.9+2645	2.08	3.26	0.39	0.60	0.48	0.56	0.41	0.06
RXJ1347	2.02	2.71	0.39	0.55	0.37	0.47	0.35	0.05
PLCK G171.9-40.7	1.99	3.12	0.37	0.57	0.47	0.55	0.40	0.06
A370	1.95	2.96	0.37	0.55	0.43	0.52	0.38	0.05
A1489	1.92	2.82	0.36	0.54	0.40	0.49	0.36	0.05
AS1063	1.81	2.67	0.34	0.51	0.38	0.47	0.34	0.05
A2744	1.79	2.53	0.33	0.49	0.36	0.45	0.33	0.05
A1758a	1.76	2.56	0.33	0.49	0.37	0.45	0.33	0.05
MACS J0035.4-2015	1.74	2.38	0.32	0.47	0.34	0.43	0.32	0.04
MACS0329	1.48	2.03	0.28	0.41	0.28	0.35	0.26	0.04
MACS1206	1.40	2.05	0.26	0.39	0.29	0.35	0.26	0.04
SPT-CLJ0615-5746	1.32	1.58	0.26	0.36	0.17	0.23	0.18	0.03
MACSJ0647+70	1.25	1.66	0.24	0.34	0.21	0.27	0.20	0.03
MACS0520	1.23	1.87	0.23	0.35	0.27	0.32	0.24	0.03
RXC J0600.1-2007	1.21	1.99	0.23	0.36	0.28	0.32	0.23	0.03
PLCK G209.79+10.23	1.21	1.22	0.24	0.30	0.15	0.22	0.17	0.02
RXS J060313.4+4212 S	1.19	1.81	0.22	0.33	0.27	0.32	0.23	0.03
MACS J0257.1-2325	1.16	1.30	0.22	0.29	0.18	0.24	0.18	0.02
MACS J0159.8-0849	1.12	1.66	0.21	0.31	0.24	0.28	0.21	0.03
MACSJ1931	1.12	1.63	0.21	0.31	0.23	0.29	0.21	0.03
MS1008.1-1224	1.05	1.43	0.20	0.28	0.20	0.26	0.19	0.02
MACS0257	1.03	1.57	0.19	0.29	0.23	0.27	0.20	0.03
SMACS J0723.3-7327	1.00	1.15	0.19	0.26	0.15	0.21	0.16	0.02
A2261	0.99	1.46	0.18	0.27	0.21	0.26	0.19	0.02
WHL J24.3324-8.477	0.99	1.35	0.19	0.27	0.18	0.22	0.17	0.02
MACS0451	0.97	1.25	0.19	0.26	0.16	0.21	0.15	0.02
MACS0416	0.91	1.27	0.17	0.25	0.17	0.21	0.16	0.02
ACT-CLJ0102-49151	0.90	1.09	0.19	0.25	0.11	0.15	0.11	0.02
RXC J0018.5+1626	0.87	1.22	0.17	0.24	0.16	0.20	0.15	0.02
RXC J0949.8+1707	0.86	1.30	0.16	0.24	0.19	0.22	0.16	0.02
BULLET	0.86	1.35	0.16	0.25	0.19	0.23	0.16	0.02
A2537	0.82	1.37	0.15	0.24	0.21	0.23	0.17	0.02
RXC J0142.9+4438	0.79	1.28	0.15	0.23	0.19	0.21	0.15	0.02
MACSJ1149+22	0.77	1.15	0.15	0.22	0.14	0.17	0.13	0.02
RXC J0232.2-4420	0.72	1.22	0.13	0.21	0.18	0.21	0.15	0.02
A611	0.69	1.08	0.13	0.19	0.16	0.18	0.13	0.02
MACSJ2129-07	0.69	0.94	0.13	0.19	0.12	0.15	0.11	0.01
MACS2214	0.68	0.97	0.13	0.19	0.13	0.16	0.12	0.01
SMACS2332	0.68	0.92	0.13	0.18	0.12	0.16	0.12	0.01
A1423	0.66	1.04	0.12	0.18	0.16	0.18	0.13	0.02
SMACS2131	0.65	0.97	0.12	0.18	0.14	0.16	0.12	0.01
MACSJ1720+35	0.64	0.95	0.12	0.18	0.13	0.16	0.11	0.01
MACSJ0744+39	0.62	0.85	0.12	0.17	0.10	0.12	0.09	0.01
SMACS2031	0.61	0.94	0.11	0.17	0.13	0.15	0.11	0.01
RXS J060313.4+4212 N	0.58	0.90	0.10	0.16	0.13	0.16	0.11	0.01
MACSJ0429	0.56	0.78	0.10	0.15	0.11	0.13	0.10	0.01
MACSJ1311	0.55	0.76	0.10	0.15	0.10	0.13	0.09	0.01
AS295	0.50	0.79	0.09	0.14	0.11	0.13	0.09	0.01
A2813	0.46	0.82	0.08	0.14	0.12	0.13	0.10	0.01
MS 2137.3-2353	0.45	0.66	0.08	0.12	0.09	0.11	0.08	0.01
A1763	0.44	0.73	0.08	0.12	0.11	0.12	0.09	0.01
MACSJ1423+24	0.41	0.63	0.08	0.12	0.08	0.10	0.07	0.01
A383	0.39	0.64	0.07	0.11	0.10	0.11	0.08	0.01
MACS0940	0.35	0.47	0.06	0.09	0.06	0.08	0.06	0.00
A2163	0.32	0.51	0.05	0.09	0.07	0.09	0.06	0.01
RXJ2129+0005	0.26	0.43	0.05	0.07	0.06	0.07	0.05	0.00
A209	0.26	0.38	0.04	0.07	0.05	0.06	0.05	0.00
CLJ0152.7-1357	0.22	0.25	0.04	0.06	0.02	0.03	0.02	0.00
CLJ1226+3332	0.20	0.29	0.04	0.06	0.03	0.03	0.02	0.00
RXC J0911.1+1746	0.18	0.26	0.03	0.05	0.03	0.04	0.03	0.00
MACSJ1115	0.12	0.23	0.02	0.03	0.03	0.03	0.02	0.00
A697	0.06	0.12	0.01	0.02	0.01	0.02	0.01	0.00

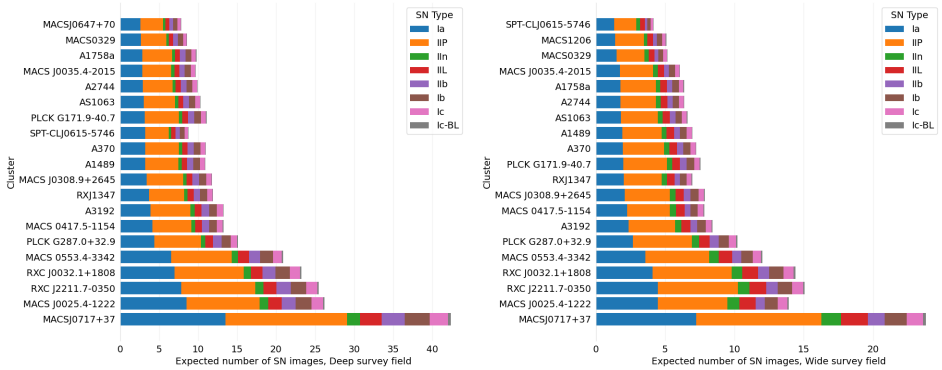

Figure 1: Expected multiply-imaged supernova yields for the 25 clusters with the highest number of expected Type Ia supernova images, for the for the Deep (left) and Wide (right) survey tier.

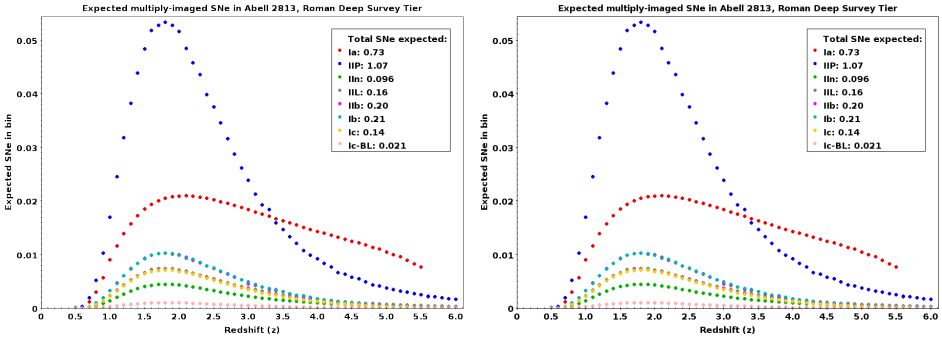

Figure 2: Distribution of expected multiply-imaged supernovae as a function of redshift for the galaxy cluster Abell 2813 in the Deep (left) and Wide (right) survey tiers. Individual images of supernovae are counted separately.

images. A large discrepancy can be clearly seen between individual clusters, highlighting the variety between clusters' potential as gravitational telescopes.

An example redshift distribution of expected supernova images is presented in Figure 2, for the Deep and Wide survey tiers, respectively. The Figures show expectations for Abell 2813, however, a similar distribution can be found for most other clusters as well. The vast majority of Core Collapse SNe can be expected in the z range between 1 and 3, with Type Ia having a distribution more skewed towards higher redshifts.

5. Conclusions

We analysed most of the galaxy clusters which were analysed as gravitational telescopes available in literature. We accomplished it by analysing *NGRST*'s capa-

bilities as a detector of lensed supernovae, and then combining it with supernova rates throughout the history of the Universe, and gravitational lensing models of individual galaxy clusters.

We find that *NGRST* is very promising as a multiply-imaged supernova detector. If the clusters we studied are selected as targets for *NGRST* observations in the HLTDS, we can expect it to detect multiple Supernovae throughout the mission duration.

Based on our research, recommendations can be made for the survey. Especially of interest is the galaxy cluster MACS J0717+37 (MACS J0717.5+3745); however, the cluster is at a low galactic latitude of around 20°, which falls outside the planned latitude range of the survey. Nevertheless, we recommend that promising clusters from our sample which are in, or close to, the planned latitude range provided by [35], are observed. One excellent target is MACS J0025.4-1222, which is the second most promising gravitational telescope in our sample, and falls within proposed survey requirements. We strongly recommend that it falls within the area of continual viewing.

Acknowledgements

This work is based on observations taken by the RELICS Treasury Program (GO 14096) with the NASA/ESA HST, which is operated by the Association of Universities for Research in Astronomy, Inc., under NASA contract NAS5-26555. The following software was used in this work: *astropy* [68], *Matplotlib* [69], *SNANA* [65], *CIGALE* [70], based on [71] and [72].

References

[1] I. Kovner and B. Paczynski, *Supernovae in luminous arcs*, *Astrophysical Journal Letters* **335** (1988) L9.

[2] M. Sullivan, R. Ellis, P. Nugent, I. Smail and P. Madau, *A strategy for finding gravitationally lensed distant supernovae*, *Monthly Notices of the Royal Astronomical Society* **319** (2000) 549 [astro-ph/0007228].

[3] A. Gal-Yam, D. Maoz and K. Sharon, *Supernovae in deep Hubble Space Telescope galaxy cluster fields: cluster rates and field counts*, *Monthly Notices of the Royal Astronomical Society* **332** (2002) 37 [astro-ph/0109089].

[4] C. Gunnarsson and A. Goobar, *Massive galaxy clusters as gravitational telescopes for distant supernovae*, *Astronomy and Astrophysics* **405** (2003) 859 [astro-ph/0211401].

[5] S. Refsdal, *On the possibility of determining Hubble's parameter and the masses of galaxies from the gravitational lens effect*, *Monthly Notices of the Royal Astronomical Society* **128** (1964) 307.

[6] D. Paraficz and J. Hjorth, *Gravitational lenses as cosmic rulers: Ω_m, Ω_Λ from time delays and velocity dispersions*, *Astronomy and Astrophysics* **507** (2009) L49 [0910.5823].

[7] E.V. Linder, *Lensing time delays and cosmological complementarity*, *Physical Review D* **84** (2011) 123529 [1109.2592].

[8] T. Treu and P.J. Marshall, *Time delay cosmography*, *Astronomy and Astrophysics Reviews* **24** (2016) 11 [1605.05333].

[9] T. Treu, S.H. Suyu and P.J. Marshall, *Strong lensing time-delay cosmography in the 2020s*, *Astronomy and Astrophysics Reviews* **30** (2022) 8 [2210.15794].

[10] S. Birrer, M. Millon, D. Sluse, A.J. Shajib, F. Courbin, L.V.E. Koopmans et al., *Time-Delay Cosmography: Measuring the Hubble Constant and other cosmological parameters with strong gravitational lensing*, *arXiv e-prints* (2022) arXiv:2210.10833 [2210.10833].

[11] A.G. Riess, L. Breuval, W. Yuan, S. Casertano, L.M. Macri, J.B. Bowers et al., *Cluster Cepheids with High Precision Gaia Parallaxes, Low Zero-point Uncertainties, and Hubble Space Telescope Photometry*, *Astrophysical Journal* **938** (2022) 36 [2208.01045].

[12] K.C. Wong, S.H. Suyu, G.C.F. Chen, C.E. Rusu, M. Millon, D. Sluse et al., *H0LiCOW - XIII. A 2.4 per cent measurement of H_0 from lensed quasars: 5.3σ tension between early- and late-Universe probes*, *Monthly Notices of the Royal Astronomical Society* **498** (2020) 1420 [1907.04869].

[13] Planck Collaboration, N. Aghanim, Y. Akrami, M. Ashdown, J. Aumont, C. Baccigalupi et al., *Planck 2018 results. VI. Cosmological parameters*, *Astronomy and Astrophysics* **641** (2020) A6 [1807.06209].

[14] T.M.C. Abbott, M. Aguena, A. Alarcon, S. Allam, O. Alves, A. Amon et al., *Dark Energy Survey Year 3 results: Cosmological constraints from galaxy clustering and weak lensing*, *Physical Review D* **105** (2022) 023520 [2105.13549].

[15] X. Ding, K. Liao, S. Birrer, A.J. Shajib, T. Treu and L. Yang, *Improved time-delay lens modelling and H_0 inference with transient sources*, *Monthly Notices of the Royal Astronomical Society* **504** (2021) 5621 [2103.08609].

[16] S.S. Tie and C.S. Kochanek, *Microlensing makes lensed quasar time delays significantly time variable*, *Monthly Notices of the Royal Astronomical Society* **473** (2018) 80 [1707.01908].

[17] V. Bonvin, O. Tihhonova, M. Millon, J.H.H. Chan, E. Savary, S. Huber et al., *Impact of the 3D source geometry on time-delay measurements of lensed type-Ia supernovae*, *Astronomy and Astrophysics* **621** (2019) A55 [1805.04525].

[18] M. Foxley-Marrable, T.E. Collett, G. Vernardos, D.A. Goldstein and D. Bacon, *The impact of microlensing on the standardization of strongly lensed Type Ia supernovae*, *Monthly Notices of the Royal Astronomical Society* **478** (2018) 5081 [1802.07738].

[19] S. Huber, S.H. Suyu, U.M. Noebauer, V. Bonvin, D. Rothchild, J.H.H. Chan et al., *Strongly lensed SNe Ia in the era of LSST: observing cadence for lens discoveries and time-delay measurements*, *Astronomy and Astrophysics* **631** (2019) A161 [1903.00510].

[20] A. Goobar, R. Amanullah, S.R. Kulkarni, P.E. Nugent, J. Johansson, C. Steidel et al., *iPTF16geu: A multiply imaged, gravitationally lensed type Ia supernova*, *Science* **356** (2017) 291 [1611.00014].

[21] J.D.R. Pierel, N. Arendse, S. Ertl, X. Huang, L.A. Moustakas, S. Schuldt et al., *LensWatch. I. Resolved HST Observations and Constraints on the Strongly Lensed Type Ia Supernova 2022qmx ("SN Zwicky")*, *Astrophysical Journal* **948** (2023) 115 [2211.03772].

[22] P.L. Kelly, S.A. Rodney, T. Treu, R.J. Foley, G. Brammer, K.B. Schmidt et al., *Multiple images of a highly magnified supernova formed by an early-type cluster galaxy lens*, *Science* **347** (2015) 1123 [1411.6009].

[23] C. Grillo, P. Rosati, S.H. Suyu, I. Balestra, G.B. Caminha, A. Halkola et al., *Measuring the Value of the Hubble Constant "à la Refsdal"*, *Astrophysical Journal* **860** (2018) 94 [1802.01584].

[24] P.L. Kelly, S. Rodney, T. Treu, S. Birrer, V. Bonvin, L. Dessart et al., *The Magnificent Five Images of Supernova Refsdal: Time Delay and Magnification Measurements*, *Astrophysical Journal* **948** (2023) 93 [2305.06377].

[25] S.A. Rodney, G.B. Brammer, J.D.R. Pierel, J. Richard, S. Toft, K.F. O'Connor et al., *A gravitationally lensed supernova with an observable two-decade time delay*, *Nature Astronomy* **5** (2021) 1118 [2106.08935].

[26] A. Goobar, J. Johansson, S. Schulze, N. Arendse, A. Sagués Carracedo, S. Dhawan et al., *Uncovering a population of gravitational lens galaxies with magnified standard candle SN Zwicky*, *arXiv e-prints* (2022) arXiv:2211.00656 [2211.00656].

[27] B. Frye, M. Pascale, S. Cohen, J. Summers, N. Foo, P. Kamieneski et al., *SN H0pe: three images of a SN detected near the central region of the galaxy cluster field PLCK G165.7+67.0*, *Transient Name Server AstroNote* **96** (2023) 1.

[28] A.G. Riess, A.V. Filippenko, P. Challis, A. Clocchiatti, A. Diercks, P.M. Garnavich et al., *Observational Evidence from Supernovae for an Accelerating Universe and a Cosmological Constant*, *Astronomical Journal* **116** (1998) 1009 [astro-ph/9805201].

[29] S. Perlmutter, G. Aldering, G. Goldhaber, R.A. Knop, P. Nugent, P.G. Castro et al., *Measurements of* Ω *and* Λ *from 42 High-Redshift Supernovae*, *Astrophysical Journal* **517** (1999) 565 [astro-ph/9812133].

[30] E.Y. Hsiao, A. Conley, D.A. Howell, M. Sullivan, C.J. Pritchet, R.G. Carlberg et al., *K-Corrections and Spectral Templates of Type Ia Supernovae*, *Astrophysical Journal* **663** (2007) 1187 [astro-ph/0703529].

[31] W.D. Kenworthy, D.O. Jones, M. Dai, R. Kessler, D. Scolnic, D. Brout et al., *SALT3: An Improved Type Ia Supernova Model for Measuring Cosmic Distances*, *Astrophysical Journal* **923** (2021) 265 [2104.07795].

[32] J.D.R. Pierel, D.O. Jones, W.D. Kenworthy, M. Dai, R. Kessler, C. Ashall et al., *SALT3-NIR: Taking the Open-source Type Ia Supernova Model to Longer Wavelengths for Next-generation Cosmological Measurements*, *Astrophysical Journal* **939** (2022) 11 [2209.05594].

[33] E.E. Falco, M.V. Gorenstein and I.I. Shapiro, *On model-dependent bounds on H 0 from gravitational images : application to Q 0957+561 A, B.*, *Astrophysical Journal Letters* **289** (1985) L1.

[34] M. Oguri and Y. Kawano, *Gravitational lens time delays for distant supernovae: breaking the degeneracy between radial mass profiles and the*

Hubble constant, *Monthly Notices of the Royal Astronomical Society* **338** (2003) L25 [astro-ph/0211499].

[35] B.M. Rose, C. Baltay, R. Hounsell, P. Macias, D. Rubin, D. Scolnic et al., *A Reference Survey for Supernova Cosmology with the Nancy Grace Roman Space Telescope*, *arXiv e-prints* (2021) arXiv:2111.03081 [2111.03081].

[36] M. Oguri and P.J. Marshall, *Gravitationally lensed quasars and supernovae in future wide-field optical imaging surveys*, *Monthly Notices of the Royal Astronomical Society* **405** (2010) 2579 [1001.2037].

[37] R. Wojtak, J. Hjorth and C. Gall, *Magnified or multiply imaged? - Search strategies for gravitationally lensed supernovae in wide-field surveys*, *Monthly Notices of the Royal Astronomical Society* **487** (2019) 3342 [1903.07687].

[38] D.A. Goldstein, P.E. Nugent and A. Goobar, *Rates and Properties of Supernovae Strongly Gravitationally Lensed by Elliptical Galaxies in Time-domain Imaging Surveys*, *The Astrophysical Journal Supplement Series* **243** (2019) 6 [1809.10147].

[39] B.W. Holwerda, S. Knabel, R.C. Steele, L. Strolger, J. Kielkopf, A. Jacques et al., *The observable supernova rate in galaxy-galaxy lensing systems with the TESS satellite*, *Monthly Notices of the Royal Astronomical Society* **505** (2021) 1316 [2104.11654].

[40] A. Sainz de Murieta, T.E. Collett, M.R. Magee, L. Weisenbach, C.M. Krawczyk and W. Enzi, *Lensed type Ia supernovae in light of SN Zwicky and iPTF16geu*, *arXiv e-prints* (2023) arXiv:2307.12881 [2307.12881].

[41] T. Petrushevska, R. Amanullah, A. Goobar, S. Fabbro, J. Johansson, T. Kjellsson et al., *High-redshift supernova rates measured with the gravitational telescope A 1689*, *Astronomy and Astrophysics* **594** (2016) A54 [1607.01617].

[42] T. Petrushevska, A. Goobar, D.J. Lagattuta, R. Amanullah, L. Hangard, S. Fabbro et al., *Searching for supernovae in the multiply-imaged galaxies behind the gravitational telescope A370*, *Astronomy and Astrophysics* **614** (2018) A103 [1802.10525].

[43] T. Petrushevska, T. Okamura, R. Kawamata, L. Hangard, G. Mahler and A. Goobar, *Prospects for Strongly Lensed Supernovae Behind Hubble*

Frontier Fields Galaxy Clusters with the James Webb Space Telescope, *Astronomy Reports* **62** (2018) 917 [1901.02014].

[44] C. Cerny, K. Sharon, F. Andrade-Santos, R.J. Avila, M. Bradač, L.D. Bradley et al., *RELICS: Strong Lens Models for Five Galaxy Clusters from the Reionization Lensing Cluster Survey*, *Astrophysical Journal* **859** (2018) 159 [1710.09329].

[45] N. Cibirka, A. Acebron, A. Zitrin, D. Coe, I. Agulli, F. Andrade-Santos et al., *RELICS: Strong Lensing Analysis of the Galaxy Clusters Abell S295, Abell 697, MACS J0025.4-1222, and MACS J0159.8-0849*, *Astrophysical Journal* **863** (2018) 145 [1803.09557].

[46] A. Acebron, M. Alon, A. Zitrin, G. Mahler, D. Coe, K. Sharon et al., *RELICS: High-resolution Constraints on the Inner Mass Distribution of the z = 0.83 Merging Cluster RXJ0152.7-1357 from Strong Lensing*, *Astrophysical Journal* **874** (2019) 132 [1810.08122].

[47] A. Acebron, N. Cibirka, A. Zitrin, D. Coe, I. Agulli, K. Sharon et al., *RELICS: Strong-lensing Analysis of the Massive Clusters MACS J0308.9+2645 and PLCK G171.9-40.7*, *Astrophysical Journal* **858** (2018) 42 [1803.00560].

[48] G. Mahler, K. Sharon, C. Fox, D. Coe, M. Jauzac, V. Strait et al., *RELICS: Strong Lensing Analysis of MACS J0417.5-1154 and Predictions for Observing the Magnified High-redshift Universe with JWST*, *Astrophysical Journal* **873** (2019) 96 [1810.13439].

[49] A. Zitrin, S. Seitz, A. Monna, A.M. Koekemoer, M. Nonino, D. Gruen et al., *A Very Large ($\theta_E \gtrsim 40$") Strong Gravitational Lens Selected with the Sunyaev-Zel'dovich Effect: PLCK G287.0+32.9 (z = 0.38)*, *Astrophysical Journal Letters* **839** (2017) L11 [1702.05090].

[50] A. Acebron, A. Zitrin, D. Coe, G. Mahler, K. Sharon, M. Oguri et al., *RELICS: A Very Large ($\theta_E \sim 40$") Cluster Lens—RXC J0032.1+1808*, *Astrophysical Journal* **898** (2020) 6 [1912.02702].

[51] R. Paterno-Mahler, K. Sharon, D. Coe, G. Mahler, C. Cerny, T.L. Johnson et al., *RELICS: A Strong Lens Model for SPT-CLJ0615-5746, a z = 0.972 Cluster*, *Astrophysical Journal* **863** (2018) 154 [1805.09834].

[52] J. Richard, A. Claeyssens, D. Lagattuta, L. Guaita, F.E. Bauer, R. Pello et al., *An atlas of MUSE observations towards twelve massive lensing clusters*, *Astronomy and Astrophysics* **646** (2021) A83 [2009.09784].

[53] A. Zitrin, A. Fabris, J. Merten, P. Melchior, M. Meneghetti, A. Koekemoer et al., *Hubble Space Telescope Combined Strong and Weak Lensing Analysis of the CLASH Sample: Mass and Magnification Models and Systematic Uncertainties*, *Astrophysical Journal* **801** (2015) 44 [1411.1414].

[54] G.B. Caminha, P. Rosati, C. Grillo, G. Rosani, K.I. Caputi, M. Meneghetti et al., *Strong lensing models of eight CLASH clusters from extensive spectroscopy: Accurate total mass reconstructions in the cores*, *Astronomy and Astrophysics* **632** (2019) A36 [1903.05103].

[55] A. Zitrin, A. Acebron, D. Coe, P.L. Kelly, A.M. Koekemoer, M. Nonino et al., *A Strong-lensing Model for the WMDF JWST/GTO Very Rich Cluster A1489*, *Astrophysical Journal* **903** (2020) 137 [2007.11600].

[56] B. Salmon, D. Coe, L. Bradley, R. Bouwens, M. Bradač, K.-H. Huang et al., *RELICS: The Reionization Lensing Cluster Survey and the Brightest High-z Galaxies*, *Astrophysical Journal* **889** (2020) 189 [1710.08930].

[57] R. Bacon, M. Accardo, L. Adjali, H. Anwand, S. Bauer, I. Biswas et al., *The MUSE second-generation VLT instrument*, in *Ground-based and Airborne Instrumentation for Astronomy III*, I.S. McLean, S.K. Ramsay and H. Takami, eds., vol. 7735 of *Society of Photo-Optical Instrumentation Engineers (SPIE) Conference Series*, p. 773508, July, 2010, DOI [2211.16795].

[58] E.E. Salpeter, *The Luminosity Function and Stellar Evolution.*, *Astrophysical Journal* **121** (1955) 161.

[59] M. Vincenzi, M. Sullivan, R.E. Firth, C.P. Gutiérrez, C. Frohmaier, M. Smith et al., *Spectrophotometric templates for core-collapse supernovae and their application in simulations of time-domain surveys*, *Monthly Notices of the Royal Astronomical Society* **489** (2019) 5802 [1908.05228].

[60] I. Shivvers, M. Modjaz, W. Zheng, Y. Liu, A.V. Filippenko, J.M. Silverman et al., *Revisiting the Lick Observatory Supernova Search Volume-limited Sample: Updated Classifications and Revised Stripped-envelope Supernova Fractions*, *Publications of the ASP* **129** (2017) 054201 [1609.02922].

[61] W. Li, J. Leaman, R. Chornock, A.V. Filippenko, D. Poznanski, M. Ganeshalingam et al., *Nearby supernova rates from the Lick Observatory Supernova Search - II. The observed luminosity functions and fractions of supernovae in a complete sample*, *Monthly Notices of the Royal Astronomical Society* **412** (2011) 1441 [1006.4612].

[62] E. Scannapieco and L. Bildsten, *The Type Ia Supernova Rate*, *Astrophysical Journal Letters* **629** (2005) L85 [astro-ph/0507456].

[63] P. Andersen and J. Hjorth, *Reconciling volumetric and individual galaxy type Ia supernova rates*, *Monthly Notices of the Royal Astronomical Society* **480** (2018) 68 [1801.00793].

[64] M. Smith, R.C. Nichol, B. Dilday, J. Marriner, R. Kessler, B. Bassett et al., *The SDSS-II Supernova Survey: Parameterizing the Type Ia Supernova Rate as a Function of Host Galaxy Properties*, *Astrophysical Journal* **755** (2012) 61 [1108.4923].

[65] R. Kessler, J.P. Bernstein, D. Cinabro, B. Dilday, J.A. Frieman, S. Jha et al., *SNANA: A Public Software Package for Supernova Analysis*, *Publications of the ASP* **121** (2009) 1028 [0908.4280].

[66] L.-G. Strolger, T. Dahlen, S.A. Rodney, O. Graur, A.G. Riess, C. McCully et al., *The Rate of Core Collapse Supernovae to Redshift 2.5 from the CANDELS and CLASH Supernova Surveys*, *Astrophysical Journal* **813** (2015) 93 [1509.06574].

[67] L.-G. Strolger, S.A. Rodney, C. Pacifici, G. Narayan and O. Graur, *Delay Time Distributions of Type Ia Supernovae from Galaxy and Cosmic Star Formation Histories*, *Astrophysical Journal* **890** (2020) 140 [2001.05967].

[68] Astropy Collaboration, A.M. Price-Whelan, P.L. Lim, N. Earl, N. Starkman, L. Bradley et al., *The Astropy Project: Sustaining and Growing a Community-oriented Open-source Project and the Latest Major Release (v5.0) of the Core Package*, *Astrophysical Journal* **935** (2022) 167 [2206.14220].

[69] J.D. Hunter, *Matplotlib: A 2d graphics environment*, *Computing in Science & Engineering* **9** (2007) 90.

[70] M. Boquien, D. Burgarella, Y. Roehlly, V. Buat, L. Ciesla, D. Corre et al., *CIGALE: a python Code Investigating GALaxy Emission*, *Astronomy and Astrophysics* **622** (2019) A103 [1811.03094].

[71] S. Noll, D. Burgarella, E. Giovannoli, V. Buat, D. Marcillac and J.C. Muñoz-Mateos, *Analysis of galaxy spectral energy distributions from far-UV to far-IR with CIGALE: studying a SINGS test sample*, *Astronomy and Astrophysics* **507** (2009) 1793 [0909.5439].

[72] D. Burgarella, V. Buat and J. Iglesias-Páramo, *Star formation and dust attenuation properties in galaxies from a statistical ultraviolet-to-far-infrared analysis*, *Monthly Notices of the Royal Astronomical Society* **360** (2005) 1413 [astro-ph/0504434].

Review on Photoconductivity Measurements in Organic Semiconductor and 2D Materials using Scanning Near Field Optical Microscopy

Lakshmi Rajan

University of Nova Gorica, Vipavska 13, SI-5000 Nova Gorica

Abstract

Organic semiconductor/2D materials heterostructures have emerged as promising contenders for next-generation optoelectronic devices, leveraging their unique electronic and optical properties. Comprehending the intricate photoconductivity dynamics within these heterogeneous structures stands pivotal in optimizing their performance and unlocking novel applications. To unravel the elusive photoconductive behavior in these systems, Scanning Near Field Optical Microscopy (SNOM) has emerged as an instrumental technique, offering exceptional spatial resolution and sensitivity.This comprehensive review elucidates recent strides in photoconductivity measurements within organic semiconductor and 2D materials heterostructures using SNOM.

Keywords: Organic semiconductor, 2D materials, photoconductivity, SNOM

1. Introduction

The synergy between organic semiconductors [1] and 2D materials [2] in heterostructures allows for the exploitation of the distinct advantages of each component while compensating for their individual limitations. The interface between these materials can lead to new physics and novel optoelectronic phenomena, such as exciton dissociation and charge transfer processes, which are essential for efficient light harvesting and device operation. At the heart of harnessing their full potential lies a profound understanding of their photoconductive behavior - a pivotal property governing the efficient conversion of light into electrical signals. As a result, researchers have sought sophisticated techniques to probe the photoconductivity intricacies within these heterostructures with exceptional precision. Among these, Scanning Near Field Optical Microscopy (SNOM) [3] has garnered significant attention and acclaim for its unmatched capability to explore local optoelectronic

Email address: lakshmi.rajan@ung.si (Lakshmi Rajan)

properties with nanoscale resolution. By integrating optical microscopy with scanning probe microscopy, SNOM surpasses the diffraction limit of traditional optical techniques, enabling unprecedented insights into light-matter interactions at the nanoscale.

This review aims to provide an extensive survey of recent advancements in photoconductivity measurements within organic semiconductor and 2D materials heterostructures utilizing SNOM as a cutting-edge investigative tool. First, we lay the groundwork by elucidating the fundamental principles of photoconductivity in organic semiconductors and 2D materials (Section 2), as well as the working principles of SNOM (Section 3). Subsequently, we delve into a meticulous exposition of key findings from diverse studies, showcasing how SNOM has unveiled the intriguing photoconductivity dynamics of various heterostructures (Section 4), while being organized according to materials and experimental approaches.

2. Fundamental Principles of Photoconductivity

Photoconductivity has been a significant focus in materials research. This phenomenon involves an increase in electrical conductivity when materials absorb photons, resulting in photocurrent. It depends on photon absorption, carrier transport, and recombination of photo-excited carriers. Analyzing these aspects under varying illumination conditions and observing their temporal evolution provides insights into the material's structure and electronic properties. Experimental techniques based on photoconductivity can be categorized into steady-state photoconductivity (SSPC) and transient effects (TPC) [4]. SSPC focuses on examining stationary photocurrent levels, while TPC studies the time evolution of photocurrents, offering insights into recombination processes.

2.1. Steady state photoconductivity measurements (SSPC)

2.1.1. Single beam experiment

Equal densities of electrons and holes ($\Delta n = \Delta p$) can be created by using a constant monochromatic light source. This alters the conductivity by,

$$\Delta\sigma = \sigma_{p_h} = e(\mu_n \Delta n + \mu_p \Delta p) \tag{1}$$

where e is the electric charge and μ_n , μ_p are the electron and hole mobility.

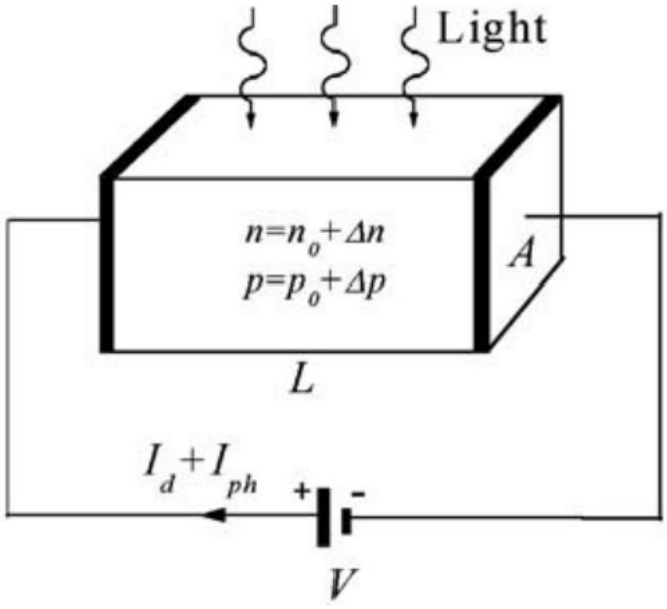

Figure 1: Schematic representation of the photoconductivity measurements with V the voltage applied and L, respectively A, the sample length and the cross-sectional area. I_d, n_0, p_0 are the current and the carrier densities in the dark, and I_{ph}, Δn, Δp are the incremental values caused by the illumination.

In practical scenarios, some of the photogenerated carriers get trapped at defects, leading to unequal contributions of Δn and Δp to the photoconductivity in Equation 1. This trapping effect is manifested in lower mobilities μ_n and μ_p compared to the theoretical free-carrier mobility. Interestingly, many widely used materials exhibit significantly unequal carrier mobilities, resulting in one of the terms in Equation 1 being much larger than the other. For example, in intrinsic silicon, the electron term dominates, while in chalcogenide glasses, the photocurrent is mainly carried by holes. In such instances, Equation 1 effectively simplifies to a one-carrier equation.

2.1.2. The constant photocurrent method (CPM)

The constant photocurrent method (CPM) was introduced [5, 6] as a technique to determine the optical absorption coefficient (α) as a function of photon energy (E). In CPM, the photocurrent is maintained at a constant level by continuously adjusting the light intensity (I_0) while scanning the photon energy across the spectrum. This constant photocurrent condition implies a stationary position of the quasi-Fermi levels and thus a constant free carrier lifetime (τ). By considering the expression,

$$\sigma_{p_h} = e\mu\tau \left(\frac{I_0}{h\nu}\right)(1-R)\eta\alpha \tag{2}$$

where σ_{p_h} is the photocurrent, e is the electronic charge, μ is the carrier mobility, R represents recombination effects, and η is the quantum efficiency of carrier genera-

tion and the product $\frac{I_0}{h\nu}$ remains constant. This constancy allows the determination of α from the measurement, provided that the energy dependence of μ, R, and η in Equation 2 is negligible.

2.1.3. Dual beam photoconductivity (DBP)

Similar to the constant photocurrent method (CPM) described earlier, the dual-beam photoconductivity (DBP) technique also aims to determine the sub-bandgap optical absorption in a photoconductor. In DBP, a constant and uniformly absorbed light intensity I_0 is used to create a stable excess carrier density and free-carrier lifetime τ in the material. In this setup, a low-intensity, tunable light source produces a chopped signal (I_E) that is added to the background illumination. This combination generates small variations in photoconductivity ($\delta\sigma_{p_h}$(E)). By using synchronous lock-in detection of this AC signal, one can obtain the necessary information to deduce the optical absorption coefficient (α(E)). DBP allows to perform measurements with varying background illumination intensities. This allows testing the photoconductor absorption at different positions of its quasi-Fermi levels, which are related to the distribution of electronic states known as the density of states (DOS) in the material.

2.1.4. Modulated photoconductivity (MPC)

The experimental technique known as Modulated Photoconductivity (MPC) aims to determine the distribution of states within the bandgap of a photoconductor by analyzing the phase shift between an alternating current (AC) photo-excitation and the resulting AC photocurrent at different modulation frequencies of the light [7, 8]. The MPC setup, shown in Fig 2, illustrates the phase difference between the illumination and the photocurrent.

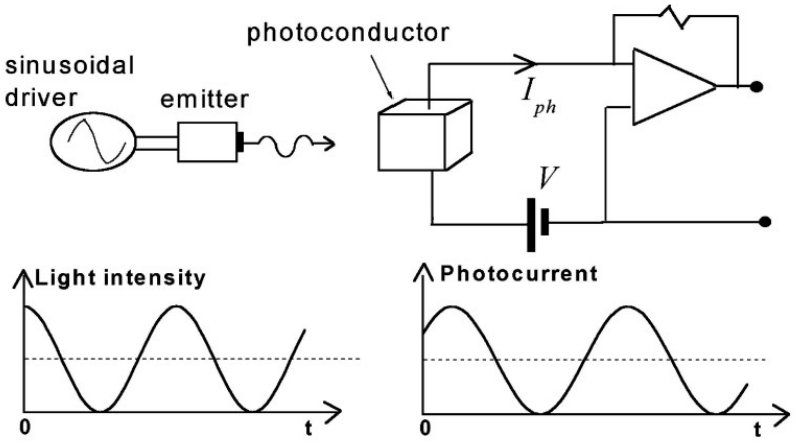

Figure 2: Schematic diagram of a MPC set-up, and the phase relationship between exciting light intensity and the resulting photocurrent (lower frames).

Two distinct modulation frequency ranges have been identified. In the high-frequency region, typically from a few Hz to the kHz range, the signal is mainly influenced by carrier release from traps, where the release rate matches the modulation frequency. By assuming that the release probability from traps decreases exponentially with trap depth, the measured phase shift can be linked to the DOS of the material. The relationship between the phase shift and the DOS is expressed by the following equation:

$$g(E) \propto \frac{\sin(\theta)}{I_{a_c}}, E = KT \ln \frac{\nu_0}{\omega}$$

where θ and I_{a_c} are the phase and intensity of the AC photocurrent, K is the Boltzmann constant, T is the temperature, ν_0 is the attempt-to-escape frequency, ω is the modulation frequency and E is the energy. In the low-frequency region, the phase shifts are determined by recombination and trapping in deep states, and the DOS varies according to $\tan(\theta)/\omega$. The transition between these two regions depends on the position of the quasi-Fermi levels, which can be adjusted by changing the illumination intensity. MPC is most effective in photoconductors where one carrier type dominates the current, allowing for the analysis to focus on one side of the bandgap.

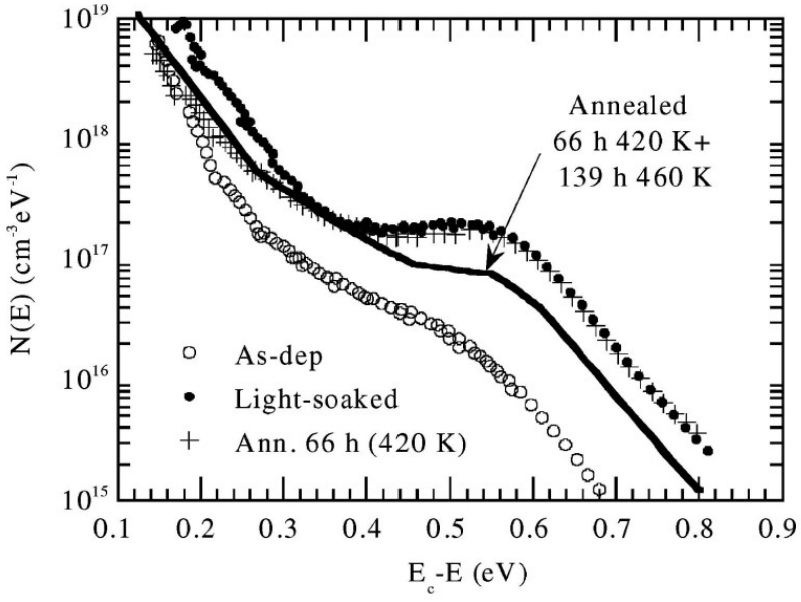

Figure 3: DOS below the conduction band (CB) edge of a polymorphous silicon sample deposited at 423 K, and measured by MPC as-deposited, after light soaking, and after two stages of subsequent annealing [9].

Fig. 3 presents an example of DOS profiles determined using MPC. It shows the conduction-band side of the bandgap of a polymorphous silicon sample, both as-deposited and after light soaking and subsequent annealing [9]. MPC provides valuable information about the electronic properties of the material, especially when one carrier type is prevalent, and helps to study changes in the bandgap structure due to external factors like light soaking and annealing.

2.2. Transient photoconductivity measurements (TPC)

Transient photoconductivity (TPC) is a fascinating area of study that involves investigating how photocurrents evolve during their buildup or relaxation and how materials respond to pulsed excitation. When examining steady state photoconductivity (SSPC), the initial turn-on transient, which results from the complex interplay between carrier generation and recombination was observed. At high excitation levels, this interplay can lead to interesting phenomena, such as current overshoots. Conversely, the relaxation of SSPC when turning off the excitation is relatively easier to analyze, primarily involving carrier recombination. On the other hand, TPC experiments, utilizing pulsed excitation, offer a more straightforward analysis. Unlike in SSPC, TPC measurements do not need to consider the quasi-equilibrium distribution of trapped photogenerated carriers in the material. Instead, they can be analyzed in the context of the thermal equilibrium distribution of carriers present in the material. The study of transient photoconductivity provides valuable insights into the dynamic behavior of carriers in materials. Whether observing photocurrent buildup or decay, or studying the response to pulsed excitation, different experimental approaches offer unique advantages, contributing to a deeper understanding of the fascinating photoelectric properties of materials.

2.2.1. Current relaxation from the steady state

When the steady state illumination is stopped, the rate equation governing the non-equilibrium carrier distribution no longer includes the generation term. However, the carrier density and the recombination process remain unchanged. As a result, the initial decay of the photocurrent will be determined by the same recombination mode that existed under SSPC conditions. For monomolecular recombination, a spectroscopic analysis of the relaxation current can be easily achieved, where the product of the photocurrent and time is proportional to the DOS in the bandgap [10]. The relationship is expressed as

$$I_{p_h}(t)t \propto g(E), E = KT\ln(\nu_0 t) \tag{3}$$

On the other hand, when bimolecular recombination dominates, the connection between the current and the distribution of recombination centers is less straightforward, making spectroscopic analysis challenging. Unfortunately, bimolecular recombination is common in good photoconductors. Despite the complexities, relaxation of the steady state current has been used to estimate free carrier lifetimes,

often on a phenomenological basis due to limited information on the involved recombination mechanisms. In such cases, an exponential fit to the initial decay is often utilized for making the estimate. However, when different recombination mechanisms are at play, the initial decay might not represent the most significant aspect of carrier behavior. This situation arises, for example, when observing persistent photoconductivity, where one of the relaxation times involved is longer than the observation time.

2.2.2. Transient photoconductivity

In the standard TPC experiment, free carriers are excited into the transport band by a brief light pulse at t = 0. These carriers then move under the influence of an electric field until they recombine. Along their journey, they encounter various traps in the material, causing them to be immobilized multiple times. At the beginning of the experiment, the carrier distributions are in thermal equilibrium, and both the trapping sites for electrons above the Fermi level and the hole trapping sites below E_F are vacant, allowing the newly created carriers to access all trapping sites. Carrier release from traps is a thermally activated process, where deeper traps immobilize carriers for longer times, leading to lower transient currents. As shallower traps release trapped carriers sooner, re-trapping occurs, resulting in more carriers occupying deeper states and further reducing the current. To study the thermalization of excited carriers until recombination takes place, the experiments are typically conducted in the secondary photocurrent mode, with ohmic electrical contacts applied to the sample, ensuring that carrier loss is solely due to recombination. Gap cells with co-planar electrode geometries are often used.

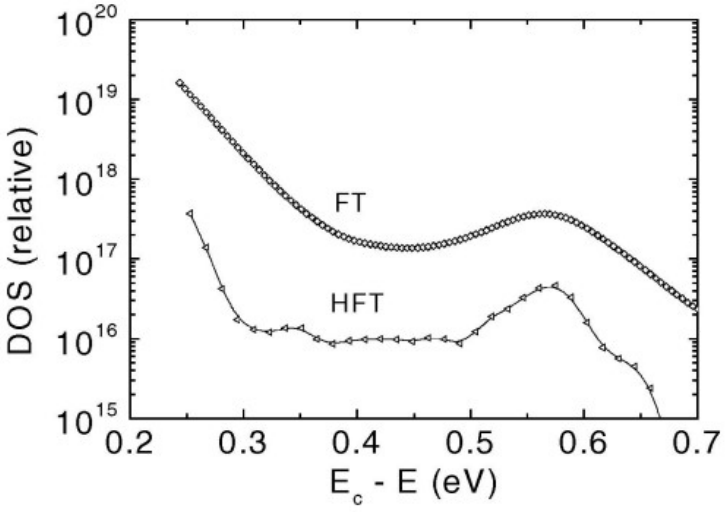

Figure 4: DOS below the conduction band edge in a-Si:H, obtained through Fourier transforms of the transient photocurrent [11, 12].

An alternative approach to tackle the challenges in analyzing the transient current is by performing a Fourier transform [11], which translates the current decay into the frequency domain. This Fourier transform reveals the frequency response I(ω) of the photoconductor, equivalent to the photocurrent intensity I_{a_c} used in the MPC method. Using similar procedures, valuable information on the density and energy distribution of localized states within the bandgap can be extracted. Both Fourier and Laplace transform techniques have been employed to convert TPC signals into DOS information [12]. The application of Fourier-transform TPC analysis to an a-Si:H sample is exemplified in Fig.4, illustrating its potential for understanding the energy range probed in comparison to the limitations of MPC.

2.2.3. Time-of-Flight photoconductivity measurements

The time-of-flight (TOF) experiment, originally designed to determine the drift mobility of free carriers in high-mobility materials, has been particularly successful when adapted for low-mobility materials like organic or amorphous semiconductors [13]. In these materials, it has been effectively used for both drift mobility measurements and as an alternative transient photoconductivity (TPC) technique to investigate the energy distribution of localized states.

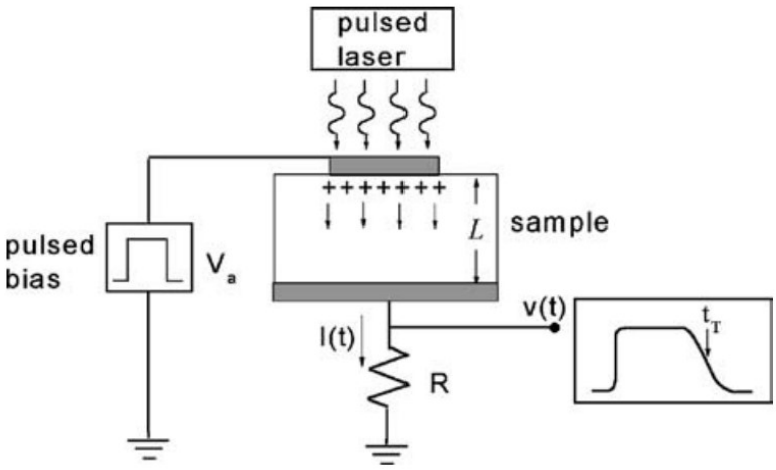

Figure 5: Time-of-flight (TOF) measurement setup for hole drift in the sample's length L under the influence of a positive applied voltage. The resistor R can be adjusted to a low value to minimize RC distortion at short times, or to a high value to enhance the detectability of weak signals at the expense of time resolution.

In TOF measurements, the sample comprises a layer of the photoconducting material positioned between two electrodes (Fig.5), which act as barriers for carrier injection into the sample. At least one of the electrodes must be semi-transparent to enable photo-excitation of free carriers in the material just beyond the illuminated contact, triggered by an intense light flash. Depending on the electric field's polarity applied across the sample, either electrons or holes will be drifted through the material[14]. Upon reaching the back contact, the current drops as the blocking contact ensures that only the primary photocurrent is measured. The drift mobility (μ_d) can then be calculated using the transit time (t_T), which is the time it takes for the charge sheet to cross the sample. The relationship is expressed as $\mu_d = \frac{L}{t_T}$ F, where L is the sample length, and F is the applied electric field. The transit time can be measured directly from the current trace, with varying definitions, such as the time when the current drops by 10% to 50% (the latter being more commonly used). Alternatively, it can be obtained by integrating the current and determining the time at which the collected charge saturates. To ensure an accurate value of μ_d, the applied electric field (F) must be uniform and constant during the carrier transit. This necessitates applying F only a short time before the optical excitation and ensuring the transit time is short compared to the material's dielectric relaxation time.

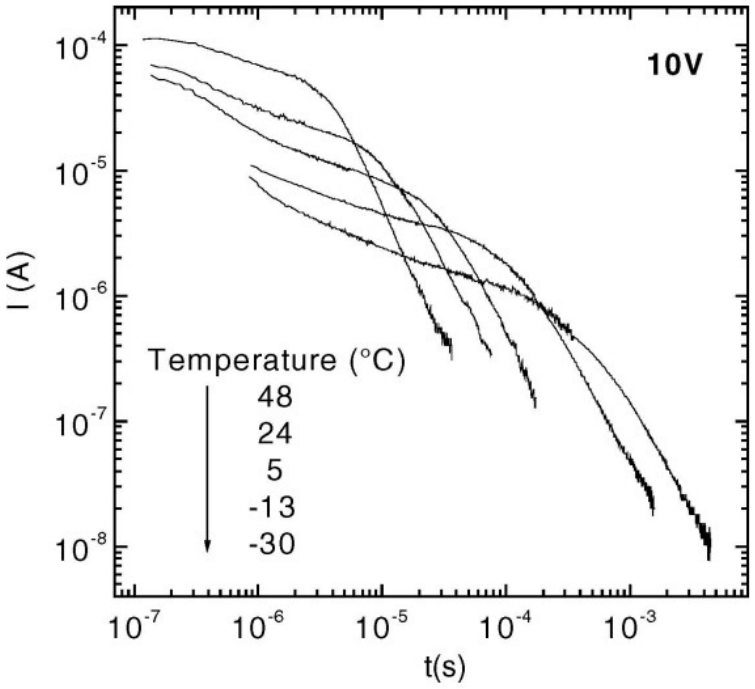

Figure 6: TOF hole transients measured at different temperatures with a 10 V applied voltage across a 5.6 µm thick a-Si:H sample. The sample was grown in an expanding thermal plasma at a substrate temperature of 250°C and sandwiched between Mo contacts [15].

In materials with a wide distribution of localized gap states, such as disordered photoconductors, the drifting charge package spreads along the sample's length. To identify a representative transit time, researchers analyze the current versus time plot using a double-logarithmic scale, as depicted in Fig.6 [15]. To ensure that the observed feature indeed indicates carrier transit and not deep trapping of the photogenerated charge, measurements at various temperatures and applied fields are required. In materials exhibiting this anomalously dispersive transport, the pre-transit current demonstrates characteristics similar to those observed in the TPC explained earlier. Therefore, information about the distribution of gap states (g(E)) contained in the current transient can be extracted using the same methods. In the past, both the pre-transit current transients and the measured drift mobility values were utilized to estimate the DOS in the band tails of disordered semiconductors. For this purpose, trap-controlled transport modeling was employed to reproduce the experimental variation of μ_d with temperature and electric field.

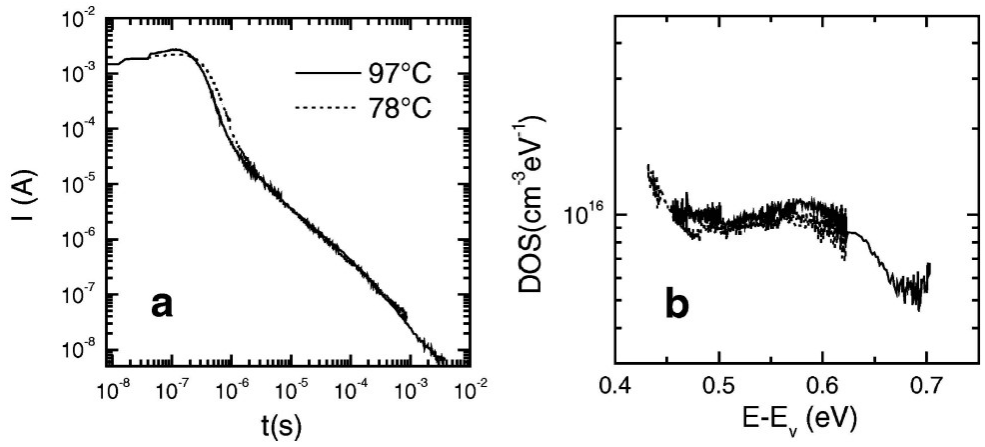

Figure 7: (a)TOF hole transients, displaying the post-transit regime, obtained from a 2 µm thick a-Si:H sample grown at a rate of 6 nm/s and 450°C, with an applied voltage of 10 V. (b) The corresponding DOS profile is calculated, with $Q_0 = 2 \times 10^{-9}$ C, $\nu = 10^{12}$ s^{-1}, $g(0) = 10^{21}$ cm^{-3} eV^{-1}, and $\mu_0 = 8$ cm^2 V^{-1} s^{-1} [16]).

For times longer than the TOF transit time, a steeper current decay indicates that carriers are leaving the sample. The post-transit current observed at this stage is primarily due to carriers emitted from deep states within the bandgap, where they were initially trapped. By analyzing these post-transit TOF current transients appropriately, researchers can gain insights into the distribution of localized states deeper within the gap [17]. This analysis corresponds to the relationship $g(E) \ \alpha \ [I(t)t]$ as shown in Equation 3. An example of such post-transit analysis, revealing the DOS on the valence band side of a hydrogenated amorphous silicon sample is illustrated in Fig.7.

2.2.4. Interrupted field time-of-flight

The interrupted field time-of-flight (IFTOF) experiment differs from the previous time-of-flight experiment in a crucial way. In IFTOF, the applied electric field that propels the photogenerated carriers through the sample is temporarily turned off before the carriers have completed their transit. When the field is turned on again, a lower current intensity is measured, indicating that some of the drifting carriers have become trapped in deep states [18]. By studying the current drop as a function of the interruption time, the deep-trapping lifetime of the carriers can be assessed. Typically, recombination can be disregarded in time-of-flight experiments since only one type of carrier drifts through the sample. However, by initially charging the sample with carriers of one polarity and then conducting an IFTOF experiment that drifts carriers of the opposite polarity through the sample, recombination parameters can also be studied [19].

Another intriguing approach to study the recombination process is a modification of the TOF experiment. After generating free carriers through one contact and drifting the slower type of carrier into the sample, a second light pulse through the other contact launches a sheet of carriers with opposite charges towards the first one. During their crossing, some electrons and holes recombine, the observed current levels provides insights into the recombination process [20].

3. Scanning Near-Field Optical Microscopy (SNOM)

Scanning near-field optical microscopy (SNOM or NSOM) is a cutting-edge technique that combines scanned probe technology with the capabilities of optical microscopy [21]. SNOM allows us to explore the nanoworld by providing high spatial resolution and revealing details like shape, size, chemical composition, molecular structure, and dynamic properties of nanostructures. While traditional optical microscopes excel in spectroscopic and temporal selectivity, their resolution is limited by diffraction to around half the wavelength, typically 0.2-0.5 micrometers for visible light. Today's scientific and technological advancements demand tools capable of characterizing, generating, and manipulating structures as small as a few nanometers, as seen in biology, microelectronics, and medical sciences. Electron microscopes, scanning tunneling, and atomic force microscopes can achieve spatial resolutions of 10 nm and beyond but lack spectral and dynamic capabilities. Additionally, electron microscopes require vacuum operation, limiting their applications in life sciences and complicating sample handling. SNOM, on the other hand, offers excellent spectroscopic and temporal selectivity and boasts lateral resolution reaching well into the sub-100 nm range. While technical challenges once hindered its widespread use, recent research and development in near-field optics have overcome these obstacles. SNOM is now a well-understood and powerful tool for surface analysis, ready to be applied to various physics, chemistry, and biology-related challenges.

3.1. Theory and Operation of SNOM

Theory: The spatial resolution of conventional optical microscopy is restricted by diffraction. To fully leverage optical microscopy in nanotechnology, it becomes essential to surpass the diffraction limit and enhance spatial resolution. Achieving this requires the use of a subwavelength aperture. The key to attaining high spatial resolution beyond the diffraction limit is through near-field illumination using a subwavelength aperture.

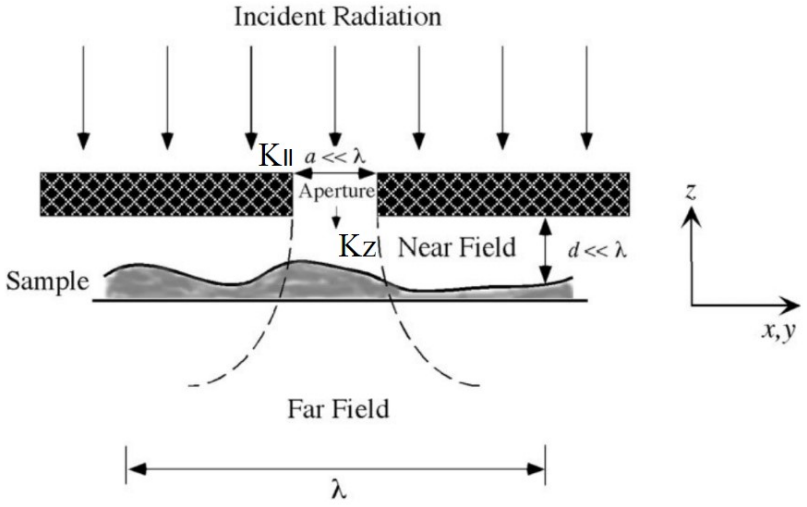

Figure 8: An illustration depicting the fundamental concepts of achieving sub-wavelength resolution in near-field optics. It relies on two essential conditions: (1) employing a light source with sub-wavelength properties (represented by the aperture in the diagram), and (2) positioning the sample within the close vicinity of the light source, known as the near-field zone. These conditions are crucial for achieving high-resolution imaging and probing capabilities in the near-field optical setup.

To maximize the performance of aperture SNOM, it is crucial to study the electric field distribution behind a small aperture. The sample is illuminated by a plane wave (Fig.8) can be represented as

$$E = E_0 \exp(i(\mathbf{k} \cdot \mathbf{r} - \omega t)), \text{where, } k^2 = k_{\|}^2 + k_z^2$$

with a wave vector $k = \frac{2\pi}{\lambda}$, where λ represents the wavelength, $k_{\|}$ and k_z represent the wave vectors transverse and longitudinal to the surface, respectively. Immediately after passing through this aperture, the transmitted field will remain relatively confined within its width. For an aperture of width 'a', The transverse component of the wave vector $k_{\|}$ is given by $k_{\|} = \frac{2\pi}{a}$. Consequently, the longitudinal component can be expressed as

$$k_z = \sqrt{\left(\frac{2\pi}{\lambda}\right)^2 - \left(\frac{k_{\|}}{a}\right)^2}$$

Depending on the magnitude of $k_{\|}$, two different solutions for $k_{\perp}$ can be obtained,

$$k_z = \begin{cases} \sqrt{k^2 - k_{\|}^2}, & \text{if } k_{\|} \leq k \\ i\sqrt{k_{\|}^2 - k^2}, & \text{if } k_{\|} > k \end{cases} \tag{4}$$

It is obvious that for $a < \lambda$, k_z becomes imaginary (case 1 of Equation 4). As a result, an electric field containing an imaginary wave vector along the propagation

direction is indicative of an evanescent field. Consequently, it remains tightly confined to the aperture and does not spread into the distant field. The significant confinement is accountable for the remarkable resolution attainable in scanning near-field optical microscopy.

For a much larger aperture size ($a > \lambda$), the transmitted field closely resembles that of the incident field (case 2 of Equation 4). The transmitted field primarily propagates in the forward direction, with a propagation vector $k_z \approx$ k. With a larger aperture, the spectrum of the transmitted field in the propagation direction will be dominated by propagating components. The presence of evanescent components, which are responsible for near-field effects, becomes minimal. The transmitted light through the aperture will experience diffraction, leading to the spreading of the beam and reduced spatial resolution. This phenomenon limits the ability to achieve high-resolution imaging using conventional optical systems. The transmitted field will be weakly localized at the vicinity of the aperture and will not exhibit strong confinement. Consequently, the enhancement of near-field effects is limited.

Operation: The setup of an SNOM system resembles that of other scanning probe microscopes. It involves a tip, which is a subwavelength light source or detector, and a scanning system that precisely moves the tip relative to the sample with sub-nanometer accuracy. A feedback mechanism (dither piezo) ensures a constant and near-field tip-sample separation. Data acquisition and scanning are controlled and synchronized by a computer (Fig.9). To complete the SNOM system, an external laser and a sensitive optical detection system (photomultiplier tube (PMT)) are incorporated, tailored to specific applications. Typically, the SNOM head is integrated into a conventional far-field optical microscope, enabling precise positioning of the SNOM tip on the desired part of the sample. As a result, SNOM functions as the highest magnification of the entire optical microscope setup.

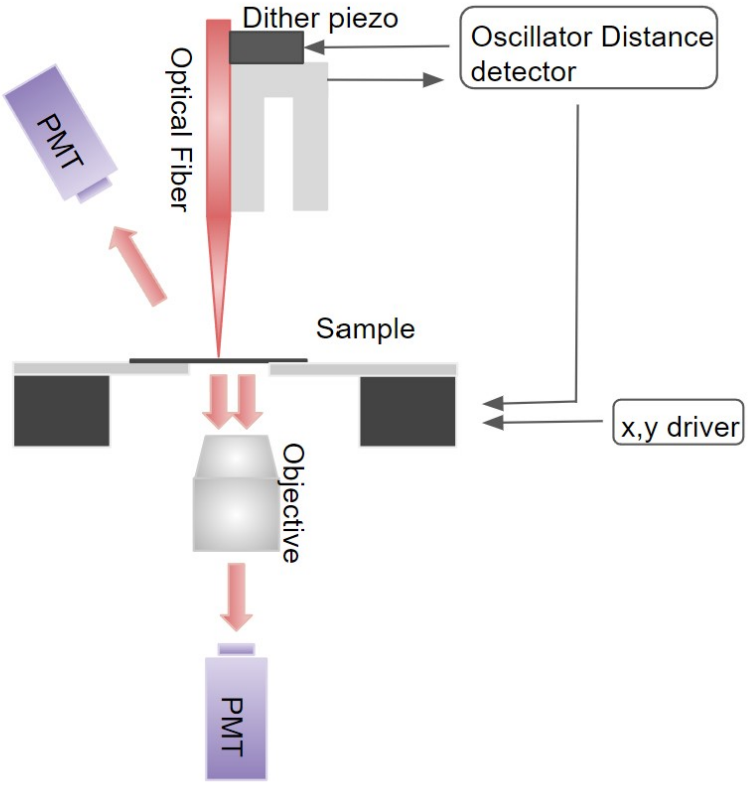

Figure 9: An illustration representing the Scanning Near-Field Optical Microscopy set up. The system incorporates an external laser and optical detection (PMT) customized for applications. It is integrated into a conventional optical microscope, the SNOM tip's precise positioning makes it the highest-magnification element.

4. Applications and Advances

Organic semiconductors: The photoconductivity of rubrene crystals [22], focusing on exciton and charge carrier behavior. At low excitation, both bulk and surface photoconductivity showed linear responses ($\alpha = 1$). At higher intensities, bulk photoconductivity followed bimolecular recombination ($\alpha = 1/2$). Pristine rubrene exhibited a unique $\alpha = 1/3$ behavior at the surface due to dominant triplet-charge quenching. At even higher intensities, surface and bulk photoconductivity exhibited $\alpha = 1/4$ and 0.4, respectively, attributed to triplet-triplet fusion competition. The findings offer insights into nonlinear photoconductivity in highly-ordered organic semiconductors, crucial for optoelectronic applications.

The electronic structure of bulk heterojunction (BHJ) solar cells using photoconductivity spectral response and carrier mobility measurements [23], along with theoretical calculations was invextigated. Evidence suggests the presence of band

tail states with an approximately exponential DOS, supported by both experiments and theory. However, the specific band tail being measured remains uncertain. The measurements indicate that the interface band gap, which separates the polymer HOMO and the PCBM LUMO, occurs at an absorption coefficient of approximately $10\,\mathrm{cm}^{-1}$ in the spectral response data, potentially providing valuable information for other BHJ solar cells. A DOS model is developed, but certain aspects of it are still undetermined. The photoconductivity spectral response can be explained by a model involving weak phonon coupling with disorder-induced band tail states, contrasting with a strong phonon coupling model. Distinguishing between the two models is challenging, and both band tail states and phonon coupling may play significant roles. Transient photoconductivity measures the combination of electron and hole transport, but distinguishing between them is currently not possible. An analytical procedure is devised to extract the dispersion parameter and mobility from experimental data. The slower carrier shows dispersion with a room-temperature mobility of approximately $10^{-4}\,\mathrm{cm}^2/\mathrm{V\,s}$, exhibiting thermal activation and a temperature-dependent dispersion parameter consistent with multiple trapping in an exponential band tail.

A group of researchers investigated the effect of strong coupling on polaron photoconductivity in an organic semiconductor called TAPC doped with MoO_3 [24]. Strong coupling occurs when molecular electronic or vibrational transitions hybridize with light to form polariton states, which can have different properties than the uncoupled molecules. To conduct their study, the researchers used measurements of the photoconductivity spectral response and carrier mobility, along with theoretical calculations. They coupled the charged molecules (polarons) to a Fabry-Perot microcavity to achieve strong coupling. They then measured the photoconductivity spectra and observed polaron polariton modes. It showed that the field dependence of the photoconductivity changed with strong coupling. This indicated a modification in the initial photoinduced electron transfer event responsible for dissociating coulombically bound holes from their MoO_3 counterions. The researchers proposed that strong coupling increased the thermalization length, affecting the dissociation yield and charge transfer rate. However, the exact mechanism behind the polariton-enhanced charge transfer still requires further investigation. The findings highlight the potential of strongly coupled exciton and polaron systems for studying cavity-controlled electron transfer.

A comprehensive comparison of infrared spectroscopy techniques was conducted on organic semiconductor single crystals [25]. The three methods used were FT-IR microscopy, AFM-IR, and IR-SNOM. Interestingly, distinct IR spectra were obtained for each technique, with certain molecular modes being either enhanced or suppressed depending on the crystal's molecular orientation and the chosen method. Notably, AFM-IR spectra quality varied significantly based on the molecular structures, likely influenced by distinct thermal expansion coefficients along different crystal axes. In the case of IR-SNOM, the orientation and polarizability of

the π-conjugated core of molecules played a significant role in the signal strength and enhancement of specific out-of-plane modes. Both AFM-IR and IR-SNOM exhibited the ability to discern local structures in polycrystalline samples of the organic semiconductor PDIF-CN_2 with excellent spatial resolution. However, interpreting the contrast observed in the spectra remains a formidable challenge. To gain further insights, future studies should explore additional model systems and conduct comparative investigations to ascertain the strengths and limitations of these advanced IR spectroscopy and microscopy techniques. Establishing guidelines for their application in molecular semiconducting thin films beyond basic morphology would be of great value.

Infrared scattering-type scanning near-field optical microscopy (IR s-SNOM) to investigate molecular crystallites of diindenoperylene (DIP) on a nanoscale level [26]. The researchers observed two distinct groups of DIP molecular orientations on a MoS_2 substrate, influenced by defects in the substrate. By analyzing the ratio of scattered optical amplitudes, they accurately determined the molecular orientation without the need for a reference comparison. The study also involved density functional theory (DFT) calculations to understand the coupling effects between orthogonal vibrational modes near the absorption peak at $1450\,cm^{-1}$. This allowed them to explain the reduced ratio of optical amplitudes observed in the experiments. Overall, the novel approach demonstrated the potential of IR s-SNOM in studying molecular orientations and defects in organic films, with potential implications for developing organic optoelectronic devices.

Scanning near-field optical microscopy (SNOM) along with pump-probe spectroscopy to investigate the behavior of excitons (excited states of molecules) in thin films of a material called perylenetetracarboxylic dianhydride (PTCDA)[27]. They illuminated the film with a pump laser at 520 nm to excite the excitons and then probed the material with a second laser at 650 nm to measure how the excitons behaved over time. The SNOM setup allowed them to obtain high-resolution images of the exciton population, providing detailed information about their dynamics. They found that the behavior of excitons was influenced by their density and observed a phenomenon called exciton-exciton annihilation at high exciton densities. The study demonstrated that pump-probe SNOM can provide more accurate information about exciton dynamics compared to conventional SNOM techniques. Additionally, they found that using high repetition rate laser systems could speed up imaging and enable pump-probe measurements with very low pulse energies.

2D Materials: The photoconductivity of the MoS_2 films [28] was investigated by exposing the films to light using a solar simulator and measured the resulting photocurrent. Surprisingly, the photoconductivity behavior did not follow a linear relationship with light intensity, which is typically observed for semiconductors. Instead, it scaled roughly with the square root of the incident light intensity. This behavior is usually associated with bimolecular recombination, indicating the presence of trap-free systems. However, further analysis revealed that the slow rise and

decay of the photocurrent indicated the presence of traps. Traps are localized states in the material that can capture and release charge carriers (electrons and holes) under light exposure. These traps can slow down the photocurrent response and lead to non-linear behavior. The researchers proposed that the traps might be associated with the edges of the MoS_2 flakes in the film. Despite the presence of traps, the devices showed reasonable photoresponsivity, matching the early reports for monolayer graphene photodetectors. The spectral response of the devices indicated an apparent peak around 650 nm, which is consistent with the expected behavior for MoS_2 excitons. The devices exhibit photoconductivity, but the presence of traps introduces complexity in the photocurrent behavior. Further research could explore passivation methods to reduce the effects of traps and improve device performance.

TOF photoconductivity measurements to study the electron transport properties was investigated on $Ti_3C_2T_x$ MXene thin films [29]. The results showed that the electron mobility in these MXene flakes reached values as high as $279\,cm^2/Vs$. This mobility is substantially higher than the previously reported field-effect mobility, which was below $10\,cm^2/Vs$. The researchers attribute this difference in mobility to the precise exfoliation process of MXene and the efficient deposition method used to create the layers. The exfoliation yielded flakes with relatively large dimensions, up to several microns in size. The layers formed a film consisting of up to 6-layer-thick interconnected flakes with random orientations. The charge transport through this network of randomly connected flakes is characterized as a combination of charge transport through crystalline flakes and trapping in localized states at the interfaces between flakes. The former process results in high charge mobility, while the latter leads to low charge carrier mobility. The study suggests that the observed high charge carrier mobility in these layers is a result of the transport through several pristine MXene layers away from the dielectric interface. This reduces the impact of charge trapping at the interface and results in an overall higher observed mobility. However, the charge carrier mobility still exhibits a positive dependence on the electric field of the Poole-Frenkel type, typical for disordered materials. This behavior is associated with the multilayered network of randomly distributed flakes with an interfacial electronic structure, which improves charge carrier transport bypassing the trapping effect.

Near-field photocurrent nanoscopy to study bare and encapsulated graphene [30]. In bare graphene, they observed strong photocurrent signals at grain boundaries, indicating modified electronic properties. Random photocurrent variations suggested charge puddles with varying carrier densities. In encapsulated graphene, strong carrier density variations near edges were noticed, possibly due to water molecule penetration. To address edge doping, local conductive gates were used, effectively suppressing edge and photodoping effects. The technique provided valuable insights into graphene's local electronic properties, enhancing our understanding of its behavior and potential applications in electronic devices.

A new tunable laser source called OPO/OPA laser to perform near-field pho-

tocurrent nanoscopy (s-SNOM) on few-layer graphene (FLG) [31]. They achieved nanoscale resolution and directly measured the complex optical conductivity resonance in bilayer graphene (BLG) at around 0.39 eV. This technique allowed them to map the electronic and optical properties of graphene with high spatial resolution. They suggest that this approach can be extended to investigate the IR-conductivity properties and specific resonances in various stacking orders, including twisted graphene and Moiré patterns. By combining s-SNOM with low-temperature measurements, they could even investigate superconductivity phenomena in magic-angle graphene at infrared frequencies.

5. Challenges and Future outlook

Challenges in photoconductivity measurements using scanning near-field optical microscopy (s-SNOM) in organic semiconductors and 2D materials arise from several factors [21]. One of the primary challenges is achieving high spatial resolution. The near-field region is constrained by the tip size, limiting the ability to probe small-scale features or nanoscale devices with precision. Additionally, the signal-to-noise ratio in s-SNOM measurements can be a limitation, especially when dealing with weak photocurrent signals in organic semiconductors or 2D materials. Improving the sensitivity of the detection system is crucial to accurately measure low photocurrent levels and obtain meaningful data. Efficiently coupling light to the sample and collecting scattered light for detection is another hurdle in s-SNOM measurements. In organic semiconductors or 2D materials, achieving efficient optical coupling can be challenging due to their unique optical properties. Furthermore, accurate calibration and quantification of the measured photoconductivity values are essential for meaningful results. This requires careful consideration of various parameters, including the tip-sample distance, tip properties, and background subtraction.

In the future, advancements in instrumentation will enhance the capabilities of SNOM for photoconductivity measurements. This may involve the development of more sensitive detectors and tunable laser sources to explore a broader range of wavelengths and improve signal detection. Combining SNOM with other imaging techniques, such as atomic force microscopy (AFM) or Raman spectroscopy, can provide complementary information and a more comprehensive understanding of the electronic and structural properties of organic semiconductors and 2D materials. Introducing time-resolved techniques in SNOM can reveal dynamic photoconductivity processes, shedding light on charge carrier lifetimes, recombination dynamics, and photoresponse mechanisms in these materials. Advancements in theoretical modeling and simulations will aid in accurately interpreting SNOM data and gaining a deeper understanding of the photoconductivity behavior in organic semiconductors and 2D materials. Integrating SNOM with device fabrication and electrical measurements can provide a more comprehensive understanding of the photoconductivity behavior in real devices, facilitating the optimization of

device performance. Addressing the challenges and exploring future directions in SNOM photoconductivity measurements will help to gain valuable insights into the electronic properties of organic semiconductors and 2D materials. These advancements are vital for the development of next-generation electronic and optoelectronic devices.

6. Conclusion

Scanning near-field optical microscopy (SNOM) has proven to be a valuable technique for studying photoconductivity in organic semiconductors and 2D materials. Its nanoscale spatial resolution and non-contact nature provide unique insights into the electronic properties of these materials at the sub-wavelength level. Through SNOM, it has been able to directly map and characterize photoconductivity phenomena, including charge carrier transport, trapping, and recombination processes. This has contributed to a better understanding of the fundamental behavior of organic semiconductors and 2D materials, with potential implications for the development of advanced electronic and optoelectronic devices.

The research has independently explored the photoconductivity of organic semiconductors and 2D materials using scanning near-field optical microscopy (SNOM). However, there remains a significant opportunity to investigate the photoconductivity of their heterostructures, combining these materials in novel ways. This approach has the potential to yield valuable and exciting results, leading to a deeper understanding of the complex behavior of these hybrid systems and paving the way for the development of advanced and tailored optoelectronic devices.

References

[1] Hugo Bronstein, Christian B. Nielsen, Bob C. Schroeder and Iain McCulloch, *The role of chemical design in the performance of organic semiconductors, 4th Edition*, Nat Rev Chem, 2020.

[2] Rubén Mas-Ballesté, Cristina Gómez-Navarro, Julio Gómez-Herrero and Félix Zamora, *2D materials: to graphene and beyond, 1st Edition*, Nanoscale 3, 2011.

[3] Richard J. Hermann and Michael J. Gordon, *Nanoscale Optical Microscopy and Spectroscopy Using Near-Field Probes, 9th Edition*, Annual Review of Chemical and Biomolecular Engineering, 2018.

[4] Safa. O. Kasap, *Photoconductivity: Fundamental Concepts, Photoconductivity and Photoconductive Materials: Fundamentals, Techniques and Applications 1*, Wiley & Sons, 2022.

[5] M. Vaněček, J. Kočka, J. Stuchlík, A. Tříska, *Direct measurement of the gap states and band tail absorption by constant photocurrent method in amorphous silicon, 11th Edition*, Solid State Communications, 1981.

[6] M. Vaněček, J. Kočka, A. Poruba and A. Fejfar, *Direct measurement of the deep defect density in thin amorphous silicon films with the "absolute" constant photocurrent method, 10th Edition*, Journal of Applied Physics, 1995.

[7] Hidetoshi Oheda, *Phase - shift analysis of modulated photocurrent: Its application to the determination of the energetic distribution of gap states, 11th Edition*, Journal of Applied Physics, 1981.

[8] R. Bruggemannt, C. Main, J. Berkin and S. Reynolds, *An evaluation of phase-shift analysis of modulated photocurrents, 1st Edition*, Philsophical Magazine B, 1990.

[9] C. Longeaud, D. Roy, and O. Saadane, *Role of interstitial hydrogen and voids in light-induced metastable defect formation in hydrogenated amorphous silicon: A model, 8th Edition*, Physical Review B, 2002.

[10] M. S. Iovu and I. A. Vasiliev and E. P. Colomeico and E. V. Emelianova and V. I. Arkhipov and G. J. Adriaenssens, *Photocurrent Relaxation in Pure and Pr-doped a-As_2S_3 Films, 16th Edition*, Journal of Physics: Condensed Matter, 2004.

[11] C. Main and R. Brüggemann and D. P. Webb and S. Reynolds *Determination of Gap-State Distributions in Amorphous Semiconductors from Transient Photocurrents Using a Fourier Transform Technique, 83th Edition*, Solid State Communications, 1992

[12] C. Main *Interpretation of Photocurrent Transients in Amorphous Semiconductors, 299th Edition*, Journal of Non-Crystalline Solids, 2002.

[13] Veaceslav Coropceanu 1, Jérôme Cornil, Demetrio A da Silva Filho, Yoann Olivier, Robert Silbey, Jean-Luc Brédas Coropceanu, *Charge transport in organic semiconductors, 107th Edition*, Chemical Reviews, 2007.

[14] Masahiro Funahashi, *Time of Flight Method for Determining the Drift Mobility in Organic Semiconductors, Organic Semiconductors for Optoelectronics*, Springer, 2021.

[15] Monica Brinza, Evguenia V. Emelianova, and Guy J. Adriaenssens, *Nonexponential distributions of tail states in hydrogenated amorphous silicon, 71th Edition*, Physical Review B, 2005.

[16] M. Brinza, and Guy J. Adriaenssens, *Electronic properties of hydrogenated amorphous silicon prepared in expanding thermal plasmas, 7th Edition*, J. Optoelectron. Adv. Mater, 2005.

[17] Guy J. Adriaenssens, and Astrid Eliat, *Density of Localized States in the Gap of Non-Crystalline Semiconductors, 77th Edition*, Physics and Applications of Non-Crystalline Semiconductors in Optoelectronics, Springer Netherlands, 1997.

[18] S. O. Kasap, B. Polischuk and D. Dodds, *An interrupted field time - of - flight (IFTOF) technique in transient photoconductivity measurements, 61th Edition*, Review of scientific instruments, 1990.

[19] Bud Fogal, M. Zahangir Kabir, Stephen K. O'Leary, Robert E. Johanson and S. O. Kasap, *X-ray-induced recombination effects in a-Se-based x-ray photoconductors used in direct conversion x-ray sensors, 22nd Edition*, Journal of Vacuum Science & Technology A: Vacuum, Surfaces, and Films, 2004.

[20] C. Haugen and S. O Kasap, *Langevin recombination of drifting electrons and holes in stabilized a-Se (Cl-doped a-Se: 0.3% As), 71th Edition*, Philosophical Magazine B, 1995.

[21] Richter, Marc and Deckert, Volker, *Scanning near-field optical microscopy (SNOM)*, Wiley Online Library, 2011.

[22] P. Irkhin, H. Najafov, and V. Podzorov. *Steady-state photoconductivity and multiparticle interactions in high-mobility organic semiconductors, 5th Edition*, Scientific reports, 2015.

[23] R. A. Street, K. W. Song, J. E. Northrup, and S. Cowan. *Photoconductivity measurements of the electronic structure of organic solar cells, 83rd Edition*. Physical Review B, 2011.

[24] Nina Krainova, Alex J. Grede, Demetra Tsokkou, Natalie Banerji, and Noel C. Giebink. *Polaron photoconductivity in the weak and strong light-matter coupling regime, 124th Edition*, Physical Review Letters, 2020.

[25] Vaishnavi J. Rao, Maik Matthiesen, Katelyn P. Goetz, Christian Huck, Chanyoung Yim, Rita Siris, Jie Han, Sebastian Hahn, Uwe H. F. Bunz, Andreas Dreuw, Georg S. Duesberg, Annemarie Pucci, and Jana Zaumseil. *AFM-IR and IR-SNOM for the characterization of small molecule organic semiconductors, 9th Edition*. The Journal of Physical Chemistry C, 2020.

[26] Nada Mrkyvkova, Adrian Cernescu, Zdenek Futera, Alois Nebojsa, Adam Dubroka, Michaela Sojkova, Martin Hulman, Eva Majkova, Matej Jergel, Peter Siffalovic, and Frank Schreiber. *Nanoimaging of orientational defects in semiconducting organic films, 1st Edition*, The Journal of Physical Chemistry C, 2021.

[27] Karki Khadga, Mahesh Namboodiri, Tahir Zeb Khan, and Arnulf Materny. *Pump-probe scanning near field optical microscopy: Sub-wavelength resolution chemical imaging and ultrafast local dynamics*, Applied physics letters, 2021.

[28] Cunningham, Graeme, Umar Khan, Claudia Backes, Damien Hanlon, David McCloskey, John F. Donegan, and Jonathan N. Coleman. *Photoconductivity of solution-processed MoS_2 films, 14th Edition*, Journal of Materials Chemistry C, 2013.

[29] Jurij Urbančič, Erika Tomsič, Manisha Chhikara, Nadiia Pastukhova, Vadym Tkachuk, Alexander Dixon, Andraž Mavrič, Payam Hashemi, Davood Sabaghi, Ali Shaygan Nia, Gvido Bratina, and Egon Pavlica. *Time-of-flight photoconductivity investigation of high charge carrier mobility in $Ti_3C_2T_x$ MXenes thin-film, 1st Edition*, Diamond and Related Materials, 2023.

[30] Woessner, Achim, Pablo Alonso-González, Mark B. Lundeberg, Yuanda Gao, Jose E. Barrios-Vargas, Gabriele Navickaite, Qiong Ma, David Janner, Kenji Watanabe, Adam W. Cummings, and Takashi Taniguchi. *Near-field photocurrent nanoscopy on bare and encapsulated graphene, 1st Edition*, Nature Communications, 2016.

[31] Wirth, Konstantin G., Heiko Linnenbank, Tobias Steinle, Luca Banszerus, Eike Icking, Christoph Stampfer, Harald Giessen, and Thomas Taubner. *Tunable s-SNOM for nanoscale infrared optical measurement of electronic properties of bilayer graphene. 8th Edition*, ACS Photonics, 2021.

Review of the Dynamics and Emission Characteristics of Tidal Disruption Events: Theory, Observations, and Simulations

Mario Aguilar

University of Nova Gorica, Vipavska 13, SI-5000 Nova Gorica

Abstract

We present a review of some of the state-of-the-art studies in the theoretical modeling of processes with significant impact on the expected light curves of Tidal Disruption Events (TDE) in visible light, with emphasis in the influence of the parameters (e.g. star orbit parameters, effects of general relativity theory) in the characterization of TDE events, black hole masses and their environments. In this respect, observational correlations, TDE emission mechanisms, and hydrodynamical simulations are also covered to dive into the dynamics of TDEs. Challenges in understanding optical emissions and future directions toward more realistic simulations are discussed, in light of the forthcoming Legacy Survey of Space and Time (LSST) project at the Vera Rubin Observatory, which is expected to discover tens of thousands of TDEs in 10 years of operation.

Keywords: Black hole physics, Hydrodynamical simulations, Relativistic fluid dynamics, Tidal disruption

1. Introduction

In the late 1970s, the concept of Tidal Disruption Events (TDEs) emerged as a theoretical idea. They were regarded as a dynamic outcome of massive black holes (MBHs) postulated to exist at the cores of most galaxies [1, 2]. In this scenario, the trajectory of a star could lead it to a proximity where the MBH's gravitational forces either tear it apart or capture it. The outcome depends on how the tidal disruption radius compares to the

Email address: mario.aguilar@ung.si (Mario Aguilar)

black hole's event horizon size. When a star is torn apart beyond the event horizon, which typically occurs when the black hole mass is less than or around $10^8 M_\odot$, a luminous burst of radiation is anticipated. This radiation stems from the portion of tidal debris that remains bound and falls back onto the black hole, subsequently forming an accretion disc as it circularizes [3, 4, 5, 6]. At that time, this electromagnetic (EM) signal was proposed as an effective method to investigate quiescent MBHs residing in the centers of galaxies, especially when direct dynamical measurements of black hole mass are unattainable [7].

Additionally, TDEs serve as an astronomical laboratory for observing the real-time emergence of an accretion disc and jet. During a TDE, a MBH that was previously inactive undergoes a substantial alteration due to a sudden inflow of gas. This gas, potentially accompanied by magnetic flux, originates from a star that has been disrupted and becomes available for the process of accretion onto the MBH. Because the time frame for the remnants of the disrupted star to fall back towards the MBH and form a circular path is extremely short – often just a matter of months – TDEs offer a unique opportunity to observe the gradual formation of an emerging accretion disc. This also includes the initiation of any concurrent outflow or jet of matter. Once accretion sets in, it is doable to explore the density of gas in the central parts of galaxy cores by studying the effects of photoionization and the interplay between jets, outflows, and the environment surrounding the nucleus of the galaxy [7].

The rate at which stars are likely to undergo tidal disruption (TDE rate) is influenced by factors such as the mass, spin, binarity and occupation fraction of MBHs. This renders TDEs highly valuable for investigating the characteristics of MBH demographics [7]. The observed TDE rate is in the range of 10^{-5} to 10^{-4} galaxy^{-1} yr^{-1} [8, 9, 10, 11, 12, 13, 14, 15].

The importance to study MBHs or supermassive black holes (SMBHs) owes to the fact of their location in galactic centers, which has a significant impact on the dynamics and evolution of galaxies. One of the ways in which MBHs and SMBHs influence galaxies is through their interaction with the surrounding matter. As material falls toward the black hole, it forms an accretion disc and releases large amounts of energy in the form of EM radiation or winds. This can have a significant effect on the star formation and evolution of the host galaxy. Despite their widespread presence, the properties of most MBHs and SMBHs are not well known, due to the majority of them being in a quiescent state, and therefore challenging to study [7].

Currently there are around one hundred observed TDE candidates [16].

This counting is predicted to experience a substantial upswing, approximately one thousand additional sources each year [17], as new surveys begin, such as Legacy Survey of Space and Time (LSST), commencing in 2024 at the Vera Rubin Observatory [18].
The main goal of this paper is to present a brief review of some theoretical aspects for a quick start in the use of the latest available codes to execute TDE hydrodynamical simulations, with some modern inputs from observations. Some theoretical aspects not covered in this paper include, for example, the scattering conditions of the star into the loss cone, partial tidal disruptions, and nuclear reactions, which are not considered essential for a first approach to run these modern scripts. A more extensive theoretical focused review can be found, for example, in [19]. This paper is not intended as a review of observational aspects of TDEs, with a more extensive modern review published in [7].

The paper is structured as follows: Section 2 contains some theoretical foundations of TDEs needed to understand both the observations and hydrodynamical simulations, including the conditions that the astrophysical configuration must obey to undergo a disruption and a time-ordered description of the dynamics of the disruption. In Section 3 some basic ideas of the main observational EM emission measurements are given along with a narrative of how these emissions are speculated to be generated. The processes presented do not include secondary emissions such as IR emissions. In Section 4 a description of the two main approaches to perform TDE hydrodynamical simulations is presented, and an example of one of the most suitable codes for TDE hydrodynamical simulations is briefly introduced. Section 5, based in the latest efforts performed in numerical hydrodynamical simulations, presents avenues for further research. Finally, Section 6 concludes the paper.

2. Theory

2.1. Disruption Conditions

A MBH or SMBH situated at the center of a galaxy can be modeled as a gravitational sink, drawing in stars that come close enough to it. The elimination of a star can happen through two manners, contingent on the mass of the MBH and the characteristics of the star. Firstly, the star may be engulfed by the MBH if it gets too close and crosses the event horizon, disappearing from any external observer. Alternatively, the tidal forces exerted by the powerful gravitational pull of the MBH may disrupt the star,

tearing it apart. In cases where the star is a compact object like a neutron star or another black hole, it remains relatively unaffected by the tidal forces of the MBH and it is eventually swallowed as a whole. This fate can also befall ordinary stars, provided they possess the necessary conditions to withstand being torn apart by the intense tidal forces of the MBH [20].
In this situation, a star with a mass denoted as $M_\star$ and a radius represented by $R_\star$, is following a parabolic path at a distance r from the MBH, located in the focal point of the orbit with a mass M_{BH}. The tidal forces exerted by the MBH intensify as the star draws nearer. If the star comes within a distance where the tidal forces surpass the star's self-gravitational forces, it will be torn apart or disrupted [21]. Recalling the gravitational constant G, this condition can be mathematically expressed as,

$$\frac{GM_{\rm BH}R_\star}{r^3} > \frac{GM_\star}{R_\star^2}, \tag{1}$$

The maximum distance from the MBH at which a star can be ripped apart, the tidal radius R_t [1], is then

$$R_t \equiv R_\star \left(\frac{M_{\rm BH}}{M_\star}\right)^{1/3}, \tag{2}$$

Using the pericenter distance of the orbit R_p, it is customary to define the penetration factor,

$$\beta \equiv \frac{R_t}{R_p}, \tag{3}$$

Stars with a $\beta > 1$ undergo complete disruption. On the other hand, if a star has $\beta \leq 1$, it may only experience a grazing interaction with the tidal sphere, leading to a partial disruption. In such instances, the star's core remains intact, while the MBH only removes some of the star's outer layers [21].
A luminous burst resulting from a complete disruption of a star sets both a lower and upper limit on the MBH mass. The lower limit is determined by the size of the star and its pericenter distance [21]. Should the pericenter distance to the black hole be smaller than the star's radius, the star will fully engulf the black hole, making the flare unobservable. On the other hand, the upper limit on the MBH's mass is defined by the Schwarzschild radius. A flare occurs only if the star is disrupted outside the event horizon of the black hole. In the straightforward scenario of a non-rotating MBH, the Schwarzschild radius, R_s, exhibits a linear growth with its mass,

$$R_s = \frac{2GM_{\rm BH}}{c^2}, \tag{4}$$

where c is the speed of light. Combining this with Eq. 2, the upper limit on the mass of the black hole, capable of causing the disruption of a specific type of star outside the event horizon, is obtained [20],

$$M_{\text{crit}} = 1.1 \cdot 10^8 M_\odot \left(\frac{R_\star}{R_\odot}\right)^{3/2} \left(\frac{M_\star}{M_\odot}\right)^{-1/2}, \tag{5}$$

The radius of the Sun is denoted as $R_\odot$, and the mass of the Sun is represented by $M_\odot$. According to Eq. 5, if the mass of a black hole, denoted as M_{BH}, is less than or equal to $10^8 M_\odot$, a main sequence star will be disrupted outside the event horizon of the black hole. However, evolved stars can be disrupted by black holes with higher masses. When it comes to white dwarfs, they will only be disrupted outside the event horizon if the mass of the black hole is less than or equal to $10^5 M_\odot$, which corresponds to intermediate mass black holes (IMBHs) [21].
In Fig. 1, there is the $M_{\text{BH}} - \beta$ parameter space for tidal disruption events (TDEs). For a star to be disrupted outside the Schwarzschild radius R_S, it must fall within its respective triangle on the plot. The left side of the triangle is defined by the condition that the radius of the star $R_\star$ is less than the pericenter distance R_P; otherwise, the black hole penetrates inside the star.

The calculation of the tidal radius R_t is based on the assumption that the MBH gravitational field behaves like that of a Newtonian point particle, which is accurate only at significant distances, where R_t is much larger than the Schwarzschild radius R_s. However, when considering a Kerr black hole in the framework of general relativity, the tidal radius and, consequently, the critical mass of the MBH can vary due to the spin of the MBH. In this relativistic treatment, the MBH's rotation (spin) introduces additional complexities that can influence the dynamics of the tidal disruption event [22, 23].

2.2. Dynamics of TDEs

For the purpose of this section, a star of mass $M_\star$ and radius $R_\star$ on a parabolic orbit about the MBH of mass M_{BH} with the pericenter distance $R_P = R_T$ (so that the impact parameter is $\beta = 1$) will be analyzed. Initially, it is assumed that the star remains undisturbed until it reaches the pericenter of its orbit, as described by [3]. At this point, the star undergoes disruption. Then, different fluid elements within the star are located at various distances from the MBH. Consequently, there is a significant variation in the specific orbital energy ε within the star.

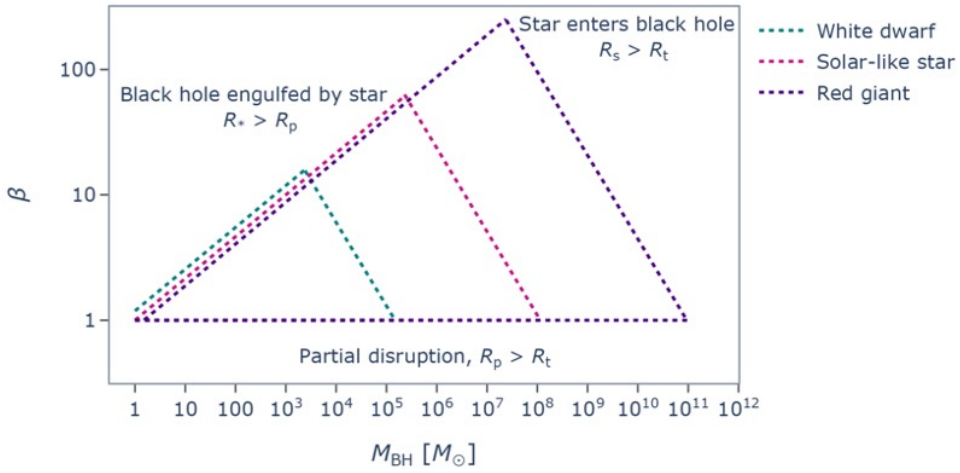

Figure 1: The diagram illustrates the $M_{\rm BH} - \beta$ parameter space for TDEs. It displays the allowed regions where stars of different types can be disrupted: white dwarfs (shown in green), Solar-type stars (shown in pink), and red giants (shown in purple). A star falling within its corresponding triangle indicates that it will undergo complete disruption. Beneath the triangles, where the value of β is less than 1, the disruptions are only partial or the interaction between the star and the black hole is weak. When β is much smaller than 1, there is virtually no interaction between the star and the black hole. In the upper-left corner of the parameter space, where $R_\star > R_P$, the black hole penetrates inside the star, and a TDE cannot occur in this scenario. In the upper-right corner of the diagram, where $R_S > R_P$, the star enters the black hole before undergo disruption. Figure from [21].

Under the assumption that the energy needed to disrupt the star is equivalent to its self-binding energy, the average specific binding energy of the debris to the black hole is similar to the star's specific self-binding energy. The debris farther from the black hole possesses a positive specific energy, whereas the portions closer to the black hole exhibit negative specific energy. The spread in the specific orbital energy of the debris is given by [3, 24, 25]

$$\Delta\varepsilon = \pm\frac{GM_{\rm BH}R_\star}{R_t^2}, \tag{6}$$

Therefore, around 50% of the stellar remnants possessing a particular orbital energy ($\varepsilon \leq 0$) stay gravitationally bound to the black hole, whereas the remaining portion with higher energy ($\varepsilon > 0$) becomes unbound. The proportion of bound and unbound debris may differ if the original stellar orbit is not precisely parabolic. The illustration of the disruption process can be found in Fig. 2.

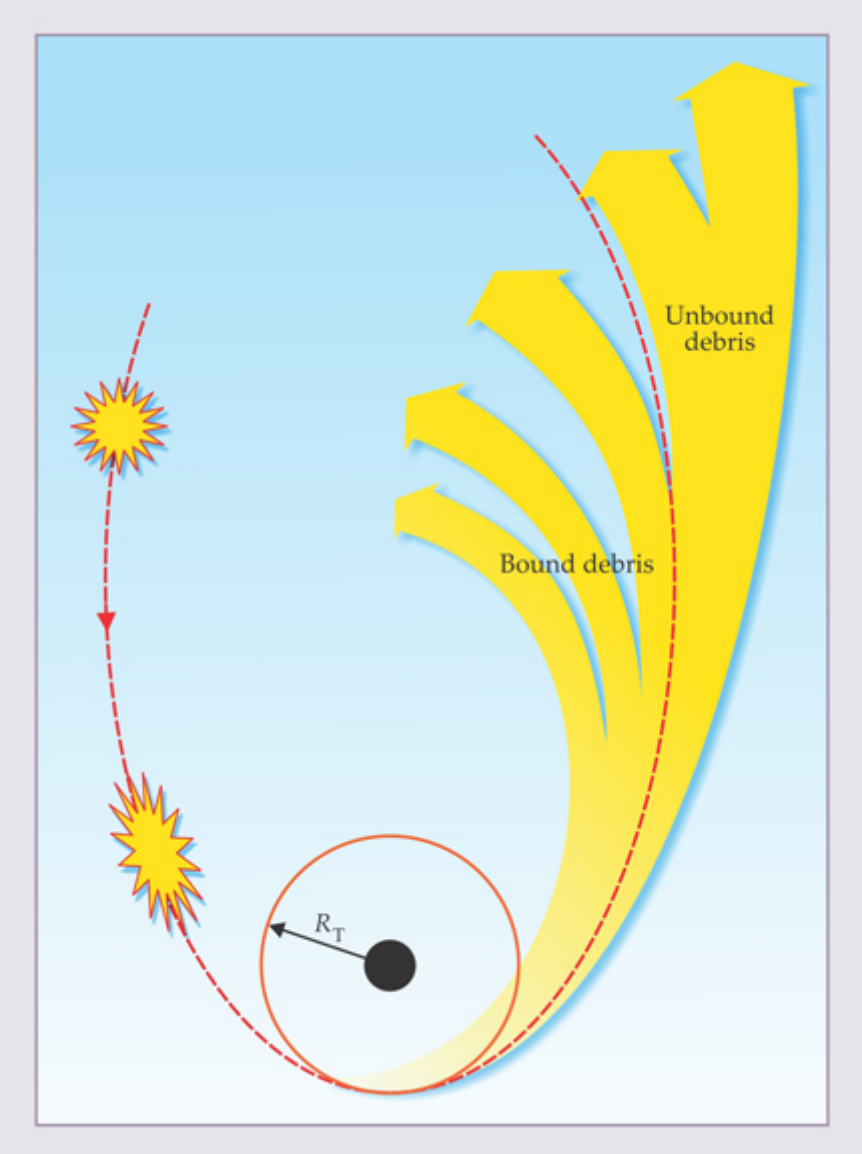

Figure 2: Beginning of the tidal disruption process of a star. As the star gets closer to a MBH represented by a black circle and enters the region spanned by the tidal disruption radius R_t, the MBH's tidal forces lead to the star's disruption. About half of the resulting stellar debris becomes gravitationally bound to the MBH and eventually coalesces into an accretion disc. Meanwhile, the other half of the stellar debris is not bound by the MBH's gravity and escapes into space. Figure from [26].

2.2.1. Phase 1: Dynamics of encounter at pericenter

The passage of the star at pericentre can then be analyzed in more detail. In its initial state of hydrostatic equilibrium, the star remains practically unaltered until it comes within a distance of a few times the tidal radius R_t from the MBH. At this point, as depicted in Fig. 3, the MBH's tidal force begins to deform the star. The deformation primarily occurs along a nearly radial direction because the stellar components closer to the MBH feel a stronger gravitational attraction. As the star approaches the tidal radius, this deformation becomes significant. The pressure response to this distortion leads to a spread in the orbital energy of the stellar debris, as described by Eq. 6 [27, 20].

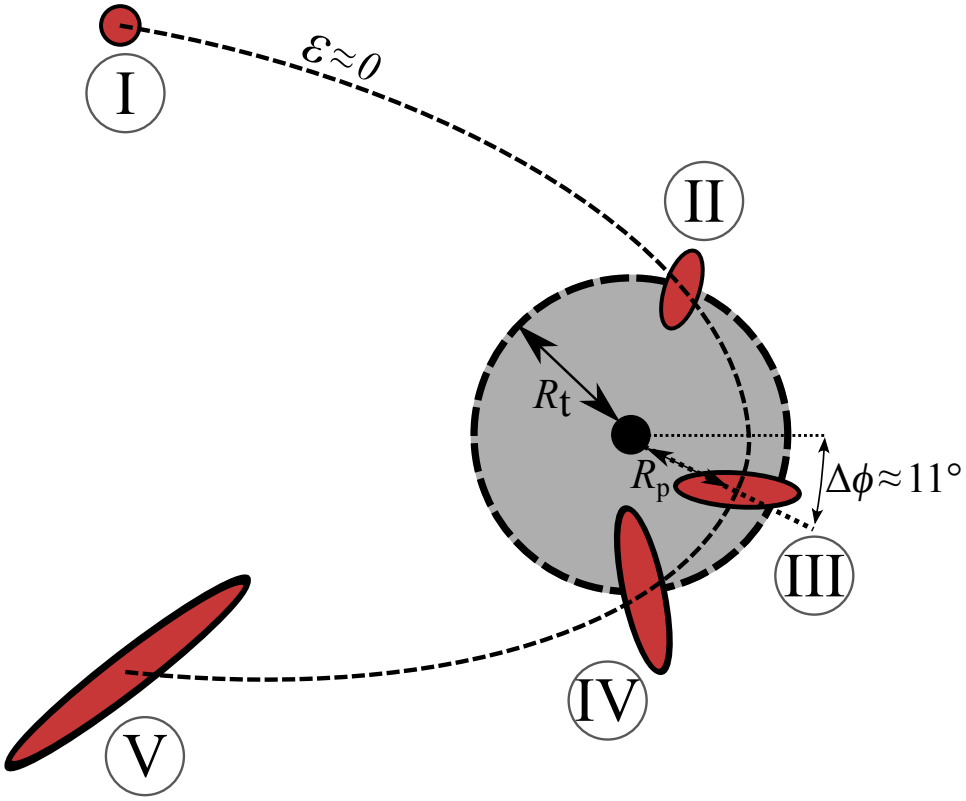

Figure 3: Sketch showing the passage of the star (in red) at pericentre inside the tidal sphere of radius R_t (grey area) with an orbit approximated as a parabola with orbital energy $\varepsilon \approx 0$. The time evolution of the orbit is indexed by roman numbers. Due to relativistic precession, in this example the star precess by an angle $\Delta\phi \approx 11^\circ$ after pericentre passage at distance $r = R_p$ from the MBH. Figure credit: Taj Jankovič.

2.2.2. Phase 2: Debris evolution and fallback

Following the disruption, the stellar remnants form an elongated configuration (Fig. 4). In this section, a concise description of the evolution of the debris stream around the MBH is provided [20]. As the star reaches pericenter and experiences tidal disruption, the gas within the debris stream moves along nearly ballistic trajectories. Specifically, the debris that is most strongly bound possesses an orbital energy, denoted as $\varepsilon_{\rm orb} = -\Delta\varepsilon$, which is associated with orbits having certain semi-major axes and periods,

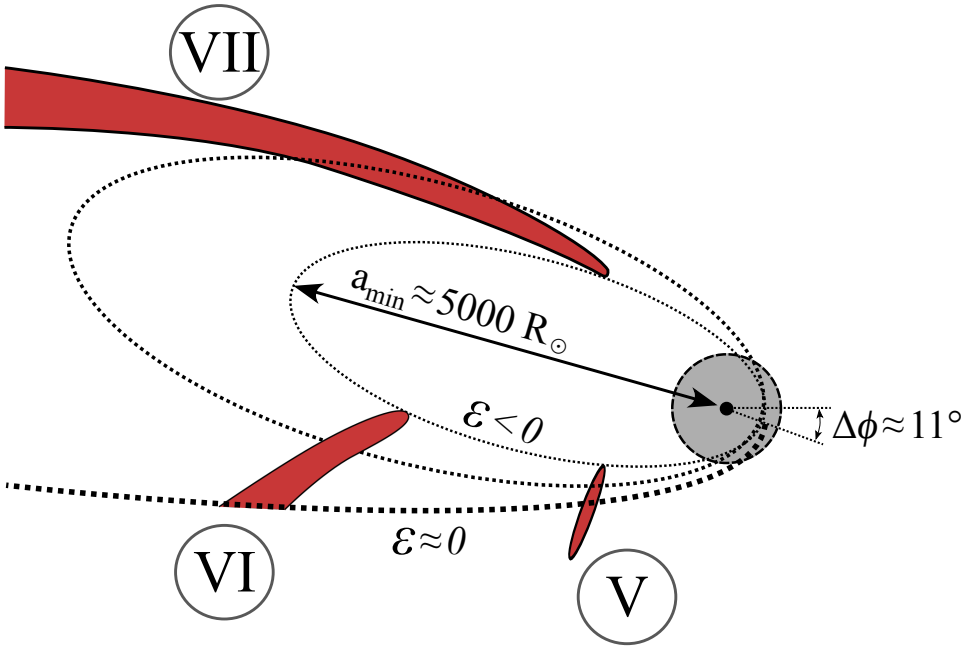

Figure 4: Diagram showing the second passage of the stellar remnants (in red) at pericentre inside the tidal sphere (grey area). A parabolic orbit with orbital energy $\varepsilon \approx 0$ is shown as the external and open dotted line. The dotted lines corresponding to inner and closed orbits corresponds to the bound debris with orbital energies $\varepsilon < 0$, including the innermost orbit linked to the most bound debris, with semi-major axis $a_{\rm min} \approx 5000\ R_\odot$. The time evolution of the orbit is indexed by roman numbers, labels that are the continuation of the ones in Fig. 3. Owing to the relativistic precession, in this example the stellar debris precess by an angle $\Delta\phi \approx 11^\circ$ after pericentre passage. Figure credit: Taj Jankovič.

$$a_{\min} = \frac{R_\star}{2}\left(\frac{M_{\rm BH}}{M_\star}\right)^{2/3} \tag{7}$$

$$t_{\min} = \frac{\pi}{\sqrt{2}}\sqrt{\frac{R_\star^3}{GM_\star}}\sqrt{\frac{M_{\rm BH}}{M_\star}} \tag{8}$$

The fallback mass rate dm/dt, that is the rate at which the bound matter falls back to the MBH, is obtained as,

$$\frac{dm}{dt} = \frac{dm}{d\varepsilon}\frac{d\varepsilon}{dt} = \frac{1}{3}(2\pi G M_{\rm BH})^{2/3}\frac{dm}{d\varepsilon}t^{-5/3}, \tag{9}$$

The rate of change of orbital energy over time, $d\varepsilon/dt$, is determined by applying Kepler's third law to obtain the energy of the most tightly bound debris elements after a time period t

$$\varepsilon = -\frac{1}{2}\left(\frac{2\pi G M_{\rm BH}}{t}\right)^{2/3} \tag{10}$$

Regarding the mass fallback rate dependence on $dm/d\varepsilon$, as a first approximation, it has been considered a uniform energy distribution [3, 24], which leads to the extensively known $t^{-5/3}$ power law decay. Under the assumption that around 50% of the stellar mass makes its way to the MBH anytime longer than $t_{\min}$, a maximum value $\dot{M}_{\rm pk}$ can be defined [28]

$$\frac{dm}{dt} = \dot{M}_{\rm pk}\left(\frac{t}{t_{\min}}\right)^{-5/3} \tag{11}$$

The assumptions of this theory have been reexamined so far [29] and it has been pointed out that the fallback mass rate is influenced by the internal structure of the star. Consequently, for a more accurate determination of the fallback mass rate, the assumption of a uniform energy distribution $dm/d\varepsilon$ should not be made. Although the standard $t^{-5/3}$ power law remains applicable, it holds true only in the later stages. Thus, in most of the literature, it is commonly posited that the accretion rate onto the MBH closely follows the mass fallback rate described by Eq. 9. Similarly, the resulting luminosity of the flare is also believed to be directly related to the fallback rate as $L \propto \dot{M} \propto t^{-5/3}$.

2.2.3. Phase 3: Self-crossing of streams

The general understanding is that the majority of the EM emission observed from TDEs is sourced from the dissipation of orbital energy in the

debris stream as it returns to the black hole [27]. The initial assumption in this context is that a circular accretion disc rapidly forms around the black hole. However, it is not entirely clear how such a disc structure forms from the debris stream initially. The formation of the disc requires an efficient dissipation mechanism since rapid circularization demands a significant amount of energy dissipation in a short period. Two primary dissipation mechanisms have been proposed for this purpose. The first one involves the intense compression of the stream at pericentre. However, this mechanism alone cannot achieve complete circularization [30].
The second mechanism of dissipation, as depicted in Fig. 5, involves an interaction where the stream intersects with itself. When the innermost part of the stream reaches pericentre, the debris undergo changes in their apsidal angles due to relativistic apsidal precession or hydrodynamical effects. This phenomenon can cause the stream to cross over itself: as the leading segments move away from the black hole after passing pericentre, they collide with the portion that is still falling back, resulting in shocks [5, 31]. These shocks can dissipate a portion of the orbital energy of the stream into heat, as demonstrated by estimates based on inelastic collisions [32, 33].
In fact, various studies have confirmed that self-crossing is generally the most effective mechanism for dissipating energy in this context [34, 35, 30, 36].

2.2.4. Phase 4: Accretion disc formation

As a consequence of the processes that facilitate the circularization of the debris stream, an accretion disc is formed. The circularization process encompasses various mechanisms responsible for dissipating kinetic energy within the debris stream, transforming its trajectories from elliptical to circular, and ultimately giving rise to the disc. However, the complete understanding of this circularization process remains elusive, and it involves several different mechanisms, as mentioned in Section 2.2.3. Once the accretion disc takes shape, as shown in Fig. 6, its structure and evolution will be determined by the efficiency and balance between the timescales of the circularization itself, radiative cooling, viscous accretion and debris infall [5].
While accurately describing the processes involved in the circularization of the stellar debris may pose challenges, it is reasonable to presume that, eventually, a circularized accretion flow will form around the MBH after disruption [20]. This particular phase of a tidal disruption event (TDE) has direct relevance to observations, as it will be described in Section 3.

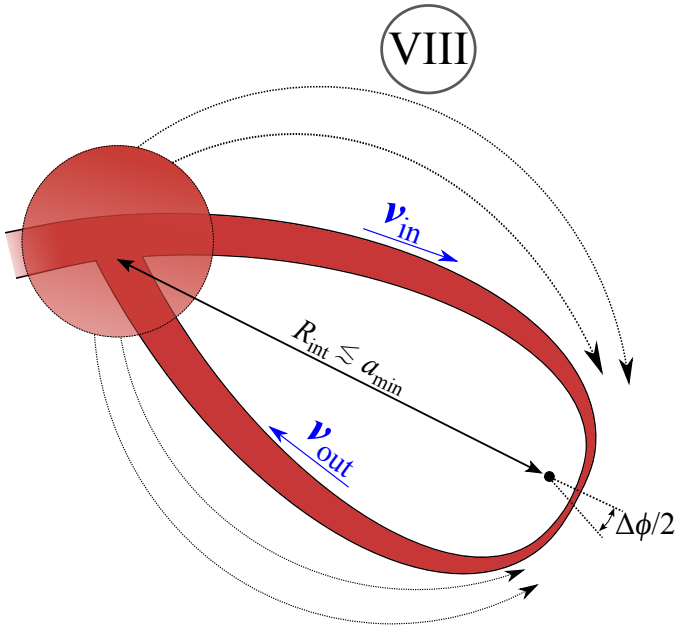

Figure 5: Diagram illustrating the self-crossing of the stream (in red). Owing to the relativistic precession, the most bound part of the stellar debris (with an elliptical orbit characterized by a semi-major axis $a_{\rm min}$) precess by an angle $\Delta\phi$ after pericentre passage. As a result, this part of the stream that recedes from the MBH with velocity $v_{\rm out}$ collides with the part of the stream still approaching the MBH with velocity $v_{\rm in}$. This encounter occurs at a distance $R_{\rm int}$ from the MBH. The dotted lines with arrows show possible subsequent secondary intersections of the streams. The time evolution of the orbit is indexed by the roman number VII, label that is the continuation of the ones in Fig. 4. Figure credit: Taj Jankovič.

3. Observations

With the increasing number of TDEs, it has become feasible to conduct detailed comparisons between the observed events and theoretical expectations regarding their emissions. These comparisons aim to deduce the physical parameters of the events, such as black hole mass and stellar type. However, the process of understanding the disparities between the observations and the fundamental predictions for emissions from an accreting debris disc poses a significant challenge. It necessitates significant modifications to the simplest emission models in order to try to reconcile the differences [7].

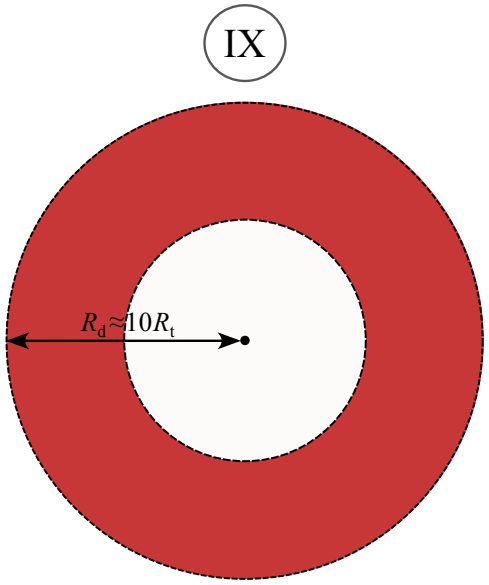

Figure 6: Sketch showing the accretion disc (in red) after the process of circularization of the the debris stream. The external radius of the disc is denoted by R_d. The time evolution of the process is indexed by the roman number IX, label that is the continuation of the one in Fig. 5. Figure credit: Taj Jankovič.

3.1. Light Curves

A key characteristic of the debris stream fallback is that if its specific energy distribution is uniform, represented by dE/dM = 0, the rate at which material returns to pericenter follows a power-law pattern, as given by Eq. 11. Specifically, the rate can be described as $dM/dt \propto (t - t_{\rm D})^{-5/3}$. In the case of a partial disruption, a steeper power-law decline is anticipated, resulting in $dM/dt \propto (t - t_{\rm D})^{-9/4}$ [37].

Furthermore, the star's internal structure [34, 38, 39] and spin [40], the spin of the MBH [41, 42], and the impact parameter of the star's orbit [42], all play a role in shaping the energy distribution of the debris and, consequently, the fallback rate.

Light curves (LCs) are a type of observations consisting in time series of flux measurements. These flux variations in individual astronomical objects, as captured through light curves, have been the mainstay for making scientific discoveries [43]. TDE candidates have been observed in the X-ray, UV/optical, IR and radio wavebands, but typically detected in the UV (as shown in Fig. 7) and optical wavebands.

One of the most striking observed features of TDEs is that, at first glance,

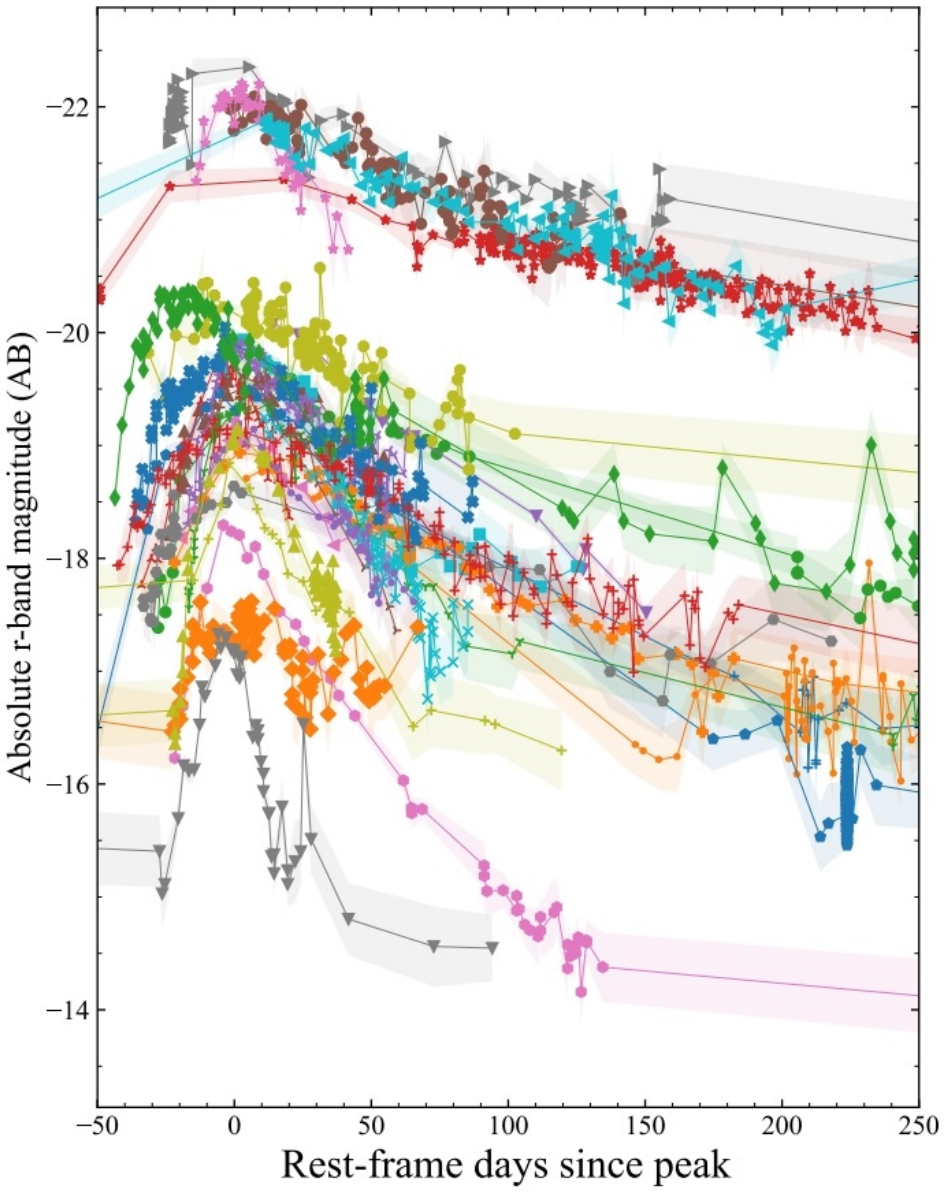

Figure 7: Compilation of TDE light curves. The *r*-band absolute magnitude for a selected sample of 30 spectroscopically classified TDEs from the Zwicky Transient Facility Phase I survey operations with follow-up *Swift* UV and X-ray measurements. Figure slightly modified from [44]

.

their LCs seem to exhibit a general resemblance to the theoretical TDE fallback rate. In fact, when a $t^{-5/3}$ power law is fitted to the LC during its decline from the peak, a strong correlation emerges between the time of peak since the estimated disruption time, denoted as $\Delta t = (t_{\rm peak} - t_{\rm D})$, and the inferred MBH mass. This correlation follows the expected pattern for the fallback timescale, where $\Delta t \propto M_{\rm BH}^{1/2}$, as demonstrated in studies by [45, 15]. However, deviations may arise from the density profile of the star [46] or relativistic effects [47].
The main takeaway in the importance of the observation of the TDE light curves is the potential determination of different parameters in relation to the disruption, such as penetration factor β and eccentricity e of the initial stellar orbit, mass $M_\star$ and radius $R_\star$ the disrupted star, mass $M_{\rm BH}$ and spin of the MBH, as well as the investigation of the MBH environment properties and the study of general relativistic (GR) effects associated with this phenomenon.

3.2. Mechanisms of emission

The advancement in utilizing TDEs to explore MBH demographics has been significantly hindered by the current limited comprehension of the mechanism responsible for the emission in TDEs. Over the past ten years, observations of TDEs have progressed more rapidly than the development of theoretical models [7]. Numerous crucial aspects of TDE characteristics remain to be conclusively and consistently explained by a scientifically motivated model that accounts for the formation of the debris from tidal disruption and its subsequent organization into an accretion disc. Nonetheless, the objective of this section is to present our most up-to-date understanding of the most favored mechanisms driving TDE emissions, with the hopes that a deeper theoretical understanding will soon be achieved to undoubtedly and totally account for these emissions. These mechanisms include:

1. Thermal emission in the X-ray waveband from the circularized debris disc.
2. Reprocessing of a fraction of the soft X-ray photons from an accretion flow, released as debris accretes onto the black hole, by an optically-thick structure and re-emitted into the UV/optical wavebands [48, 49, 50]. In this scenario, the ability to detect X-ray emissions would rely on the angle from which they are viewed. For instance, X-ray photons might retain the capacity to exit through the funnels of a thick torus, yet not along its plane of orbit. This viewing angle effect is illustrated in Fig. 8.

3. Synchrotron emission in the radio waveband from internal shocks in a relativistic freely expanding canonical jet. [51].

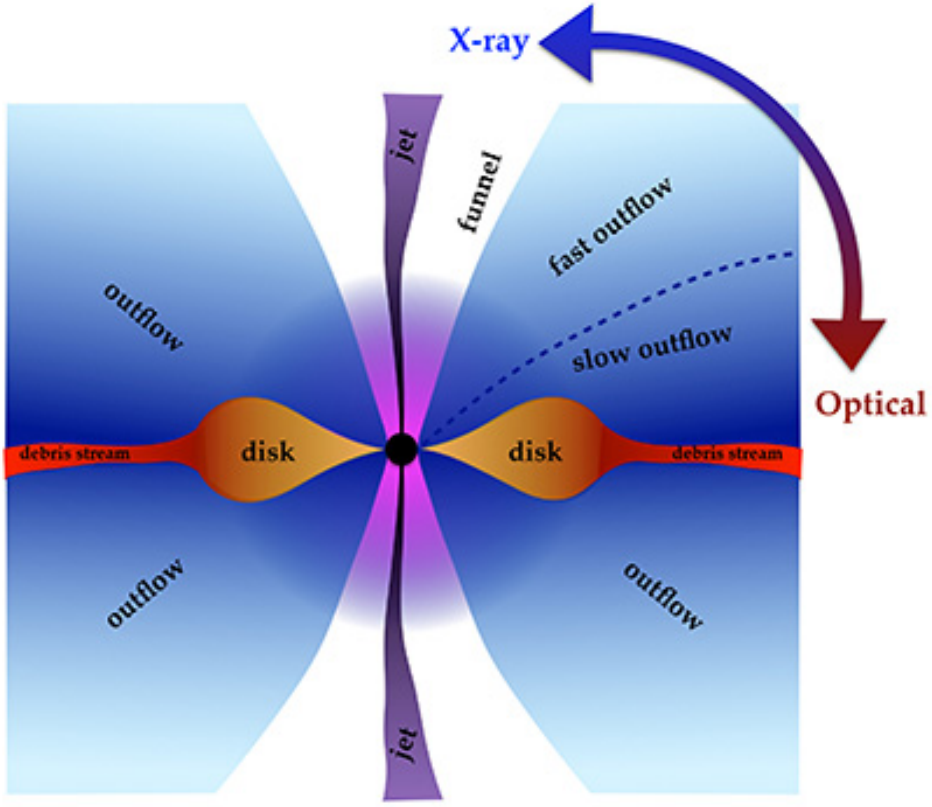

Figure 8: Sketch of emissions stemming from a tidal disruption event depicts, in a sliced view, the outcome when a black hole consumes material from a torn-apart star. This material shapes an accretion disc that warms up and releases substantial quantities of light and energy. The wavebands of observable emission from Earth are contingent upon how the viewing angle aligns with the MBH's orientation. Figure credit: Jane Lixin Dai.

4. Hydrodynamical simulations

There exist two fundamental approaches to express the governing physical equations: the Eulerian approach and the Lagrangian approach. Eulerian techniques involve the utilization of geometric grids, which can either be fixed or adaptable, and they compute derivatives at established spatial points indicated by the grid. These methodologies laid the foundation for

computational fluid dynamics, which emerged in the 1960's and 1970's, and they continue to be the most prevalent approach today. In contrast, Lagrangian techniques calculate derivatives within a coordinate system connected to a fluid element in motion. These two methods can be likened to a boat tracing the course of a river, the Lagrangian approach, as opposed to being stationed on the riverbank observing the flow of the river, the Eulerian approach [20].

Within the Lagrangian approach, as each grid node moves in tandem with the material it represents, the relative displacement of connecting nodes can lead to a deformation of the mesh cell. During this deformation, mass, momentum, and energy are conveyed along with the mesh cell's motion. Each cell maintains a constant mass, preventing any mass flux between neighboring cells. Nonetheless, this technique can pose challenges when dealing with highly distorted meshes. For instance, instances where the mesh becomes extremely distorted can significantly compromise the accuracy of the formulation and subsequent solutions [52].

Conversely, in the Eulerian method, grid nodes and cells remain fixed in space, irrespective of the material's movement across the grid. As such, substantial deformations do not impact the mesh itself, avoiding the numerical complications encountered in the Lagrangian method. This characteristic makes the Eulerian method more prominent in computational fluid dynamics, particularly in scenarios dominated by material flow. However, this method also exhibits certain drawbacks. Notably, the grid must be sufficiently large to encompass the entire area where material might flow. This pursuit of computational efficiency can lead to coarser grids, which can sacrifice resolution and accuracy [52].

Nowadays, a numerical code known as "Phantom" has been effectively employed for the investigation of TDEs [53, 54, 55, 56, 39, 57, 58, 59, 60]. Developed by [61], this code is designed for astrophysical applications in three dimensions and boasts attributes such as rapid computation, parallel processing, modularity, and minimal memory usage. Phantom is based on the SPH (Smoothed Particle Hydrodynamics) Lagrangian modeling method initially proposed by [62] and [63]. This approach, devoid of a grid, represents fluid elements through discrete particles that obey hydrodynamic flow equations. The SPH technique, renowned for its adaptability, has been extensively utilized to simulate various phenomena in the realm of astrophysics.

SPH characterizes the fluid using discrete mass elements, defined as particles. These particles' attributes are determined by calculating appropriate means involving neighboring particles positioned within a smoothing

region around them. Within this smoothing region, particles gain lower weight as they lie close to the edge, which defines the *smoothing kernel* W, usually a function that resembles a bell curve with compact support. Other relevant parameters to this setup include the *smoothing length* h, which sets the size of the kernel, and N, the number of neighbouring particles within the kernel, which together allows to introduce the density ρ at the location of particle 'i' as

$$\rho(\vec{r}_i) = \sum_{j=1}^{N} m_j W(\vec{r}_i - \vec{r}_j, h) \tag{12}$$

Every particle possesses its individual smoothing length h. This value is determined in a way that ensures each particle is in proximity to a roughly consistent count of neighboring particles, as outlined by [64]. This smoothing distance can be expressed as

$$h(\vec{r}_i) = \eta \left(\frac{m_i}{\rho_i} \right)^{1/3} \tag{13}$$

In accordance with the findings of [65], the parameter η ought to be selected within the interval of 1.2 to 1.5. Consequently, SPH offers a notable advantage where the level of resolution aligns with density. This means that regions with higher densities exhibit shorter smoothing lengths, resulting in enhanced spatial precision. As a result, SPH inherently functions as an adaptive technique, as pointed out by [65, 66].

5. Challenges and Potential Future Work

While significant progress has been made in understanding TDEs, there are still several aspects that remain poorly understood or are a focus of increasing interest. An example of the first situation is the optical emission mechanism in TDEs. Although the origin of this phenomenon is believed to stem either from shocks resulting from intersections within the self-interacting debris stream of the star [67, 68], or from the debris reprocessing the emission originating from an accretion disc [69, 70, 50, 71], uncertainties persist. Questions remain regarding the luminosity of shocks generated by the self-intersections of the stream, while in the case of the reprocessing scenario, fundamental uncertainties persist concerning the location of the reprocessing material, its formation process, the extent of its coverage in relation to the MBH, its efficiency in transforming disc emission into optical wavelengths, and how all of these variables are influenced

by the characteristics of both the MBH and the disrupted star [72].
For an example of the second situation, the observation of the neutron star binary merger event GW170817, detected both as a gravitational and EM wave signal, marked the commencement of a revolutionary phase in multi-messenger astronomy [73]. This remarkable event exemplified the unprecedented potential of amalgamating data from gravitational waves and EM to unveil profound details about astrophysical transient phenomena [7]. As the strain of the gravitational wave (GW) generated by a binary system follows a scaling law represented by [7],

$$h \approx \frac{R_g G M_\star}{D R_p c^2} \approx 2 \times 10^{-22} \left(\frac{10\,\mathrm{Mpc}}{D} \right) \left[\frac{\left(m_\star^2 M_6 \right)^{2/3}}{r_\star} \right] \beta, \tag{14}$$

And a wave frequency corresponding to

$$f \approx \sqrt{\frac{G M_{\mathrm{BH}}}{R_p^3}} \approx 6 \times 10^{-4} \sqrt{\frac{\beta^3 m_\star}{r_\star^3}} \mathrm{Hz}, \tag{15}$$

the optimal astrophysical configuration to detect a tidal disruption event (TDE) using GWs arises when a compact star, such as a white dwarf, undergoes tidal disruption during a close encounter with a black hole [7]. This is particularly feasible with a low-frequency GW detector like the Laser Interferometer Space Antenna (LISA), extending up to a distance of 10 kpc [74, 65, 75]. This preference aligns once again with the likelihood of a TDE occurring around an IMBH, which enhances its significance as a tool for investigating speculated IMBHs within dwarf galaxy nuclei or globular clusters [76]. The combined detection of both GW and EM signals allows the utilization of the chirp mass derived from the GW signal, along with precise timing data from the star's pericenter passage and the EM emission from debris streams, enabling the detailed modeling of the accretion flow and the determination of accurate timescales for circularization and accretion processes [77].
Instances of GW emissions resulting from the TDEs by MBH have been replicated under specific conditions using a general relativistic implementation of the PHANTOM code. In these investigations, the disrupted stars have been emulated as polytropic spheres characterized by a parameter γ equal to $5/3$. The simulated GW signals originating from these TDEs have been verified to align with the theoretical projections derived from earlier research, under chosen parameters. Notably, these studies have unveiled intriguing findings about how variations in certain parameters (such

as MBH spin, orbital eccentricity and inclination of the stellar trajectory) impact the gravitational signals. Consequently, a collection of templates for GW waveforms generated during TDEs has been made available to the public. It is feasible to customize this openly accessible code to investigate gravitational emissions from both familiar and more unconventional scenarios [78].
These two situations, given only as a matter of exemplification, allow to the exploration of new insights in the simulation of TDEs. For example, it is possible to consider the simulations of more realistic stellar density profiles instead of the toy-model profiles given by the polytropic equation of state, using current publicly available software such as the Modules for Experiments in Stellar Astrophysics (MESA), an open-source 1D stellar evolution code [79]. This facilitates the chances to explore gravitational emission from more realistic scenarios in the context of TDEs.

6. Conclusions

Through a comprehensive examination of TDE phenomena, this review has shed light on some of the significant progress and intriguing challenges. The observations of TDEs across different wavebands, such as X-ray, UV/optical, IR, and radio, have yielded a wealth of data that provide critical insights into the physical parameters of these events, including the black hole mass, the stellar type, the penetration factor, and eccentricity of the initial stellar orbit. The pronounced correlation between the time of peak and the inferred MBH mass shows a concrete example of the potential of TDE light curves as valuable tools for probing the dynamics of these systems.
Nevertheless, the mechanisms driving TDE emissions remain an ongoing subject of inquiry. While thermal X-ray emission from the circularized debris disc and reprocessing of X-ray photons into the UV and optical waveband offer plausible explanations, there is still room for improvement.
The utilization of advanced numerical techniques, such as the Smoothed Particle Hydrodynamics (SPH) method, in hydrodynamical simulations has provided invaluable insights into TDE dynamics.
Looking ahead, several challenges and future research avenues within the TDE field become evident. The precise mechanisms driving TDE emissions, the impact of varying parameters on gravitational wave signals, and the integration of more sophisticated stellar evolution models into simulations are all areas ripe for exploration. As the understanding of TDEs

deepens, unprecedented insights into MBH demographics, their environment and disrupted star properties, and the underlying principles governing these astrophysical transient phenomena may emerge.

Acknowledgements

This research review was supported by the Slovenian Research Agency grants P1-0031 and the Young Researchers program. We thank Taj Jankovič for helpful discussions while completing the write up of this work.

References

[1] J. G. Hills, Possible power source of Seyfert galaxies and QSOs, 254 (5498) (1975) 295–298. doi:10.1038/254295a0.

[2] V. V. Lidskii, L. M. Ozernoi, Tidal triggering of stellar flares by a massive black hole, Soviet Astronomy Letters 5 (1979) 16–19.

[3] M. J. Rees, Tidal disruption of stars by black holes of 106–108 solar masses in nearby galaxies, Nature 333 (6173) (1988) 523–528.

[4] E. S. Phinney, Manifestations of a Massive Black Hole in the Galactic Center, in: M. Morris (Ed.), The Center of the Galaxy, Vol. 136 of IAU Symposium, 1989, p. 543.

[5] C. R. Evans, C. S. Kochanek, The tidal disruption of a star by a massive black hole, The Astrophysical Journal 346 (1989) L13–L16.

[6] A. Ulmer, Flares from the Tidal Disruption of Stars by Massive Black Holes, 514 (1) (1999) 180–187. doi:10.1086/306909.

[7] S. Gezari, Tidal disruption events, Annual Review of Astronomy and Astrophysics 59 (2021) 21–58.

[8] J. L. Donley, W. N. Brandt, M. Eracleous, T. Boller, Large-Amplitude X-Ray Outbursts from Galactic Nuclei: A Systematic Survey using ROSAT Archival Data, 124 (3) (2002) 1308–1321. arXiv:astro-ph/0206291, doi:10.1086/342280.

[9] P. Esquej, R. D. Saxton, S. Komossa, A. M. Read, M. J. Freyberg, G. Hasinger, D. A. García-Hernández, H. Lu, J. Rodriguez Zaurín, M. Sánchez-Portal, H. Zhou, Evolution of tidal disruption candidates discovered by XMM-Newton, 489 (2) (2008) 543–554. arXiv:0807.4452, doi:10.1051/0004-6361:200810110.

[10] S. Gezari, T. Heckman, S. B. Cenko, M. Eracleous, K. Forster, T. S. Gonçalves, D. C. Martin, P. Morrissey, S. G. Neff, M. Seibert, D. Schiminovich, T. K. Wyder, Luminous Thermal Flares from Quiescent Supermassive Black Holes, 698 (2) (2009) 1367–1379. arXiv:0904.1596, doi:10.1088/0004-637X/698/2/1367.

[11] S. van Velzen, G. R. Farrar, Measurement of the Rate of Stellar Tidal Disruption Flares, 792 (1) (2014) 53. arXiv:1407.6425, doi:10.1088/0004-637X/792/1/53.

[12] T. W. S. Holoien, C. S. Kochanek, J. L. Prieto, K. Z. Stanek, S. Dong, B. J. Shappee, D. Grupe, J. S. Brown, U. Basu, J. F. Beacom, D. Bersier, J. Brimacombe, A. B. Danilet, E. Falco, Z. Guo, J. Jose, G. J. Herczeg, F. Long, G. Pojmanski, G. V. Simonian, D. M. Szczygieł, T. A. Thompson, J. R. Thorstensen, R. M. Wagner, P. R. Woźniak, Six months of multiwavelength follow-up of the tidal disruption candidate ASASSN-14li and implied TDE rates from ASAS-SN, 455 (3) (2016) 2918–2935. arXiv:1507.01598, doi:10.1093/mnras/stv2486.

[13] S. van Velzen, On the Mass and Luminosity Functions of Tidal Disruption Flares: Rate Suppression due to Black Hole Event Horizons, 852 (2) (2018) 72. arXiv:1707.03458, doi:10.3847/1538-4357/aa998e.

[14] T. Hung, S. Gezari, N. Blagorodnova, N. Roth, S. B. Cenko, S. R. Kulkarni, A. Horesh, I. Arcavi, C. McCully, L. Yan, R. Lunnan, C. Fremling, Y. Cao, P. E. Nugent, P. Wozniak, Revisiting Optical Tidal Disruption Events with iPTF16axa, 842 (1) (2017) 29. arXiv:1703.01299, doi:10.3847/1538-4357/aa7337.

[15] S. van Velzen, T. W. S. Holoien, F. Onori, T. Hung, I. Arcavi, Optical-Ultraviolet Tidal Disruption Events, arXiv e-prints (2020) arXiv:2008.05461arXiv:2008.05461.

[16] X. Zhang, Central bh mass of tidal disruption event candidate sdss j0159 through long-term optical variabilities, The Astrophysical Journal 948 (1) (2023) 68. doi:10.3847/1538-4357/acc182.
URL https://dx.doi.org/10.3847/1538-4357/acc182

[17] K. Bricman, A. Gomboc, The prospects of observing tidal disruption events with the large synoptic survey telescope, The Astrophysical Journal 890 (1) (2020) 73.

[18] Snowmass2021 Cosmic Frontier White Paper: Rubin Observatory after LSST.
URL https://www.osti.gov/biblio/1861822

[19] E. M. Rossi, N. C. Stone, J. A. P. Law-Smith, M. Macleod, G. Lodato, J. L. Dai, I. Mandel, The process of stellar tidal disruption by supermassive black holes, Space Science Reviews 217 (3) (2021) 40. doi:10.1007/s11214-021-00818-7.
URL https://doi.org/10.1007/s11214-021-00818-7

[20] A. Clerici, A. Gomboc, A study of stellar debris dynamics during a tidal disruption event, Doctoral dissertation, Graduate School, Nova Gorica (03 Aug 2023 2020).
URL https://repozitorij.ung.si/IzpisGradiva.php?lang=eng&id=5853

[21] K. Bučar Bricman, A. Gomboc, Tidal disruption events seen through the eyes of vera c. rubin observatory, Doktorska disertacija, Fakulteta za podiplomski študij, Nova Gorica (2021).
URL https://repozitorij.ung.si/IzpisGradiva.php?lang=slv&id=7002

[22] Ivanov, P. B., Chernyakova, M. A., Relativistic cross sections of mass stripping and tidal disruption of a star by a super-massive rotating black hole, A&A 448 (3) (2006) 843–852. doi:10.1051/0004-6361:20053409.
URL https://doi.org/10.1051/0004-6361:20053409

[23] M. Kesden, Tidal-disruption rate of stars by spinning supermassive black holes, Phys. Rev. D 85 (2012) 024037. doi:10.1103/PhysRevD.85.024037.
URL https://link.aps.org/doi/10.1103/PhysRevD.85.024037

[24] E. Phinney, Manifestations of a massive black hole in the galactic center, in: Symposium-International Astronomical Union, Vol. 136, Cambridge University Press, 1989, pp. 543–553.

[25] N. Stone, R. Sari, A. Loeb, Consequences of strong compression in tidal disruption events, Monthly Notices of the Royal Astronomical Society 435 (3) (2013) 1809–1824. doi:10.1093/mnras/stt1270.
URL https://doi.org/10.1093/mnras/stt1270

[26] S. Gezari, The tidal disruption of stars by supermassive black holes, Physics Today 67 (5) (2014) 37–42. doi:10.1063/PT.3.2382.
URL https://doi.org/10.1063/PT.3.2382

[27] C. Bonnerot, Dynamics and radiation from tidal disruption events, Ph.D. thesis, Leiden Observatory, Science, Leiden University (10 2017).

[28] G. Lodato, E. M. Rossi, Multiband light curves of tidal disruption events, Monthly Notices of the Royal Astronomical Society 410 (1) (2011) 359–367.

[29] G. Lodato, A. King, J. Pringle, Stellar disruption by a supermassive black hole: is the light curve really proportional to t- 5/3?, Monthly Notices of the Royal Astronomical Society 392 (1) (2009) 332–340.

[30] J. Guillochon, H. Manukian, E. Ramirez-Ruiz, Ps1-10jh: the disruption of a main-sequence star of near-solar composition, The Astrophysical Journal 783 (1) (2014) 23.

[31] C. S. Kochanek, The dynamics of luminous galaxies in isothermal halos, The Astrophysical Journal 436 (1994) 56.
URL https://api.semanticscholar.org/CorpusID:121262725

[32] L. Dai, J. C. McKinney, M. C. Miller, Soft x-ray temperature tidal disruption events from stars on deep plunging orbits, The Astrophysical Journal Letters 812 (2) (2015) L39.

[33] C. Bonnerot, E. M. Rossi, G. Lodato, Long-term stream evolution in tidal disruption events, Monthly Notices of the Royal Astronomical Society 464 (3) (2017) 2816–2830. doi:10.1093/mnras/stw2547.
URL https://doi.org/10.1093/mnras/stw2547

[34] E. Ramirez-Ruiz, S. Rosswog, The star ingesting luminosity of intermediate-mass black holes in globular clusters, The Astrophysical Journal 697 (2) (2009) L77.

[35] S. Rosswog, E. Ramirez-Ruiz, W. R. Hix, Tidal disruption and ignition of white dwarfs by moderately massive black holes, The Astrophysical Journal 695 (1) (2009) 404.

[36] H. Shiokawa, J. H. Krolik, R. M. Cheng, T. Piran, S. C. Noble, General relativistic hydrodynamic simulation of accretion flow from a stellar tidal disruption, The Astrophysical Journal 804 (2) (2015) 85.

[37] E. R. Coughlin, C. J. Nixon, Partial Stellar Disruption by a Supermassive Black Hole: Is the Light Curve Really Proportional to t $^{-9/4}$?, 883 (1) (2019) L17. arXiv:1907.03034, doi:10.3847/2041-8213/ab412d.

[38] J. Guillochon, E. Ramirez-Ruiz, Hydrodynamical Simulations to Determine the Feeding Rate of Black Holes by the Tidal Disruption of Stars: The Importance of the Impact Parameter and Stellar Structure, 767 (1) (2013) 25. arXiv:1206.2350, doi:10.1088/0004-637X/767/1/25.

[39] E. C. A. Golightly, C. J. Nixon, E. R. Coughlin, On the Diversity of Fallback Rates from Tidal Disruption Events with Accurate Stellar Structure, 882 (2) (2019) L26. arXiv:1907.05895, doi:10.3847/2041-8213/ab380d.

[40] E. C. A. Golightly, E. R. Coughlin, C. J. Nixon, Tidal Disruption Events: The Role of Stellar Spin, 872 (2) (2019) 163. arXiv:1901.03717, doi:10.3847/1538-4357/aafd2f.

[41] M. Kesden, Black-hole spin dependence in the light curves of tidal disruption events, 86 (6) (2012) 064026. arXiv:1207.6401, doi:10.1103/PhysRevD.86.064026.

[42] E. Gafton, S. Rosswog, Tidal disruptions by rotating black holes: effects of spin and impact parameter, 487 (4) (2019) 4790–4808. arXiv:1903.09147, doi:10.1093/mnras/stz1530.

[43] A. Mahabal, K. Sheth, F. Gieseke, A. Pai, S. G. Djorgovski, A. J. Drake, M. J. Graham, Deep-learnt classification of light curves, in: 2017 IEEE Symposium Series on Computational Intelligence (SSCI), IEEE, 2017. doi:10.1109/ssci.2017.8280984.
URL https://doi.org/10.1109%2Fssci.2017.8280984

[44] E. Hammerstein, S. van Velzen, S. Gezari, S. B. Cenko, Y. Yao, C. Ward, S. Frederick, N. Villanueva, J. J. Somalwar, M. J. Graham, S. R. Kulkarni, D. Stern, I. Andreoni, E. C. Bellm, R. Dekany, S. Dhawan, A. J. Drake, C. Fremling, P. Gatkine, S. L. Groom, A. Y. Q. Ho, M. M. Kasliwal, V. Karambelkar, E. C. Kool, F. J. Masci, M. S. Medford, D. A. Perley, J. Purdum, J. v. Roestel, Y. Sharma, J. Sollerman, K. Taggart, L. Yan, The final season reimagined: 30 tidal disruption events from the ztf-i survey, The Astrophysical Journal 942 (1) (2023) 9. doi:

10.3847/1538-4357/aca283.
URL https://dx.doi.org/10.3847/1538-4357/aca283

[45] S. van Velzen, N. C. Stone, B. D. Metzger, S. Gezari, T. M. Brown, A. S. Fruchter, Late-time UV Observations of Tidal Disruption Flares Reveal Unobscured, Compact Accretion Disks, 878 (2) (2019) 82. arXiv:1809.00003, doi:10.3847/1538-4357/ab1844.

[46] G. Lodato, A. R. King, J. E. Pringle, Stellar disruption by a supermassive black hole: is the light curve really proportional to t5/3?, Monthly Notices of the Royal Astronomical Society 392 (1) (2009) 332–340. doi:10.1111/j.1365-2966.2008.14049.x.
URL https://doi.org/10.1111/j.1365-2966.2008.14049.x

[47] M. Kesden, Black-hole spin dependence in the light curves of tidal disruption events, Physical Review D 86 (6) (2012) 064026.

[48] J. Guillochon, H. Manukian, E. Ramirez-Ruiz, PS1-10jh: The Disruption of a Main-sequence Star of Near-solar Composition, 783 (1) (2014) 23. arXiv:1304.6397, doi:10.1088/0004-637X/783/1/23.

[49] B. D. Metzger, N. C. Stone, A bright year for tidal disruptions, 461 (1) (2016) 948–966. arXiv:1506.03453, doi:10.1093/mnras/stw1394.

[50] N. Roth, D. Kasen, J. Guillochon, E. Ramirez-Ruiz, The X-Ray through Optical Fluxes and Line Strengths of Tidal Disruption Events, 827 (1) (2016) 3. arXiv:1510.08454, doi:10.3847/0004-637X/827/1/3.

[51] D. R. Pasham, S. van Velzen, Discovery of a Time Lag between the Soft X-Ray and Radio Emission of the Tidal Disruption Flare ASASSN-14li: Evidence for Linear Disk-Jet Coupling, 856 (1) (2018) 1. arXiv:1709.02882, doi:10.3847/1538-4357/aab361.

[52] G. R. Liu, M. B. Liu, S. Li, "smoothed particle hydrodynamics —a meshfree method", Computational Mechanics 33 (6) (2004) 491–491. doi:10.1007/s00466-004-0573-1.
URL https://doi.org/10.1007/s00466-004-0573-1

[53] E. R. Coughlin, C. Nixon, Variability in Tidal Disruption Events: Gravitationally Unstable Streams, 808 (2015) L11. arXiv:1506.08194, doi:10.1088/2041-8205/808/1/L11.

[54] E. R. Coughlin, C. Nixon, M. C. Begelman, P. J. Armitage, D. J. Price, Post-periapsis pancakes: sustenance for self-gravity in tidal disruption events, 455 (2016) 3612–3627. arXiv:1510.08066, doi:10.1093/mnras/stv2511.

[55] E. R. Coughlin, C. Nixon, M. C. Begelman, P. J. Armitage, On the structure of tidally disrupted stellar debris streams, 459 (2016) 3089–3103. arXiv:1603.00873, doi:10.1093/mnras/stw770.

[56] C. Bonnerot, E. M. Rossi, G. Lodato, D. J. Price, Disc formation from tidal disruptions of stars on eccentric orbits by Schwarzschild black holes, 455 (2) (2016) 2253–2266. arXiv:1501.04635, doi:10.1093/mnras/stv2411.

[57] M. Toscani, G. Lodato, R. Nealon, Gravitational wave emission from unstable accretion discs in tidal disruption events, Monthly Notices of the Royal Astronomical Society 489 (1) (2019) 699–706. doi:10.1093/mnras/stz2201.
URL https://doi.org/10.1093/mnras/stz2201

[58] A. Sacchi, G. Lodato, 'Failed' tidal disruption events and X-ray flares from the Galactic Centre, 486 (2) (2019) 1833–1839. arXiv:1904.02424, doi:10.1093/mnras/stz981.

[59] A. Sacchi, G. Lodato, C. Toci, V. Motta, What causes the fragmentation of debris streams in tdes?, Monthly Notices of the Royal Astronomical Society 495 (1) (2020) 1227–1238. doi:10.1093/mnras/staa1299.
URL https://doi.org/10.1093/mnras/staa1299

[60] E. R. Coughlin, The dynamics of debris streams from tidal disruption events: exact solutions, critical stream density, and hydrogen recombination, Monthly Notices of the Royal Astronomical Society 522 (4) (2023) 5500–5516. doi:10.1093/mnras/stad1347.
URL https://doi.org/10.1093/mnras/stad1347

[61] D. J. Price, J. Wurster, T. S. Tricco, C. Nixon, S. Toupin, A. Pettitt, C. Chan, D. Mentiplay, G. Laibe, S. Glover, C. Dobbs, R. Nealon, D. Liptai, H. Worpel, C. Bonnerot, G. Dipierro, G. Ballabio, E. Ragusa, C. Federrath, R. Iaconi, T. Reichardt, D. Forgan, M. Hutchison, T. Constantino, B. Ayliffe, K. Hirsh, G. Lodato, Phantom: A smoothed particle hydrodynamics and magnetohydrodynamics code for astrophysics, Publications of the Astronomical Society of Australia 35 (2018) e031. doi:DOI:10.1017/pasa.2018.25.

[62] L. B. Lucy, A numerical approach to the testing of the fission hypothesis., 82 (1977) 1013–1024. doi:10.1086/112164.

[63] R. A. Gingold, J. J. Monaghan, Smoothed particle hydrodynamics: theory and application to non-spherical stars, Monthly Notices of the Royal Astronomical Society 181 (3) (1977) 375–389. doi:10.1093/mnras/181.3.375.
URL https://doi.org/10.1093/mnras/181.3.375

[64] L. Hernquist, N. Katz, TREESPH: A Unification of SPH with the Hierarchical Tree Method, 70 (1989) 419. doi:10.1086/191344.

[65] S. Rosswog, E. Ramirez-Ruiz, W. R. Hix, Tidal Disruption and Ignition of White Dwarfs by Moderately Massive Black Holes, 695 (1) (2009) 404–419. arXiv:0808.2143, doi:10.1088/0004-637X/695/1/404.

[66] G. Lodato, R. M. Cheng, C. Bonnerot, J. L. Dai, Simulations of tidal disruption events, Space Science Reviews 216 (4) (2020) 63. doi:10.1007/s11214-020-00697-4.
URL https://doi.org/10.1007/s11214-020-00697-4

[67] H. Shiokawa, J. H. Krolik, R. M. Cheng, T. Piran, S. C. Noble, GENERAL RELATIVISTIC HYDRODYNAMIC SIMULATION OF ACCRETION FLOW FROM A STELLAR TIDAL DISRUPTION, The Astrophysical Journal 804 (2) (2015) 85. doi:10.1088/0004-637X/804/2/85.
URL https://iopscience.iop.org/article/10.1088/0004-637X/804/2/85

[68] T. Piran, G. Svirski, J. Krolik, R. M. Cheng, H. Shiokawa, Disk Formation Versus Disk Accretion—What Powers Tidal Disruption Events?, 806 (2) (2015) 164. arXiv:1502.05792, doi:10.1088/0004-637X/806/2/164.

[69] A. Loeb, A. Ulmer, Optical Appearance of the Debris of a Star Disrupted by a Massive Black Hole, 489 (2) (1997) 573–578. arXiv:astro-ph/9703079, doi:10.1086/304814.

[70] A. Ulmer, B. Paczynski, J. Goodman, Tidal disruption Eddington envelopes around massive black holes, Astronomy & Astrophysics 333 (1998) 379–384.
URL http://articles.adsabs.harvard.edu/cgi-bin/nph-iarticle_query?1998A%26A...333..379U&data_

type=PDF_HIGH&whole_paper=YES&type=PRINTER&filetype=.pdf

[71] N. Roth, D. Kasen, What Sets the Line Profiles in Tidal Disruption Events?, 855 (1) (2018) 54. arXiv:1707.02993, doi:10.3847/1538-4357/aaaec6.

[72] A. Malyali, A. Rau, A. Merloni, K. Nandra, J. Buchner, Z. Liu, S. Gezari, J. Sollerman, B. Shappee, B. Trakhtenbrot, I. Arcavi, C. Ricci, S. van Velzen, A. Goobar, S. Frederick, A. Kawka, L. Tartaglia, J. Burke, D. Hiramatsu, M. Schramm, D. van der Boom, G. Anderson, J. C. A. Miller-Jones, E. Bellm, A. Drake, D. Duev, C. Fremling, M. Graham, F. Masci, B. Rusholme, M. Soumagnac, R. Walters, At 2019avd: a novel addition to the diverse population of nuclear transients, A&A 647 (2021).
URL https://doi.org/10.1051/0004-6361/202039681

[73] B. P. Abbott, R. Abbott, T. D. Abbott, F. Acernese, K. Ackley, C. Adams, T. Adams, P. Addesso, R. X. Adhikari, V. B. Adya, C. Affeldt, M. Afrough, B. Agarwal, M. Agathos, K. Agatsuma, N. Aggarwal, O. D. Aguiar, L. Aiello, A. Ain, P. Ajith, B. Allen, G. Allen, A. Allocca, P. A. Altin, A. Amato, A. Ananyeva, S. B. Anderson, W. G. Anderson, S. V. Angelova, S. Antier, S. Appert, K. Arai, M. C. Araya, J. S. Areeda, N. Arnaud, K. G. Arun, S. Ascenzi, G. Ashton, M. Ast, S. M. Aston, P. Astone, D. V. Atallah, P. Aufmuth, C. Aulbert, K. AultONeal, C. Austin, A. Avila-Alvarez, S. Babak, P. Bacon, M. K. M. Bader, S. Bae, P. T. Baker, F. Baldaccini, G. Ballardin, S. W. Ballmer, S. Banagiri, J. C. Barayoga, S. E. Barclay, B. C. Barish, D. Barker, K. Barkett, F. Barone, B. Barr, L. Barsotti, M. Barsuglia, D. Barta, S. D. Barthelmy, J. Bartlett, I. Bartos, R. Bassiri, A. Basti, J. C. Batch, M. Bawaj, J. C. Bayley, M. Bazzan, B. Bécsy, C. Beer, M. Bejger, I. Belahcene, A. S. Bell, B. K. Berger, G. Bergmann, J. J. Bero, C. P. L. Berry, D. Bersanetti, A. Bertolini, J. Betzwieser, S. Bhagwat, R. Bhandare, I. A. Bilenko, G. Billingsley, C. R. Billman, J. Birch, R. Birney, O. Birnholtz, S. Biscans, S. Biscoveanu, A. Bisht, M. Bitossi, C. Biwer, M. A. Bizouard, J. K. Blackburn, J. Blackman, C. D. Blair, D. G. Blair, R. M. Blair, S. Bloemen, O. Bock, N. Bode, M. Boer, G. Bogaert, A. Bohe, F. Bondu, E. Bonilla, R. Bonnand, B. A. Boom, R. Bork, V. Boschi, S. Bose, K. Bossie, Y. Bouffanais, A. Bozzi, C. Bradaschia, P. R. Brady, M. Branchesi, J. E. Brau, T. Briant, A. Brillet, M. Brinkmann, V. Brisson, P. Brockill, J. E. Broida, A. F. Brooks, D. A. Brown, D. D. Brown, S. Brunett, C. C. Buchanan, A. Buikema, T. Bulik,

H. J. Bulten, A. Buonanno, D. Buskulic, C. Buy, R. L. Byer, M. Cabero, LIGO Scientific Collaboration, Virgo Collaboration, Multi-messenger Observations of a Binary Neutron Star Merger, 848 (2) (2017) L12. arXiv:1710.05833, doi:10.3847/2041-8213/aa91c9.

[74] S. Kobayashi, P. Laguna, E. S. Phinney, P. Mészáros, Gravitational Waves and X-Ray Signals from Stellar Disruption by a Massive Black Hole, 615 (2) (2004) 855–865. arXiv:astro-ph/0404173, doi:10.1086/424684.

[75] P. Anninos, P. C. Fragile, S. S. Olivier, R. Hoffman, B. Mishra, K. Camarda, Relativistic Tidal Disruption and Nuclear Ignition of White Dwarf Stars by Intermediate-mass Black Holes, 865 (1) (2018) 3. arXiv:1808.05664, doi:10.3847/1538-4357/aadad9.

[76] J. E. Greene, J. Strader, L. C. Ho, Intermediate-Mass Black Holes, arXiv e-prints (2020) arXiv:1911.09678arXiv:1911.09678.

[77] M. Eracleous, S. Gezari, A. Sesana, T. Bogdanovic, M. MacLeod, N. Roth, L. Dai, An Arena for Multi-Messenger Astrophysics: Inspiral and Tidal Disruption of White Dwarfs by Massive Black Holes, 51 (3) (2019) 10. arXiv:1902.06612.

[78] M. Toscani, G. Lodato, D. J. Price, D. Liptai, Gravitational waves from tidal disruption events: an open and comprehensive catalog, Monthly Notices of the Royal Astronomical Society 510 (1) (2022) 992–1001. doi:10.1093/mnras/stab3384.
URL https://doi.org/10.1093/mnras/stab3384

[79] B. Paxton, L. Bildsten, A. Dotter, F. Herwig, P. Lesaffre, F. Timmes, Modules for experiments in stellar astrophysics (mesa), The Astrophysical Journal Supplement Series 192 (1) (2011) 3. doi:10.1088/0067-0049/192/1/3.
URL https://dx.doi.org/10.1088/0067-0049/192/1/3

Spectroscopic Characterisation of Herbig Ae/Be Stars

Shima Ujjani Shivashankara

University of Nova Gorica, Vipavska 13, SI-5000 Nova Gorica

Abstract

This work presents the spectroscopic study of the stellar parameters and accretion rates of Herbig Ae/Be stars. The discs around solar mass stars are expected to evolve differently compared to those around intermediate mass stars. However, more complete samples of young pre-main sequence stars are not present in literature to quantify the differences. Most current studies in the stellar range of intermediate-mass focuses on the Herbig Ae population, a limited subset of 5-10 Myr old intermediate-mass stars already close to the main sequence. Hence, in this work an unbiased sample of young stars ($<$5 Myr) in the intermediate-mass range, 1.5-3.5 $M_{\odot}$ are selected to be studied. The spectra, optical photometric data and Pre-Main Sequence Evolutionary Tracks are used to find the parameters like effective temperature, surface gravity, extinction, distance, luminosity, radius, mass and age. The absorption and emissionlines present in the spectra are observed to be correlated with accretion luminosity and the accretion rates are determined. It is seen that the younger stars have higher accretion rates compared to the older ones, implying that the accretion rates of the stars decreases as the stars approach the main sequence.

Keywords: stars: Herbig Ae/Be – stars: pre-main sequence – stars: formation – accretion rates – techniques: spectroscopic

1. Introduction

Herbig Ae/Be stars are Pre-Main Sequence (PMS) A-Type or earlier type stars, first identified by George Herbig [1].They have masses intermediate to that of T-Tauri stars and Massive Young Stellar Objects, which lies

Email address: shima.ujjani@ung.si (Shima Ujjani Shivashankara)

in the range of 2 to 10 solar masses. This work focuses on the intermediate-mass Pre-main sequence stars which lie in the mass range of 1.5 - 3.5 solar masses and younger than 5Myr. Herbig stars meet the criteria: "spectral type A or earlier with emission lines, lies in an obscured region, and the star illuminates a fairly bright nebulosity in its immediate vicinity" [1, 2]. The luminosities of these objects range from 10 to 10^3 L_{sun} and their effective temperatures range from 6,000 K - 10,000 K. These stars generally are accompanied by circumstellar disks, which are made of dust and gas, and an Infra-Red (IR) excess can be observed which originates from the dust present around the star [3].

These stars are accreting mass from the inner regions of the disks around them and their accretion rates can be measured. Within the theory of magnetospheric accretion (MA), the accretion rates can be determined from the measured Ultra-Violet (UV) excess [4]. But this theory couldn't be applied to all Herbig stars as all Herbig stars don't have strong magnetic fields. It can only be applied if the strength of the magnetic field of the central star is adequate to truncate the material onto the star [5]. The context of MA is applicable to Classical T-Tauris (CTTs) which have magnetic fields of strengths of the order of 10^3 Gauss [6].

The PMS evolutionary phase for these kinds of stars is less than 10Myr [7]. The material of the disks around these stars gradually reduces in quantity: most of it gets accreted onto the star and some is lost due to photo-evaporation [8]. During the PMS evolutionary phase, the stars' interior is too cold for the fusion reaction to occur and only gravitational energy is acting at this point; the fusion of hydrogen to form helium occurs only when the star reaches the main sequence. It was observed that the main sequence stars have higher surface gravities than the Herbig stars [9]. Surface gravity is the acceleration due to gravity experienced by a hypothetical particle of negligible mass which is located very close to the surface of the star. By calculating the surface gravities of the stars, we can calculate their age, i.e., know their position on the Hertzsprung-Russell (HR) diagram.

A number of works show that the Herbig Ae stars are different from Herbig Be stars, but are similar to T Tauri stars [2]. It was found that the absorption and emission line properties are different for Herbig Ae and Herbig Be stars [10]. T Tauri stars and Herbig Ae stars were found to have similar linear spectropolarimetric properties, but that of Herbig Be stars was found to be different because the strength of magnetic fields is different in both Herbig Ae and Herbig Be stars [11] and, the magnetospheric accretion causes spectroscopic variability in a Herbig Ae star [12].

Spectral classification plays an important role in the study of stars. In general, PMS A-type stars have the effective temperature of 7,500 - 10,000K. The Morgan - Keenan (MK) system subdivides these stars into ten classes of spectral type, A0 to A9, A0 being the hottest and A9 the coolest. These stars have strong Balmer lines accompanied by many faint to moderately strong metallic lines, whose strength gradually increases from A0 to A9. Hydrogen has its maximum strength at A2 and decreases from there.

The spectral type determination will help us gather information about the total extinction due to the dust, the type of the star, and the components of the dust. Many of the stars show large extinction due to the presence of dust in the star formation region and the presence of significant amounts of dust in the disk around the star [13]. The spectra of these stars show some peculiarities, like the excess emission in the infrared region, which provides an evidence for the presence of the disks around them [8], and the presence of strong emission at hydrogen alpha lines showing that the star is still accreting [14]. The broadening of the absorption lines of the Herbig Ae stars yields the rotational speeds [15].

This work focuses on the study of Herbig Ae stars younger than 5Myr and in the mass range 1.5-3.5 solar masses. The frequency of formation of giant planets is the highest around stars of mass around $2M_{\odot}$ [16, 17], and around stars above $1.5M_{\odot}$ the orbits of giant planets are larger than 1 au [18]. This gives us information about the dispersal of the protoplanetary disc around the stars; giant planets can only form and migrate in presence of dense gas [19, 20]. A hypothesis was stated by Kennedy & Kenyon 2008 that faster clearing of the inner disc due to photoevaporation around intermediate-mass stars might halt the migrating giant planets before they reach smaller orbital distances and such planets are found around low mass stars. This tells us that low mass and intermediate-mass stars evolve differently on the pre-main sequence. Intermediate-mass stars are more luminous and their photoevaporation is driven by FUV photons, unlike X-rays in case of low-mass stars [21]. The thermal and chemical evolution of the discs are also different due to the large luminosities [22]. This work deals with measuring the stellar parameters and mass accretion rates to check how intermediate mass star evolves.

2. Observations and Data Reduction

The sample was collected using the Tycho-GAIA Astrometric Solution catalogue and Hipparcos catalogue, by keeping the declination between -78° and $+30^{\circ}$, and across all right ascension. First the stars with precise

B and V photometry were selected. Next only stars with measured excess levels $F_{total}/F_{midIR} \geq 1$ were considered. This limit corresponds to debris disc level of excess at 20μm [19], and therefore we do not expect detectable signatures of accretion with XShooter below this level.

Further the stars were selected based on their location on the HR diagram, keeping stars which may be of age $\leq$ 5 Myr and in the mass range 1.5-3.5 $M_{\odot}$. There are studies in the literature about pre-main sequence stars to see how the solar mass and intermediate-mass stars evolve. However, more complete samples of young pre-main sequence stars are not present to quantify the difference as there is no unbiased statistical sample of pre-main sequence stars in the intermediate-mass stellar range in the literature. Most current studies in the stellar range of intermediate-mass focus on the Herbig Ae population, a limited subset of 5-10 Myr old intermediate-mass stars already close to the main sequence. Hence, in this work an unbiased sample of young stars ($<$ 5 Myr) in the intermediate-mass range, 1.5-3.5 $M_{\odot}$ are studied. The UVB, optical and near-IR spectra of about 200 pre-main sequence candidate stars are obtained, out of which a subset of 18 stars are found to be accreting. This was determined by checking for emission at hydrogen alpha (H_{α}) line of the Balmer series; only stars which are accreting will have an emission at H_{α} line. Also, 27 targets were excluded from the observed sample as their data was already present in the ESO archive. The data was automatically reduced by the ESO pipeline and were checked by one of the collaborators, Dr. Mario van den Ancker at ESO.

3. Determining the stellar parameters

X-Shooter provides spectra covering a large wavelength range, from the ultraviolet (UV) to the near-infrared (NIR), taken simultaneously across the three arms: the UVB arm (3000-5600 Å), the VIS arm (5600-10200 Å) and the NIR arm (10200-24800 Å) [23]. Each of the three arms is an individual echelle spectrograph, which disperses the incident beam of light in the form of a spectrum. The spectra were obtained with S/N $>$ 100 over the entire wavelength range (3600-24800 Å) for each target in the sample.

The hydrogen Balmer lines are sensitive to changes in both T_{eff} and log(g). Since emission can be seen in the core, the wings of these lines are used to perform spectral typing. Among the hydrogen Balmer lines, H_{α} is the strongest and broadest of the series for Herbig stars and they often exhibit emission and can affect the parameters derived. Hence, H_{β}, H_{γ} and H_{δ} lines are used to determine T_{eff} and log(g) for the targets. The

BOSZ model [24] is used to perform the spectral fitting. To compare the lines from the spectra of the stars, the same lines from the model are also normalised based on the continuum on both the sides of the line in the same wavelength region. This normalisation is done using IRAF (Image Reduction and Analysis Facility) software. The comparison of the observed spectra to that of the model is done by over-plotting the lines and setting the T_{eff} to increase in steps of 250K and of log(g) to increase in steps of 0.5 cms^{-2}. The best fit is chosen based on the wings on both sides of the lines where intensity is greater than 0.8, to avoid any effect of emission and rotational broadening of the line, which affects the central parts of the absorption lines. The best fit is chosen by visually comparing the fits.

By performing the fitting of the spectra of the model (based on the obtained temperature), with the observed optical photometry (taken from literature), the interstellar reddening A_V, and the scaling factor D/R_*, which is the ratio of the distance of the star to its radius (from Earth), can be determined. The scaling factor is a result of fitting the the observed photometric data with the model [24]. To perform the fitting, the B, V, and R points, at 4400 Å, 5500 Å and 6400 Å, are used in this work. Photometry of the I band can also be used, but for the list of targets worked on in this project the photometry at I band was not available in literature, hence only B, V and R bands are used. The Balmer excess can have an influence on the U band and hence it is a better option not to consider that to perform fitting. In this work, the photometry is assumed to be mainly photospheric and the effect for variability is low. The photometric values with maximum brightness are chosen, in case there are many photometric values.

The radius can be determined from the scaling factor, since the distance is already known. Once the temperature (T_{eff}) and radius (R_*) is known, the luminosity of the star can be calculated, as $L_* = 4\pi R_*^2 \sigma T_{eff}^4$. The errors in both T_{eff} and R_* are used to compute the errors in the calculation of luminosity, which will then be used to calculate the errors in the other parameters. The Lionel-Siess Pre-Main Sequence (PMS) Evolutionary Tracks [25] are used to determine the other parameters. Each evolutionary track denotes a fixed mass, showing how a star would contract and evolve over time, changing its temperature and luminosity. The change in these parameters results in a change in mass, radius and age as well. The metallicity is kept Z=0.01 for all the targets in this work. The temperature (in K) and luminosity (in $L_\odot$) are entered. The radius, mass and age of the stars are determined. Table 1 shows the obtained stellar parameters for all the targets.

Table 1: Table showing the effective temperature, surface gravity, distance, reddening, luminosity, mass, radius and age of all the targets.

Name	$\mathbf{T}_{eff}$ (K)	**log(g)** (cm/s^2)	**D** (pc)	$\mathbf{A}_V$ (mag)	**log($L_\star$)** [$L_\odot$]	$\mathbf{M}_\star$ ($M_\odot$)	$\mathbf{R}_\star$ ($R_\odot$)	**Age** (Myr)
HIP 22112	14500^{+500}_{-500}	$4.0^{+0.50}_{-0.50}$	$603.50^{+19.23}_{-19.23}$	$1.17^{+0.06}_{-0.08}$	$2.99^{+0.12}_{-0.13}$	$5.04^{+0.01}_{-0.08}$	$4.96^{+0.35}_{-0.38}$	$0.40^{+0.01}_{-0.00}$
HIP 23201	13000^{+500}_{-500}	$4.0^{+0.00}_{-0.50}$	$266.40^{+4.18}_{-4.18}$	$1.22^{+0.07}_{-0.06}$	$2.24^{+0.12}_{-0.11}$	$3.49^{+0.12}_{-0.07}$	$2.61^{+0.15}_{-0.13}$	$1.66^{+0.02}_{-0.03}$
HIP 25763	6250^{+500}_{-250}	$4.5^{+0.50}_{-0.00}$	$194.73^{+2.38}_{-2.38}$	$0.43^{+0.05}_{-0.06}$	$0.91^{+0.17}_{-0.11}$	$1.60^{+0.03}_{-0.02}$	$2.44^{+0.10}_{-0.10}$	$7.44^{+0.24}_{-0.64}$
HIP 28561	11750^{+750}_{-000}	$4.0^{+0.50}_{-0.00}$	$266.84^{+9.54}_{-9.54}$	$0.06^{+0.05}_{-0.04}$	$2.47^{+0.16}_{-0.05}$	$3.99^{+0.02}_{-0.01}$	$4.16^{+0.27}_{-0.24}$	$1.42^{+0.38}_{-0.51}$
HIP 29635	11000^{+500}_{-500}	$3.5^{+0.00}_{-0.00}$	$269.63^{+4.79}_{-4.79}$	$0.11^{+0.04}_{-0.04}$	$2.35^{+0.11}_{-0.11}$	$3.56^{+0.04}_{-0.02}$	$4.10^{+0.17}_{-0.17}$	$1.14^{+0.06}_{-0.03}$
HIP 30448	11750^{+250}_{-250}	$3.5^{+0.50}_{-0.00}$	$262.59^{+6.78}_{-6.78}$	$0.07^{+0.04}_{-0.06}$	$2.51^{+0.08}_{-0.09}$	$4.04^{+0.02}_{-0.01}$	$4.37^{+0.22}_{-0.26}$	$0.87^{+0.02}_{-0.00}$
HIP 38779	11750^{+000}_{-500}	$3.5^{+0.00}_{-0.50}$	$673.67^{+0.00}_{-0.00}$	$0.23^{+0.04}_{-0.05}$	$3.19^{+0.02}_{-0.10}$	$6.73^{+0.13}_{-0.14}$	$9.53^{+0.22}_{-0.29}$	$0.20^{+0.01}_{-0.00}$
HIP 48613	9500^{+500}_{-500}	$4.0^{+0.00}_{-0.50}$	$99.34^{+0.91}_{-0.91}$	$0.08^{+0.02}_{-0.03}$	$1.70^{+0.09}_{-0.12}$	$2.46^{+0.04}_{-0.15}$	$2.61^{+0.05}_{-0.07}$	$3.45^{+0.13}_{-0.06}$
HIP 57027	6750^{+250}_{-250}	$4.5^{+0.50}_{-0.00}$	$104.91^{+4.15}_{-4.15}$	$0.00^{+0.21}_{-0.00}$	$1.07^{+0.29}_{-0.37}$	$1.67^{+0.23}_{-0.18}$	$2.50^{+0.74}_{-0.75}$	$7.39^{+3.68}_{-2.41}$
HIP 57143	14000^{+500}_{-500}	$4.0^{+0.50}_{-0.50}$	$422.71^{+12.08}_{-12.08}$	$0.45^{+0.05}_{-0.05}$	$2.89^{+0.11}_{-0.11}$	$5.03^{+0.02}_{-0.83}$	$4.72^{+0.29}_{-0.27}$	$0.52^{+0.07}_{-0.08}$
HIP 61738	13000^{+500}_{-500}	$4.0^{+0.00}_{-0.00}$	$174.52^{+2.35}_{-2.35}$	$0.64^{+0.00}_{-0.00}$	$2.38^{+0.08}_{-0.08}$	$3.68^{+0.19}_{-0.22}$	$3.05^{+0.04}_{-0.04}$	$1.50^{+0.05}_{-0.30}$
HIP 74911	12000^{+1000}_{-250}	$4.0^{+0.50}_{-0.00}$	$102.88^{+0.00}_{-0.00}$	$0.08^{+0.01}_{-0.00}$	$2.22^{+0.14}_{-0.04}$	$3.32^{+0.23}_{-0.01}$	$2.97^{+0.02}_{-0.00}$	$1.62^{+0.02}_{-0.09}$
HIP 77289	12500^{+500}_{-750}	$3.5^{+0.50}_{-0.50}$	$389.70^{+20.04}_{-20.04}$	$0.14^{+0.04}_{-0.05}$	$2.60^{+0.13}_{-0.18}$	$4.01^{+0.18}_{-0.03}$	$4.27^{+0.33}_{-1.07}$	$0.69^{+0.18}_{-0.01}$
HIP 81710	14000^{+1000}_{-500}	$4.0^{+0.00}_{-0.00}$	$234.31^{+4.26}_{-4.26}$	$0.09^{+0.04}_{-0.04}$	$2.73^{+0.16}_{-0.10}$	$4.10^{+0.34}_{-0.00}$	$3.94^{+0.17}_{-0.17}$	$0.67^{+0.01}_{-0.02}$
HIP 92364	10750^{+250}_{-250}	$3.5^{+0.50}_{-0.00}$	$270.52^{+4.08}_{-4.08}$	$0.98^{+0.07}_{-0.08}$	$2.02^{+0.09}_{-0.10}$	$2.96^{+0.01}_{-0.03}$	$2.95^{+0.17}_{-0.18}$	$2.25^{+0.03}_{-0.02}$
HIP 94260	9500^{+500}_{-250}	$4.0^{+0.50}_{-0.00}$	$265.99^{+3.30}_{-3.30}$	$0.30^{+0.03}_{-0.03}$	$1.97^{+0.12}_{-0.07}$	$2.74^{+0.16}_{-0.00}$	$3.55^{+0.11}_{-0.10}$	$2.14^{+0.02}_{-0.06}$
TYC-461-622-1	6250^{+000}_{-250}	$4.0^{+0.50}_{-0.00}$	$149.63^{+1.88}_{-1.88}$	$0.42^{+0.06}_{-0.06}$	$0.50^{+0.04}_{-0.11}$	$1.23^{+0.01}_{-0.03}$	$1.52^{+0.07}_{-0.06}$	$15.71^{+0.87}_{-0.97}$
TYC-9329-60-1	6500^{+250}_{-250}	$4.0^{+0.50}_{-0.00}$	$272.98^{+2.18}_{-2.18}$	$0.29^{+0.03}_{-0.03}$	$0.94^{+0.08}_{-0.09}$	$1.56^{+0.04}_{-0.02}$	$2.34^{+0.06}_{-0.06}$	$8.50^{+0.17}_{-0.33}$

4. Accretion Rate Measurements

Herbig stars are found to be similar to the Classical T Tauri stars (CTTs), as they have similar properties like the presence of discs around them, presence of emission lines, both have lower surface gravities than main sequence (MS) stars and both exhibit UV excess. Accretion plays an important role in influencing the mass of the planets formed within the discs as the newly forming planets need to feed on the disc material. Accretion is also a source of energy for the emission lines and the UV excess observed in their spectra [26, 27, 28].

PMS stars accrete material from their disks for a very long time until the material in the disc is accreted entirely onto the star or removed due to planet formation or photoevaporation. The accretion rates of Herbig Ae stars are low and was found to be about $10^{-9} < \dot{M}_{acc} < 10^{-6}\ M_{\odot}/\mathrm{yr}$ [29]. The inner rim of the disc receives direct stellar radiation and a puffed-up rim is formed [30, 31, 32, 33].

The accretion rates of the stars can be determined using the emission lines seen in their spectra. It has been found that the accretion luminosity is correlated to the luminosities of the emission lines of the stars [34, 35, 36, 37, 38]. Details like the motion of the gases and the geometry of the emitting regions can be provided by the various profiles of the spectral lines. For example, the presence of double peaked lines in emission signifies that the disc is rotating [39, 40, 41]. It is also seen that a few luminosity relationships which holds good for CTTs also holds good for Herbig stars [28]. Hence the line profiles can be used to determine the accretion rates of the stars. It is easier to obtain the emission line measurements than to obtain the UV excess measurements to determine the accretion rates ($\dot{M}_{acc}$), as emission lines at a variety of different wavelengths can be used for measurements.

The stellar parameters, like T_{eff}, log(g), A_V, L_*, R_*, M_* and age, were determined in the previous section for the sample of 18 stars. These parameters are used to determine the accretion rates of the stars. First, the equivalent width (EW) of the Hydrogen-alpha (H_α) emission line of the Balmer series is determined, from which the line flux is calculated. Using this the line luminosity is determined and then the accretion rate is calculated.

The strength of each observed emission line is calculated by measuring the Equivalent Width (EW) and is shown in the expression below:

$$EW = \int_a^b \frac{I_c - I_\lambda}{I_c},$$

where a and b are the blue and red wavelength points respectively, I_c is

the continuum intensity and I_λ is the intensity of the line at a particular wavelength. The line was normalised such that the continuum level is at unity. To determine the EW of the H_α emission line of the Balmer series, the spectra of the stars obtained by X-Shooter is used along-with the spectra of the Bosz model. To achieve this, the H_α emission line of the spectra was normalised using IRAF based on the continuum region on both the sides. The EW is measured for this normalised line using IRAF and is called as observed equivalent width, EW_{obs}.

There will be some intrinsic absorption of the line in the majority of the observed emission lines of the observed spectra due to the stellar photosphere. EW_{obs} is a combination of the intrinsic absorption and true circumstellar emission, and the true emission is stronger than the corrected equivalent width, EW_{corr}. The intrinsic equivalent width must be subtracted from the observed to obtain EW_{corr}. Hence, it is necessary to determine the EW of the intrinsic absorption line, EW_{int}. This is done using the model spectra.

The strength of the intrinsic absorption line depends on the temperature, surface gravity, and metallicity of the star, which are all determined in the previous section. The model spectrum corresponding to the temperature obtained for each individual star is used to find EW_{int}. To determine EW_{int}, the H_α absorption line of the spectra is normalised based on the same continuum regions, as chosen for the observed spectra, on either side of the line. The normalisation is done using IRAF and also the EW is measured using the same. Once EW_{obs} and EW_{int} is known, the corrected Equivalent Width, EW_{corr}, is determined using the relation:

$$EW_{corr} = EW_{obs} - EW_{int}.$$

The line flux, F_{line}, can be calculated with the known value of EW_{corr}, using the following expression:

$$F_{line} = \mid EW_{corr} \mid \times F_\lambda,$$

where F_λ is the continuum flux corresponding to the central wavelength of the line.

The line luminosity, L_{line}, of the emission line can be determined as the distance of the stars are known, as:

$$L_{line} = 4\pi D^2 F_{line}.$$

The calculated values of EW_{obs}, EW_{int}, EW_{corr}, F_λ, F_{line} and L_{line} will

now be used to determine the accretion luminosity, L_{acc}, and accretion rate $\dot{M}_{acc}$ of the stars.

Even though many different lines can be used for measuring accretion rates, the most commonly used are H_α, Paβ, Brγ and $[OI]_{\lambda 6300}$; H_α is used in this work. These lines are frequently used as their luminosity and accretion luminosity are correlated [42, 36, 35, 28, 34] as shown below:

$$log\left(\frac{L_{acc}}{L_\odot}\right) = A + B \times log\left(\frac{L_{line}}{L_\odot}\right),$$

where A and B are constants, which are different for different lines. The values of A and B obtained by [8] is (2.09 ± 0.06) and (1.00 ± 0.05) respectively, which is used in this work. This approach of measuring the accretion rates from accretion luminosity is more effective than from UV excess as hot stars with low accretion rates cannot be detected easily by a UV excess.

The accretion rate, $\dot{M}_{acc}$, can now be calculated using the relation:

$$L_{acc} = \frac{GM_*}{R_*}\dot{M}_{acc},$$

where L_{acc} is the accretion luminosity, G is the gravitational constant, M_* is the mass of the star and R_* is the radius of the star. Table 2 shows the determined accretion rates for the sample.

5. Results and Discussion

Figure 1 shows how the accretion rate varies with age. The stars with mass lower than 1.5 $M_\odot$ is shown in blue dots, the stars in the mass range 1.5-3.5 $M_\odot$ are shown in orange dots and the stars massive than 3.5 $M_\odot$ are shown in green dots. It is seen in the plot that the younger stars have high accretion rates compared to the older stars, i.e., the accretion rate diminishes as the star grows older. This indicates that the accretion rate tells us how the Herbig stars evolve. When the stars are young, the discs around them have more material which is accreted onto the star. Gradually, the material of the disc is lost as it is accreted onto the stars or lost due to photoevaporation or due to planet formation [21].

In this work, the relation between the accretion rate and age is determined as $\dot{M}_{acc} \propto t^{-2.10\pm0.30}$. A fit to the data that provides a relationship between the accretion rate and age as $\dot{M}_{acc} \propto t^{-\eta}$, where t is the age in Myr, obtained by [43] is $\eta = 1.92 \pm 0.09$. This relationship is seen to vary for Herbig Ae (HAes) and Herbig Be (HBes) stars. For HBes, η is found to be 2.02 ± 0.22, which is similar to the results for all Herbig stars, but HAes was

Table 2: Table showing the corrected equivalent width, line luminosity, accretion luminosity and accretion rates of all the targets.

Name	**EW**$_{corr}$ (Å)	**log(L**$_{line}$**)** ($L_\odot$)	**log(L**$_{acc}$**)** ($L_\odot$)	**log($\dot{M}_{acc}$)** [$M_\odot/yr$]
HIP 22112	-13.88 ±0.40	$-0.43^{+0.03}_{-0.04}$	$1.66^{+0.03}_{-0.04}$	$-5.85^{+0.04}_{-0.08}$
HIP 23201	-10.82 ±0.23	$-1.17^{+0.03}_{-0.03}$	$0.92^{+0.04}_{-0.03}$	$-6.73^{+0.04}_{-0.04}$
HIP 25763	0.31 ±0.10	$-3.56^{+0.02}_{-0.03}$	$-1.47^{+0.02}_{-0.03}$	$-8.81^{+0.02}_{-0.04}$
HIP 28561	-12.68 ±0.97	$-0.77^{+0.02}_{-0.02}$	$1.32^{+0.02}_{-0.02}$	$-6.13^{+0.01}_{-0.08}$
HIP 29635	-9.27 ±0.16	$-0.97^{+0.02}_{-0.02}$	$1.12^{+0.02}_{-0.02}$	$-6.32^{+0.06}_{-0.03}$
HIP 30448	-10.04 ±0.27	$-0.83^{+0.02}_{-0.03}$	$1.26^{+0.02}_{-0.03}$	$-6.20^{+0.02}_{-0.05}$
HIP 38779	-8.16 ±0.17	$-0.24^{+0.02}_{-0.03}$	$1.85^{+0.02}_{-0.03}$	$-5.50^{+0.06}_{-0.02}$
HIP 48613	0.22 ±0.05	$-3.12^{+0.01}_{-0.02}$	$-1.03^{+0.01}_{-0.02}$	$-8.44^{+0.05}_{-0.11}$
HIP 57027	-0.05 ±0.15	$-4.23^{+0.19}_{-0.27}$	$-2.14^{+0.19}_{-0.27}$	$-9.49^{+0.23}_{-0.35}$
HIP 57143	-15.09 ±1.35	$-0.46^{+0.03}_{-0.02}$	$1.63^{+0.03}_{-0.02}$	$-5.91^{+0.06}_{-0.09}$
HIP 61738	-16.32 ±1.21	$-0.86^{+0.00}_{-0.00}$	$1.22^{+0.00}_{-0.00}$	$-6.38^{+0.01}_{-0.04}$
HIP 74911	-9.13 ±0.96	$-1.19^{+0.01}_{-0.00}$	$0.90^{+0.01}_{-0.00}$	$-6.72^{+0.01}_{-0.04}$
HIP 77289	-19.50 ±0.58	$-0.51^{+0.02}_{-0.03}$	$1.58^{+0.02}_{-0.03}$	$-5.91^{+0.05}_{-0.10}$
HIP 81710	-14.32 ±0.87	$-0.64^{+0.02}_{-0.02}$	$1.45^{+0.02}_{-0.02}$	$-6.23^{+0.08}_{-0.04}$
HIP 92364	-8.12 ±0.77	$-1.34^{+0.03}_{-0.04}$	$0.75^{+0.03}_{-0.04}$	$-6.69^{+0.04}_{-0.03}$
HIP 94260	-9.80 ±1.09	$-1.20^{+0.02}_{-0.01}$	$0.89^{+0.02}_{-0.01}$	$-6.51^{+0.07}_{-0.04}$
TYC-461-622-1	-0.29 ±0.50	$-3.99^{+0.03}_{-0.03}$	$-1.91^{+0.03}_{-0.03}$	$-9.36^{+0.05}_{-0.04}$
TYC-9329-60-1	-0.06 ±0.87	$-4.28^{+0.01}_{-0.02}$	$-2.19^{+0.01}_{-0.02}$	$-9.54^{+0.02}_{-0.03}$

found to have a steeper relationship with $\eta = 4.06 \pm 0.53$ [43]. A more general relationship for all Herbig stars as η = 1.8 [44]. Classical T Tauri stars (CTTs) are also seen to follow the same trend in the relationship between the age and the accretion rates of the stars and η is found to be in the range 1.5-2.8 [45]. But, recent studies have shown that there is a difference in the relationship $\dot{M}_{acc} \propto t^{-\eta}$ for Herbig stars and CTTs, as the relationship was found to be shallower, $\dot{M}_{acc} \propto t^{-2}$ [46, 47]. This implies that massive stars have high accretion rates and are only observable at their younger ages

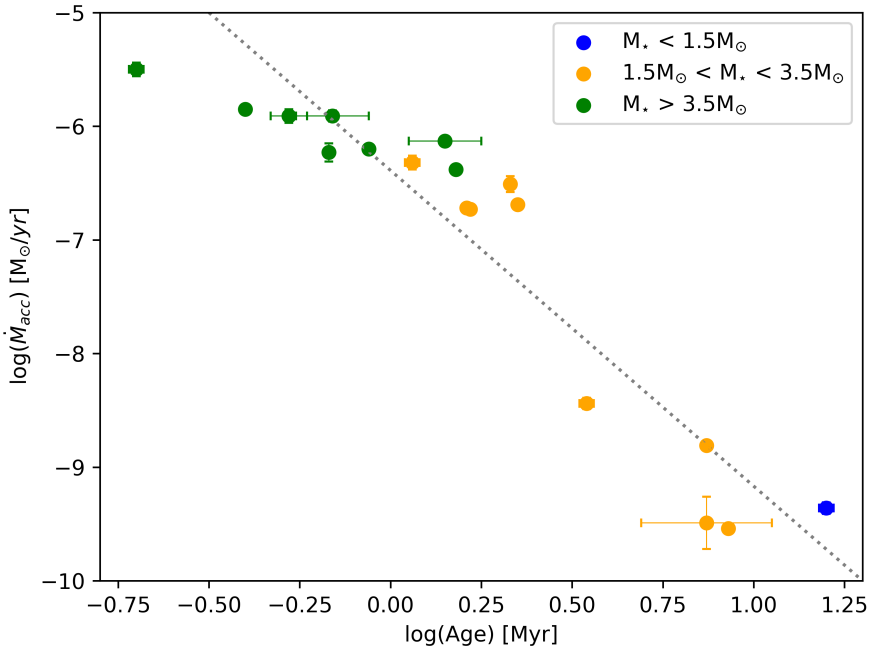

Figure 1: Plot showing the accretion rates of the stars plotted against their ages; stars with masses lower than 1.5 $M_\odot$ are shown in blue dots, stars in the mass range 1.5-3.5 $M_\odot$ are shown in orange dots and those with masses greater than 3.5 $M_\odot$ are shown in green dots.

as they evolve quicker and the less massive stars have a longer Pre-Main Sequence lifetime.

References

[1] G. H. Herbig. The Spectra of Be- and Ae-Type Stars Associated with Nebulosity. , 4:337, March 1960.

[2] R. D. Oudmaijer, K. M. Ababakr, and J. R. Fairlamb. The formation and evolution of Herbig Ae/Be stars . , 88:605, Jan 2017.

[3] M. E. van den Ancker, J. Bouwman, P. R. Wesselius, L. B. F. M. Waters, S. M. Dougherty, and E. F. van Dishoeck. ISO spectroscopy of circumstellar dust in the Herbig Ae systems AB Aur and HD 163296. , 357:325–329, May 2000.

[4] James Muzerolle, Paola D'Alessio, Nuria Calvet, and Lee Hartmann. Magnetospheres and Disk Accretion in Herbig Ae/Be Stars. , 617(1):406–417, Dec 2004.

[5] Frank Shu, Joan Najita, Eve Ostriker, Frank Wilkin, Steven Ruden, and Susana Lizano. Magnetocentrifugally Driven Flows from Young Stars and Disks. I. A Generalized Model. , 429:781, Jul 1994.

[6] J. Bouvier, S. H. P. Alencar, T. J. Harries, C. M. Johns-Krull, and M. M. Romanova. Magnetospheric Accretion in Classical T Tauri Stars. In Bo Reipurth, David Jewitt, and Klaus Keil, editors, *Protostars and Planets V*, page 479, Jan 2007.

[7] Alessandro Bressan, Paola Marigo, Léo. Girardi, Bernardo Salasnich, Claudia Dal Cero, Stefano Rubele, and Ambra Nanni. PARSEC: stellar tracks and isochrones with the PAdova and TRieste Stellar Evolution Code. , 427(1):127–145, Nov 2012.

[8] J. R. Fairlamb, R. D. Oudmaijer, I. Mendigutia, J. D. Ilee, and M. E. van den Ancker. A spectroscopic survey of Herbig Ae/Be stars with X-Shooter - II. Accretion diagnostic lines. , 464(4):4721–4735, Feb 2017.

[9] S. E. Strom, K. M. Strom, J. Yost, L. Carrasco, and G. Grasdalen. The Nature of the Herbig Ae- and Be-TYPE Stars Associated with Nebulosity. , 173:353, April 1972.

[10] P. Wilson Cauley and Christopher M. Johns-Krull. Optical Mass Flow Diagnostics in Herbig Ae/Be Stars. , 810(1):5, Sep 2015.

[11] Jorick S. Vink, Janet E. Drew, Tim J. Harries, René D. Oudmaijer, and Yvonne Unruh. Probing the circumstellar structures of T Tauri stars and their relationship to those of Herbig stars. , 359(3):1049–1064, May 2005.

[12] Silva P. Järvinen, Markus Schöller, Michail A. Pogodin, Andres Cahuasqui, Natalia A. Drake, S. Hubrig, Monika Petr-Gotzens, Igor S. Savanov, Ilya Ilyin, and Beate Stelzer. Spectroscopic Signatures Of Magnetospheric Accretion In Herbig Ae/Be Stars. In *19th Cambridge Workshop on Cool Stars, Stellar Systems, and the Sun (CS19)*, Cambridge Workshop on Cool Stars, Stellar Systems, and the Sun, page 74, Jul 2016.

[13] F. Palla and S. W. Stahler. The formation and evolution of Herbig Ae/Be stars. In P. S. The, M. R. Perez, and E. P. J. van den Heuvel, editors, *The Nature and Evolutionary Status of Herbig Ae/Be Stars*, volume 62 of *Astronomical Society of the Pacific Conference Series*, page 391, 1994.

[14] S. Kraus, K. H. Hofmann, M. Benisty, J. P. Berger, O. Chesneau, A. Isella, F. Malbet, A. Meilland, N. Nardetto, A. Natta, T. Preibisch, D. Schertl, M. Smith, P. Stee, E. Tatulli, L. Testi, and G. Weigelt. The origin of hydrogen line emission for five Herbig Ae/Be stars spatially resolved by VLTI/AMBER spectro-interferometry. , 489(3):1157–1173, Oct 2008.

[15] G. van der Plas, M. E. van den Ancker, L. B. F. M. Waters, and C. Dominik. The structure of disks around Herbig Ae/Be stars as traced by CO ro-vibrational emission. , 574:A75, Feb 2015.

[16] Sabine Reffert, Christoph Bergmann, Andreas Quirrenbach, Trifon Trifonov, and Andreas Künstler. Giant Planet Occurrence Rate as a Function of Stellar Mass. In *Protostars and Planets VI Posters*, Jul 2013.

[17] Andreas Quirrenbach, Sabine Reffert, Trifon Trifonov, Christoph Bergmann, and Christian Schwab. Planets around Giant Stars: Results from the Lick Survey. In *AAS/Division for Extreme Solar Systems Abstracts*, volume 47 of *AAS/Division for Extreme Solar Systems Abstracts*, page 502.01, Dec 2015.

[18] B. Sato, H. Izumiura, E. Toyota, E. Kambe, M. Ikoma, M. Omiya, S. Masuda, Y. Takeda, D. Murata, Y. Itoh, H. Ando, M. Yoshida, E. Kokubo, and S. Ida. *Properties of Planets around G, K Giants*, volume 398 of *Astronomical Society of the Pacific Conference Series*, page 67. 2008.

[19] Richard P. Nelson and John C. B. Papaloizou. The interaction of giant planets with a disc with MHD turbulence - IV. Migration rates of embedded protoplanets. , 350(3):849–864, May 2004.

[20] John C. B. Papaloizou, Richard P. Nelson, and Mark D. Snellgrove. The interaction of giant planets with a disc with MHD turbulence - III. Flow morphology and conditions for gap formation in local and global simulations. , 350(3):829–848, May 2004.

[21] U. Gorti and D. Hollenbach. Photoevaporation of Circumstellar Disks By Far-Ultraviolet, Extreme-Ultraviolet and X-Ray Radiation from the Central Star. , 690(2):1539–1552, Jan 2009.

[22] O. Panić and M. Min. Effects of disc mid-plane evolution on CO snow-line location. , 467(1):1175–1185, May 2017.

[23] J. Vernet, H. Dekker, S. D'Odorico, L. Kaper, P. Kjaergaard, F. Hammer, S. Randich, F. Zerbi, P. J. Groot, and J. Hjorth. X-shooter, the new wide band intermediate resolution spectrograph at the ESO Very Large Telescope. , 536:A105, Dec 2011.

[24] Ralph C. Bohlin, Szabolcs Mészáros, Scott W. Fleming, Karl D. Gordon, Anton M. Koekemoer, and József Kovács. A New Stellar Atmosphere Grid and Comparisons with HST/STIS CALSPEC Flux Distributions. , 153(5):234, May 2017.

[25] L. Siess, M. Forestini, and C. Dougados. Synthetic Hertzsprung-Russell diagrams of open clusters. , 324:556–565, Aug 1997.

[26] L. M. Garrison, Jr. Observational studies of the Herbig Ae/Be stars. III - Spectrophotometry. , 224:535–545, September 1978.

[27] Brian Donehew and Sean Brittain. Measuring the Stellar Accretion Rates of Herbig Ae/Be Stars. , 141(2):46, Feb 2011.

[28] I. Mendigutía, N. Calvet, B. Montesinos, A. Mora, J. Muzerolle, C. Eiroa, R. D. Oudmaijer, and B. Merín. Accretion rates and accretion tracers of Herbig Ae/Be stars. , 535:A99, Nov 2011.

[29] R. Garcia Lopez, A. Natta, L. Testi, and E. Habart. Accretion rates in Herbig Ae stars. , 459(3):837–842, Dec 2006.

[30] C. Dominik, C. P. Dullemond, L. B. F. M. Waters, and A. Natta. *Models of Passive Disks with Inner Holes: Evidence for Disks around Intermediate Mass Pre-Main-Sequence Stars*, volume 287 of *Astronomical Society of the Pacific Conference Series*, pages 313–318. 2003.

[31] M. Benisty, A. Natta, A. Isella, J. P. Berger, F. Massi, J. B. Le Bouquin, A. Mérand, G. Duvert, S. Kraus, F. Malbet, J. Olofsson, S. Robbe-Dubois, L. Testi, M. Vannier, and G. Weigelt. Strong near-infrared emission in the sub-AU disk of the Herbig Ae star HD 163296: evidence of refractory dust? , 511:A74, Feb 2010.

[32] Andrea Isella, Antonella Natta, and Leonardo Testi. The Shape of the Inner Rim in Proto-Planetary Disks. In A. Richichi, F. Delplancke, F. Paresce, and A. Chelli, editors, *The Power of Optical/IR Interferometry: Recent Scientific Results and 2nd Generation*, page 515, Jan 2008.

[33] C. P. Dullemond, C. Dominik, and A. Natta. Passive Irradiated Circumstellar Disks with an Inner Hole. , 560(2):957–969, Oct 2001.

[34] E. Rigliaco, A. Natta, L. Testi, S. Randich, J. M. Alcalà, E. Covino, and B. Stelzer. X-shooter spectroscopy of young stellar objects. I. Mass accretion rates of low-mass T Tauri stars in σ Orionis. , 548:A56, December 2012.

[35] Gregory J. Herczeg and Lynne A. Hillenbrand. UV Excess Measures of Accretion onto Young Very Low Mass Stars and Brown Dwarfs. , 681(1):594–625, Jul 2008.

[36] S. E. Dahm. A Spectroscopic Examination of Accretion Diagnostics for Near Solar Mass Stars in IC 348. , 136(2):521–547, Aug 2008.

[37] Nuria Calvet, James Muzerolle, César Briceño, Jesus Hernández, Lee Hartmann, José Luis Saucedo, and Karl D. Gordon. The Mass Accretion Rates of Intermediate-Mass T Tauri Stars. , 128(3):1294–1318, Sep 2004.

[38] J. Muzerolle, L. Hartmann, and N. Calvet. Emission-Line Diagnostics of T Tauri Magnetospheric Accretion. I. Line Profile Observations. , 116:455–468, July 1998.

[39] B. Acke, M. E. van den Ancker, and C. P. Dullemond. [O I] 6300 Å emission in Herbig Ae/Be systems: Signature of Keplerian rotation. , 436:209–230, June 2005.

[40] B. Acke and M. E. van den Ancker. Resolving the disk rotation of HD 97048 and HD 100546 in the [O I] 6300 Å line: evidence for a giant planet orbiting HD 100546. , 449(1):267–279, Apr 2006.

[41] T. Bagnoli, R. van Lieshout, L. B. F. M. Waters, G. van der Plas, B. Acke, H. van Winckel, G. Raskin, and P. D. Meerburg. An Inner Gaseous Disk Around the Herbig Be Star MWC 147. , 724:L5–L8, November 2010.

[42] Charles J. Lada. Star formation: from OB associations to protostars. In Manuel Peimbert and Jun Jugaku, editors, *Star Forming Regions*, volume 115 of *IAU Symposium*, page 1, Jan 1987.

[43] J. R. Fairlamb, R. D. Oudmaijer, I. Mendigutía, J. D. Ilee, and M. E. van den Ancker. A spectroscopic survey of Herbig Ae/Be stars with X-shooter - I. Stellar parameters and accretion rates. , 453(1):976–1001, Oct 2015.

[44] I. Mendigutía, A. Mora, B. Montesinos, C. Eiroa, G. Meeus, B. Merín, and R. D. Oudmaijer. Accretion-related properties of Herbig Ae/Be stars. Comparison with T Tauris. , 543:A59, July 2012.

[45] Lee Hartmann, Nuria Calvet, Erik Gullbring, and Paola D'Alessio. Accretion and the Evolution of T Tauri Disks. , 495(1):385–400, Mar 1998.

[46] Aurora Sicilia-Aguilar, Thomas Henning, and Lee W. Hartmann. Accretion in Evolved and Transitional Disks in CEP OB2: Looking for the Origin of the Inner Holes. , 710(1):597–612, Feb 2010.

[47] A. Caratti o Garatti, R. Garcia Lopez, S. Antoniucci, B. Nisini, T. Giannini, J. Eislöffel, T. P. Ray, D. Lorenzetti, and S. Cabrit. POISSON project. II. A multi-wavelength spectroscopic and photometric survey of young protostars in L 1641. , 538:A64, Feb 2012.

Fabrication of WO_3-carbon composite on different substrates for improved electrochemical performance of pseudocapacitors

Anja Siher

University of Nova Gorica, Vipavska 13, SI-5000 Nova Gorica

Abstract

The aim of this study was to improve the electrochemical performance and energy density of pseudocapacitors by fabricating a metal oxide, (WO_3)-carbon composite. The sol-gel method was used to prepare a material that could perform as an excellent charge-storing electrode. Combining WO_3 with carbon, provided a material with a better specific surface area, porosity, and electrical conductivity to make it more suitable for supercapacitor electrode material. The morphology and structure of the materials were characterized using scanning electron microscopy (SEM), transmission electron microscopy (TEM), and X-ray diffraction (XRD). The electrochemical performance of the composite was assessed by preparing working electrodes of WO_3 sol with different concentrations of polyvinylalcohol (PVA) deposited on carbon cloth, stainless steel, and Ni foam substrates. Cyclic voltammetry and galvanostatic charge-discharge were performed for the electrochemical measurements. The results showed that the capacitance of the composite varied significantly depending on the substrate, with Ni foam exhibiting the highest contribution to the overall capacitance of the material. The electrode prepared with ratio WO_3-sol:PVA=3:7 showed promising results, suggesting that this composite could be used to construct a symmetric supercapacitor for further performance improvement.

Keywords: energy storage system, supercapacitors, pseudocapacitors, WO_3-carbon composite

Email address: anja.siher@ung.si (Anja Siher)

1. Introduction

The demand for electrical energy is increasing, and this has led to the exploration of alternative energy storage systems to compensate for the use of fossil fuels, which contribute to environmental pollution. Renewable energy resources obtained from inexhaustible natural sources such as solar power, wind, and hydropower are becoming more relevant to generate clean electricity without contributing to climate change. However, the problem with these sources is intermittency and one way to address this issue would be to couple them with energy storage systems. These systems are required to store energy from renewable sources such as wind and sun along with grid energy storage for power quality, smoothing, and frequency regulations. To solve and fulfill energy demands, it is necessary to develop efficient technologies that can overcome the difficulties of intermittent energy [1, 2]. Recent demands show the need for an energy storage system that has high power and energy density. While batteries have high specific energy, they lack high power. Supercapacitors are better suited for harvesting, storage, and delivery of electrical energy as they have higher power density, higher charge/discharge rates, and better cycling stability compared to batteries. Despite the challenge caused by the low energy, there is a significant amount of research and development being conducted to address this issue [1, 2].

There are two types of supercapacitors based on charge storage systems: electrochemical double-layer capacitors (EDLC) and pseudocapacitors [2, 3, 4]. Charge separation at the electrode/electrolyte interface results in charge storage in electrochemical double-layer capacitors. To achieve the best performance of EDLCs, it is important to choose the right electrode materials. The electrodes should be made of high surface area material which maximizes the active area of the double layer and minimized the distance between the electrode and electrolyte. Carbon-based materials such as activated carbon, carbon nanotubes (CNTs), carbon nanofibers (CNFs), carbon aerogels, and graphene are used due to their non-toxicity, high specific area, good electronic conductivity, and chemical stability properties [2, 5]. Pseudocapacitors use both electrostatic and redox processes to enhance the total capacitance. Faradic reactions occur near or at the electrode surface and store a large amount of charge in addition to the charge stored in the form of the electrochemical double-layer capacitors. Compared to batteries they possess a lower energy density because the redox reactions occur on the surface of the electrode rather than in the bulk [2]. Metal oxides (RuO_2, NiO, Co_3O_4, MnO_2, and WO_3) and conduction polymers

(polyanilines, polypyrroles, and polythiophenes) are the most commonly used materials for pseudocapacitors [1, 4, 6]. These materials can lead to high faradic capacitive performances; however, they cannot maintain it after long cycling [5].

To enhance the electrochemical performance and energy density of pseudocapacitors, a carbon-based composite WO_3 can be prepared for use as a supercapacitor electrode. WO_3 is an excellent material for charge-storing electrodes due to its facile synthesis, diverse morphology, chemical stability, reversible redox transition W^{IV}/W^{V}, and high theoretical capacitance [1]-[4]. The limitation of electrochemical performance is due to the material´s poor electrical conductivity. To overcome this issue, researchers have made significant efforts to optimize the morphology and structure of WO_3 by using other conducting materials such as conducting polymers (PEG, PVA, PS,...) to prepare a composite that leads to better specific capacitance and long cycle life [7, 8].

2. Experimental details

The experiments performed in this study require the selection of materials, preparation of composite samples, and subsequent characterization of the samples.

2.1. Materials

Tungsten powder (99,9 %) and triton x-100 were purchased from Alfa Aesar. Hydrogen peroxide (H_2O_2, 30 %), isopropanol (C_3H_8O, 98 %), PVA (87-90 %, average molecular weight = 30 000 - 70 000), and Nafion were purchased by Sigma Aldrich. For the electrode substrates stainless steel ss316L, nickel foam (98 % porosity), and carbon cloth were used.

2.2. Preparation of WO_3 and WO_3-PVA composite deposited on stainless steel and Ni foam

The tungsten sol was prepared according to the method explained in [9] where 4 mmol of tungsten powder was mixed with 7 mL of 30 % aqueous solution of H_2O_2. After an exothermic reaction occurred, the solution became colorless. The solution was cooled to room temperature before adding 5 mL of isopropanol. After 30 minutes, 1.2 mL of triton x-100 was added. A series of different mass ratios of metal oxide and PVA were done by mixing solutions of WO_3 with an aqueous solution of PVA: 2-8, 3-7, and 4-6.

The small tiles of stainless steel ss316L were cleaned in ethanol and dried with nitrogen. A solution of tungsten sol with PVA in different ratios was applied to the tiles using a spin-coating process. The amount of solution deposited on each tile was 200 µL. Each spin-coating process lasted for 30 seconds at a speed of 1200 rpm. After coating, the tiles were dried for 5 minutes at 60 °C, and the process was repeated five times for each tile. Solutions of tungsten sol with PVA in different ratios were applied to nickel foams measuring 10x15 mm using a dip-coating process. The nickel foam was submerged in the solution for 5 seconds and then allowed to dry for 5 minutes at 60 °C. This deposition process was repeated four times for each nickel foam. The samples of WO_3-PVA on stainless steel and WO_3-PVA on nickel foam were thermally treated by heating in a furnace from room temperature to 500 °C at a heating rate of 2 °C/min in a flow of 20 mL/min argon. The solutions of WO_3-PVA 2-8, 3-7, and 4-6 were dried in a vacuum drier at 40 °C for 14 hours. After drying a film was obtained on the walls of the beaker. The resulting film was subjected to thermal treatment in a furnace from room temperature to 500 °C at a heating rate of 2 °C/min in a flow of 20 mL/min argon. The working electrode was prepared by mixing a resulting into 0.5 % Nafion solution and deposited on the carbon cloth substrate. The WO_3-PVA (2-8, 3-7, and 4-6) deposited on nickel foam was used for electrochemical measurements as prepared.

2.3. Characterization

The surface morphology and elemental composition of the films were investigated using an SEM (JEOL JSM7001TTLS) equipped with an EDX detector. The HR-TEM results were obtained by using JEOL JEM2100F operating at 200 kV. The X-ray diffraction patterns were obtained using powder-XRD (SmartLab SE, Rigaku Corporation) using a Cu radiation source (Cu Kα 0.1541 mm).

Electrochemical measurements were conducted to investigate the redox behavior, electrocatalytic activity, and stability of WO_3-carbon composites using a three-electrode system in an electrochemical workstation (SP-300, Biologic). The system comprised a reference electrode of Ag/AgCl in a 3.8 M KCl solution, a counter electrode of Pt wire, and a working electrode. All electrochemical measurements were performed in an aqueous solution of N_2-purged 1 M KOH as an electrolyte. The cyclic voltammetry measurements were performed from -1.35 V to 0.5 V for scan rates ranging from 0.5 to 500 mV/s. The galvanostatic measurements were conducted from -1.35 V to 0.5 V for current densities ranging from 0.5 to 20 A/g at a potential range of -1.35 V to 0.5 V.

3. Results and discussion

3.1. Structural and morphological characterization

3.1.1. Morphological characterization of WO_3-PVA 2-8, 3-7, and 4-6 on stainless steel

The backscattering electron BED-C detector was used to capture the WO_3-PVA with different concentrations deposited on stainless steel (Figure 1). The WO_3-PVA 2-8 sample (Figure 1b) demonstrates that WO_3 is coated with amorphous carbon due to the phase boundaries detected by the BED-C detector. The WO_3-PVA 3-7 sample (Figure 1c) exhibits surface defects that are recognizable due to the drying of the suspension on the stainless steel. Furthermore, WO_3 nanoparticles were repeatedly coated with amorphous carbon, resulting in a significant increase in nanoparticle size compared to the WO_3-PVA 2-8 sample. This trend continued for the WO_3-PVA 4-6 sample (Figure 1d).

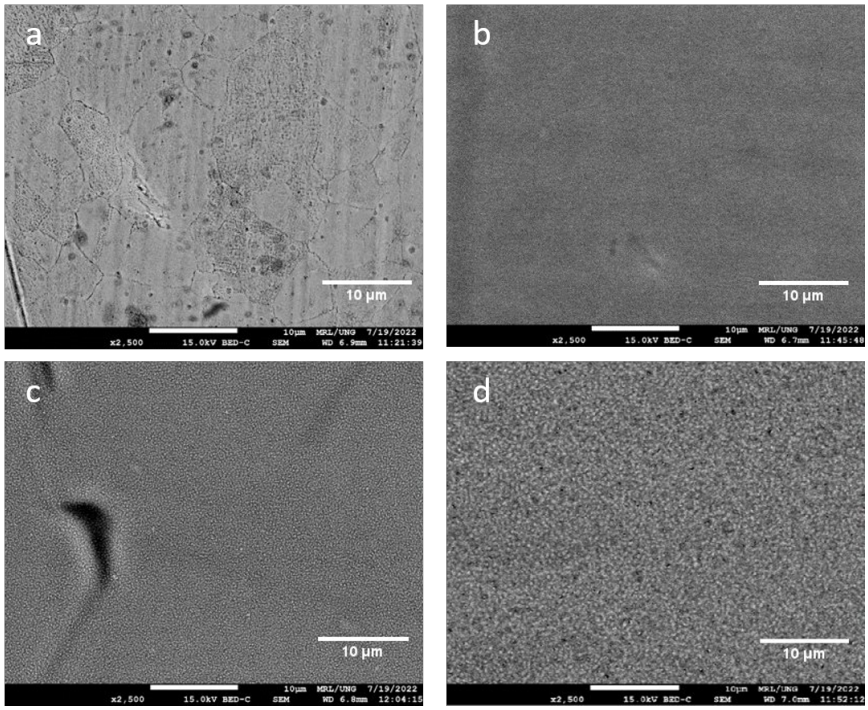

Figure 1: SEM images of a.) Stainless steel b.) WO_3-PVA 2-8 on stainless steel c.) WO_3-PVA 3-7 on stainless steel d.) WO_3-PVA 4-6 on stainless steel captured by a backscattered electron detector (BED-C).

When comparing all of the WO_3-PVA samples with different concentrations, there is a growth of WO_3 nanoparticles from 2-8 to 4-6, which corresponds to higher concentrations of tungsten in the sol. The elemental composition of the samples (Figure 2) that are presented with the EDX spectra revealed the presence of carbon, which predictably changed with the corresponding concentration. The signals that correspond to Cr, Mn, Fe, and Ni are components of stainless steel.

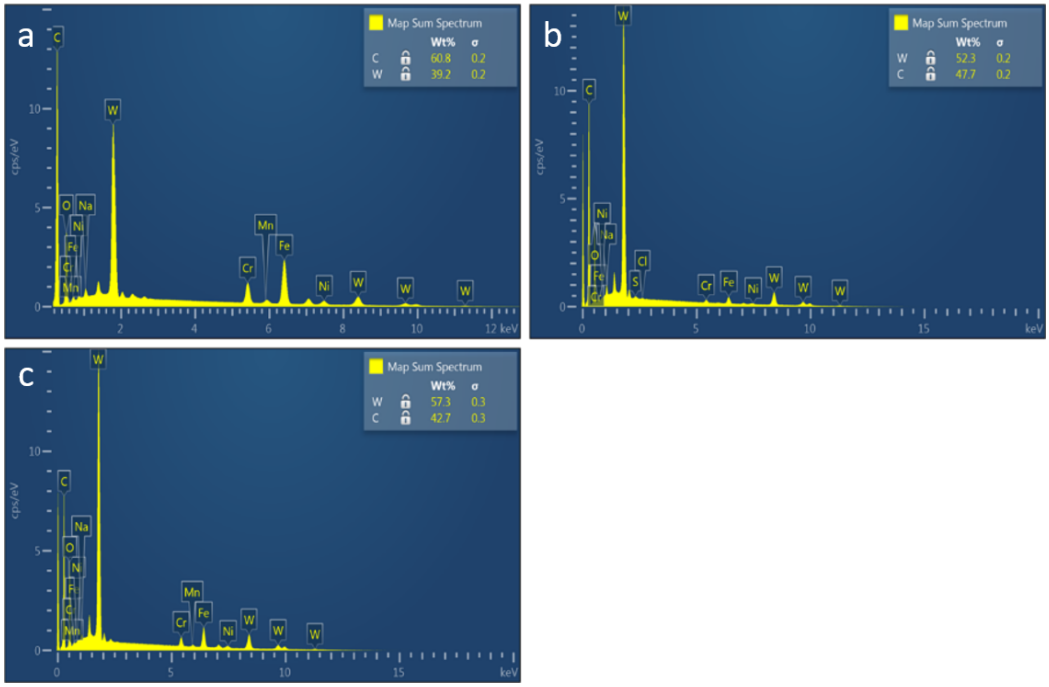

Figure 2: The stainless steel substrate was coated with WO_3-PVA samples of different concentrations and the resulting EDX spectra are: a.) WO_3-PVA 2-8 on stainless steel b.) WO_3-PVA 3-7 on stainless steel c.) WO_3-PVA 4-6 on stainless steel.

The carbon signal decreased from 2-8 to 4-6 samples due to the lower concentration of PVA in the sample.

To confirm that the concentration of carbon increases with the concentration of PVA, the ratio between tungsten and carbon was measured and averaged from EDX measurements taken at multiple parts of the coating (Table 1).

WO_3-PVA [m/m]	W	C	WO_3-C [m/m]
4-6	57.3	42.7	1.69
3-7	52.3	47.7	1.38
2-8	39.2	60.8	0.81

Table 1: The ratio between tungsten and carbon was calculated from EDX spectra for WO_3-PVA samples of different concentrations deposited on stainless steel.

3.1.2. Morphology characterization of WO_3-PVA 3-7 dip-coated on Ni foam

The SEM images of the WO_3-PVA 3-7 samples deposited in the nickel foam (Figure 3) revealed a uniform distribution of the nanoparticles.

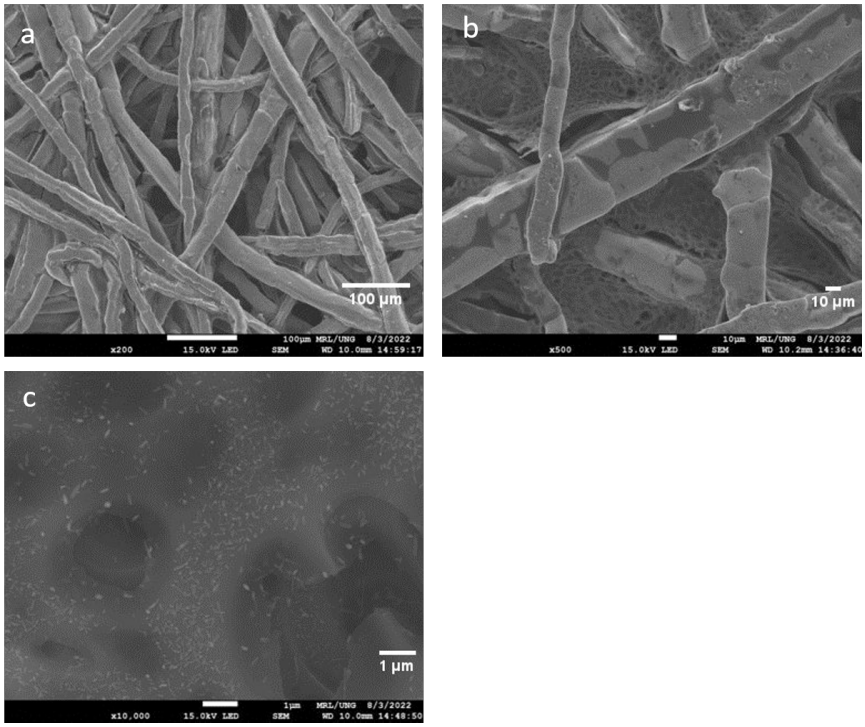

Figure 3: SEM images of a.) Ni foam and b-c.) WO_3-PVA 3-7 deposition on Ni foam.

The highly porous nickel foam (Figure 3a) with its thin fibers makes it an ideal substrate for catalytic activity and coating distribution. The EDX mapping of the selected area (Figure 4) revealed the distribution of tungsten, nickel, and carbon on the nickel foam. As predicted, there is a homogeneous distribution of nickel on the nickel fibers. Due to the high porosity of the nickel foam, WO_3 and carbon are uniformly distributed around and in between the thin fibers of the nickel foam. To further characterize the morphology of the samples, transmission electron microscopy (TEM) was employed. All of the high-resolution transmission electron microscopy (HR-TEM) images (Figure 5) exhibit dark spots that represent the denser phase of WO_3 coated with amorphous carbon.

As expected from the EDX analysis results, WO_3-PVA 4-6 has the most dark spots. The WO_3-PVA 2-8 nanoparticles (Figure 5a) are 20 nm in size, while WO_3-PVA 3-7 (Figure 5b) and WO_3-PVA 4-6 (Figure 5c) are less than 20 nm. As the images show that the particles are surrounded by an amorphous layer of carbon, it indicates the success of preparing the WO_3-C composite.

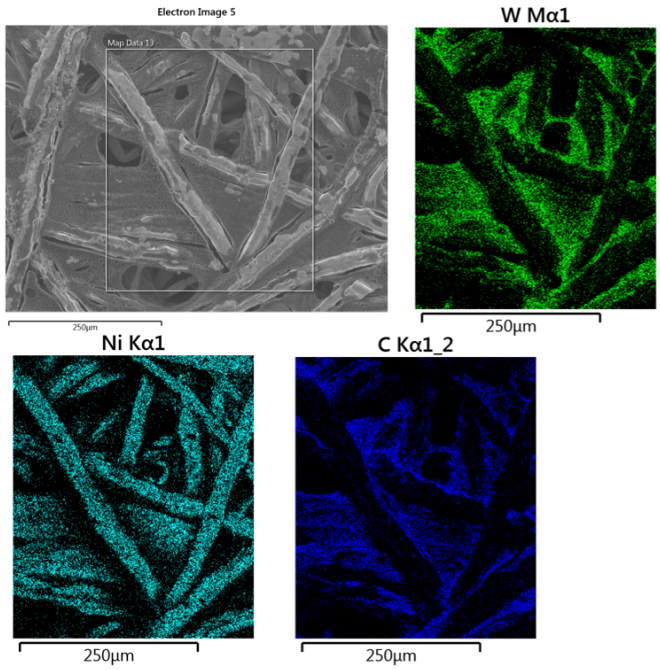

Figure 4: The EDX mapping of the selected area of EDX mapping of WO_3-PVA 3-7 shows the distribution of tungsten, nickel, and carbon on nickel foam.

The selected area electron diffraction (SAED) pattern of all the samples is shown in Figure 6.

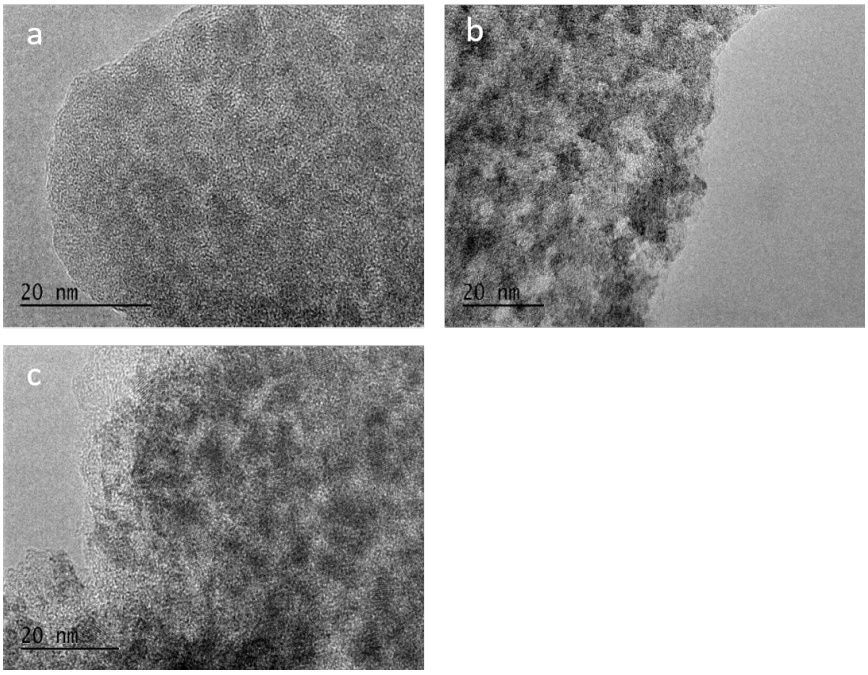

Figure 5: HR-TEM images of a.) WO_3-PVA 2-8, b.) WO_3-PVA 3-7 and c.) WO_3-PVA 4-6 exhibit dark spots that represent the denser phase of WO_3 coated with amorphous carbon.

It is difficult to determine the crystallinity of the WO_3-PVA 2-8 sample (Figure 6a-b). At the beginning of the measurement, there were visible ring patterns that are typical for an amorphous or nanocrystalline structure (Figure 6a).

After inducing an electron beam, crystallization occurred and polycrystalline WO_3 was formed (Figure 6b). Due to the higher concentration of WO_3 in the sample, ring patterns that are characteristic of polycrystalline material were formed (Figure 6c-d).

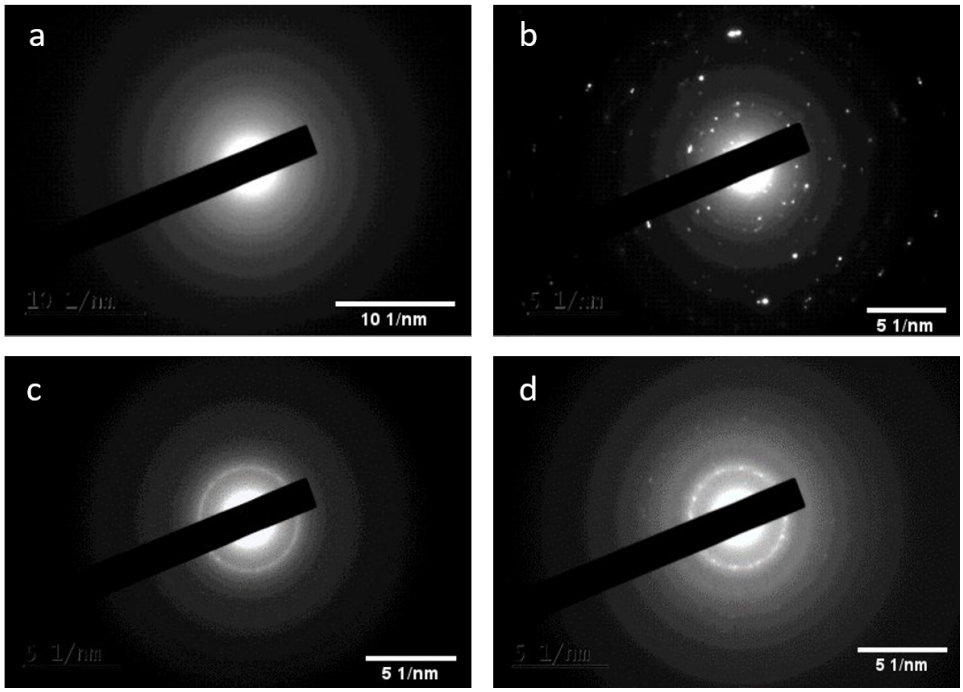

Figure 6: The SAED image of: a.) and b.) WO_3-PVA 2-8, c.) WO_3-PVA 3-7 and d.) WO_3-PVA 4-6.

3.1.3. Structure characterization of WO_3-PVA deposited on stainless steel

From the XRD spectra of WO_3-PVA 2-8, 3-7, and 4-6 samples (Figure 7), we can observe an increasing trend in polycrystalline or amorphousness of WO_3.

The peaks at 24° (2 θ) become less sharp and more diffuse with decreasing WO_3 content, indicating a smaller size and less defined crystals.

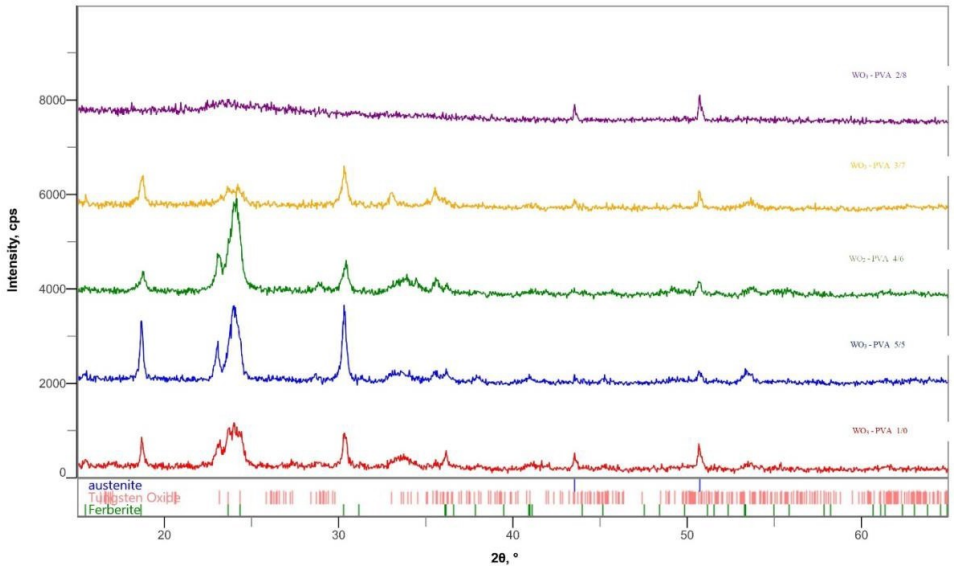

Figure 7: XRD spectra for WO_3-PVA deposited on stainless steel: WO_3-PVA 2-8 (purple line), WO_3-PVA 3-7 (yellow line), WO_3-PVA 4-6 (green line).

3.2. Electrochemical characterization

The electrochemical performance of WO_3-PVA electrodes on different substrates was evaluated in a three-electrode system. We prepared two types of working electrodes by depositing WO_3-PVA (2-8, 3-7, and 4-6) powder on carbon cloth and Ni foam, respectively. We optimized the cyclic voltammetry measurements by setting the operation window from -1.35 V to 0.5 V. Figure 8 shows the comparison of cyclic voltammograms for both types of prepared electrodes at a scan rate of 50 mV/s. The WO_3-PVA 3-7 presented in Figure 8a (red curve) had the widest voltage window among the electrodes. The oxidation peak at around 0.7 V corresponds to the W^{5+}/W^{6+} redox couple, while the reduction peak at -1.0 V corresponds to the W^{6+}/W^{5+} redox couple. These peaks were not that significant for WO_3-PVA 2-8 (green line) and 4-6 (blue line).

All the electrodes deposited on carbon cloth had low capacitance and narrow voltage windows in the range from 0 V to 0.5 V.

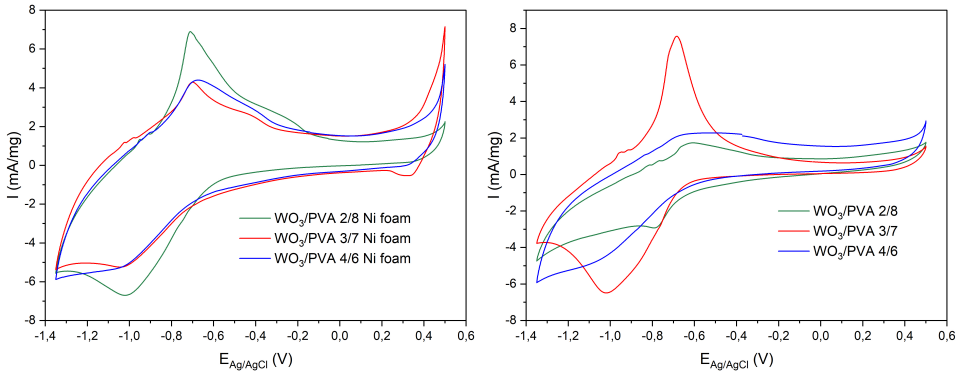

Figure 8: Cyclic voltammograms of: a.) WO_3-PVA (2-8 3-7, and 4-6) powder deposited on carbon cloth b.) WO_3-PVA (2-8, 3-7, and 4-6) deposited on Ni foam at a scanning rate of 50 mV/s.

The presence of Ni foam (Figure 8b) increased the voltage window for all the samples. In contrast to Figure 8a, there were oxidation and reduction peaks in the range from 0 V to 0.5 V that corresponded to nickel redox reactions. The oxidation peak for Ni^{2+}/Ni^{3+} was around 0.4 V and the reduction peak for Ni^{3+}/Ni^{2+} was around 0.3 V. The addition of Ni foam also increased the overall capacitance of the system. The cyclic voltammograms also revealed an oxidation peak for Ni^{0}/Ni^{2+} at around -0.4 V along with peaks for W^{5+}/W^{6+} at the same potential as in Figure 8a. By comparing the measurements in Figure 8, we found that WO_3-PVA 3-7 electrode exhibits the best performance regardless of the substrate. We also noted that Ni foam contributed significantly to the overall capacitance of the system.

Galvanostatic charge-discharge curves were obtained for WO_3-PVA (2-8, 3-7, and 4-6) at a current density of 1 A/g and a voltage range of -1.35 V to 0.5 V (Figure 9). The results indicate that WO_3-PVA 3-7 has the longest charge and discharge time at 1 A/g compared to the other two electrodes, which have relatively short charge and discharge times.

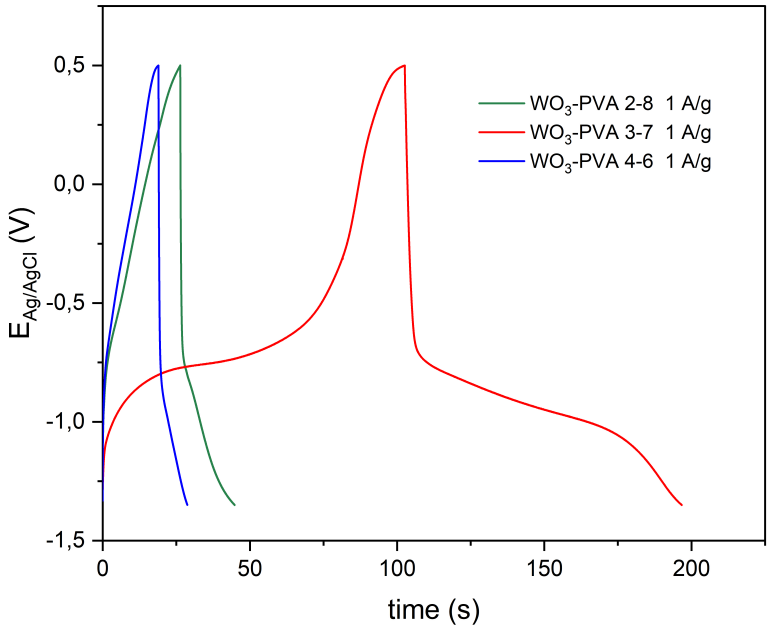

Figure 9: Galvanostatic charge-discharge curves for WO_3-PVA 2-8, 3-7, and 4-6 at a current density of 1 A/g.

The WO_3-PVA 3-7 material was selected for further analysis based on its cyclic voltammetry performance. Figure 10 presents the cyclic voltammograms and galvanostatic charge-discharge curves for WO_3-PVA 3-7 deposited on carbon cloth. The cyclic voltammograms at different scan rates (Figure 10a) were: 500 mV/s, 200 mV/s, 100 mV/s, 50 mV/s, 20 mV/s, 10 mV/s, 5 mV/s, 1 mV/s and 0.5 mV/s. The peak current ratios decrease with increasing scan rates, indicating quasi-reversible or irreversible behavior. The voltage window also narrows as the scan rate increases.

The oxidation and reduction peaks for W^{5+}/W^{6+} are observed at around 0.4 V and -1.0 V.

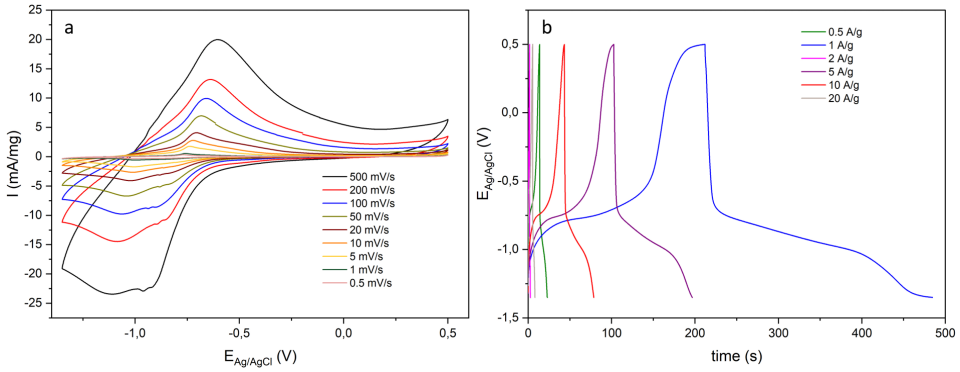

Figure 10: WO_3-PVA 3-7 powder deposited on carbon cloth: a.) different scan rates b.) galvanostatic charge-discharge curves.

The galvanostatic charge-discharge (Figure 10b) at different current densities shows that higher current density leads to shorter charge and discharge times. Specifically, the charge and discharge time is much shorter at 20 A/g than at 1 A/g.

4. Conclusion

In this study, WO_3-PVA with different concentrations (2-8, 3-7, and 4-6) was successfully synthesized and fabricated on different substrates. The results show that WO_3-PVA 3-7 deposited on carbon cloth exhibits oxidation and reduction peaks for W^{5+}/W^{6+} and W^{6+}/W^{5+}. It also presents the longest charge and discharge time compared to the other two electrodes. Although the results for WO_3-PVA 2-8, 3-7, and 4-6 with deposition on Ni foam show greater capacitance, the comparison to WO_3-PVA deposited on carbon cloth suggests that nickel contributes significantly to the overall capacitance due to its redox reactions. The results suggest that WO_3-PVA 3-7 powder deposited on carbon cloth is the most suitable electrode for further analysis by building a symmetric supercapacitor due to its superior performance.

References

[1] Giacometta Mineo, Elena Bruno, and Salvo Mirabella. Advances in WO_3-based supercapacitors: State-of-the-art research and future perspectives. *Nanomaterials*, 13(8), 2023.

[2] Patrice Simon and Yury Gogotsi. Perspectives for electrochemical capacitors and related devices. *Nature materials*, 19(11):1151—1163, November 2020.

[3] Yuqi Jiang and Jinping Liu. Definitions of pseudocapacitive materials: A brief review. *ENERGY & ENVIRONMENTAL MATERIALS*, 2(1):30–37, 2019.

[4] Vaibhav Lokhande, Abhishek Lokhande, Gon Namkoong, Jin Hyeok Kim, and Taeksoo Ji. Charge storage in WO_3 polymorphs and their application as supercapacitor electrode material. *Results in Physics*, 12:2012–2020, 2019.

[5] Parnia Forouzandeh, Vignesh Kumaravel, and Suresh C. Pillai. Electrode materials for supercapacitors: A review of recent advances. *Catalysts*, 10(9), 2020.

[6] Pragati A. Shinde, Abhishek C. Lokhande, Amar M. Patil, and Chandrakant D. Lokhande. Facile synthesis of self-assembled WO_3 nanorods for high-performance electrochemical capacitor. *Journal of Alloys and Compounds*, 770:1130–1137, 2019.

[7] Amit Kumar Das, Sarbaranjan Paria, Anirban Maitra, Lopamudra Halder, Aswini Bera, Ranadip Bera, Suman Kumar Si, Anurima De, Suparna Ojha, Sumanta Bera, Sumanta Kumar Karan, and Bhanu Bhusan Khatua. Highly rate capable nanoflower-like nise and WO_3-ppy composite electrode materials toward high energy density flexible all-solid-state asymmetric supercapacitor. *ACS Applied Electronic Materials*, 1(6):977–990, 2019.

[8] Vaishali Tanwar, Rasmita Barik, and Pravin P Ingole. Uniquely designed tungsten oxide nanopetal decorated electropsun pan nanofiber for a flexible supercapacitor with ultrahigh rate capability and cyclability. *ACS Applied Energy Materials*, 5(2):1767–1780, 2022.

[9] Martin Rozman, Boštjan Žener, Lev Matoh, Regina Fuchs Godec, Argyroula Mourtzikou, Elias Stathatos, Urban Bren, and Miha Lukšič. Flexible electrochromic tape using steel foil with WO_3 thin film. *Electrochimica Acta*, 330:135329, 2020.